Diss. ETH No. 15255

LARGE-EDDY SIMULATION OF COMPRESSIBLE FLOWS USING THE FINITE-VOLUME METHOD

A dissertation submitted to the
SWISS FEDERAL INSTITUTE OF TECHNOLOGY
ZÜRICH

for the degree of
Doctor of Technical Sciences

presented by

Roland von Kaenel

Dipl.-Ing. (Swiss Federal Institute of Technology Lausanne)
born on October 29, 1976
citizen of Switzerland

accepted on the recommendation of

Prof. Dr. L. Kleiser, examiner
Prof. Dr. N. A. Adams, co-examiner
Dr. J. B. Vos, co-examiner

2003

The picture on the title page shows contour lines of the pressure gradient for the supersonic ramp flow.

Acknowledgments

I would like to thank Prof. L. Kleiser for the supervision of my research and for his constant interest and support during my work at the Institute of Fluid Dynamics (IFD).

I wish also to warmly thank my two co-examiners, Prof. N. A. Adams (now with Institute of Fluid Mechanics at the Technical University of Dresden) and Dr. J. B. Vos (CFS Engineering).

I very much appreciated the clear guidance and precious advice of Prof. N. A. Adams. Research in his presence has always been very stimulating and I learned a lot about large-eddy simulation and fluid mechanics thanks to him. He spent a lot of time in discussing the numerous problems that arose and in proofreading my publications.

Since the very first day of my Ph.D., I could always count on the help of Dr. J. B. Vos. I have found the best possible "NSMB expert" in him to solve every problem that I encountered with the computational code. All my publications have benefited from his careful proofreading and valuable suggestions. Furthermore, it has always been a pleasure to visit him in Lausanne to discuss open problems.

Finally, I would like to thank all my friends and colleagues at IFD for numerous instructive discussions and many recreational activities. Special thanks go to Dr. Benjamin Rembold for giving me so often a hand and proofreading this thesis.

This work was supported by an ETH Zürich research grant and the Swiss ERCOFTAC Fellowship Program. Calculations were performed at the Swiss Center for Scientific Computing (CSCS).

Zürich, July 2003 Roland von Kaenel

Contents

Nomenclature

Roman symbols

$\mathbb{A}$	Jacobian matrix of the inviscid fluxes
a, b	forcing coefficients
C_f	skin-friction coefficient
C_+, C_0, C_-	characteristics
c	speed of sound
c_p, c_v	specific heat coefficients at constant pressure, volume
D_{ij}^k	k-th component of the artificial dissipation vector through the j-th cell face of the i-th cell
$\mathbf{D}$	artificial numerical dissipation vector
$\mathbf{d}$	artificial numerical dissipation vector for a surface
E	total energy
E_1, E_2	streamwise, spanwise energy spectra
e_i	limiting factors for the eigenvalues
F_{ij}^k	k-th component of the flux vector through the j-th cell face of the i-th cell
F_2	structure function
$\mathbf{F}$	flux vector
$\mathbb{F}$	flux tensor
f_1	forcing
$\mathbf{f}_{inv}, \mathbf{f}_v$	vector of inviscid, viscous flux in x_1 direction
G_1, G_2	primary, secondary filter kernel
$\mathbf{g}_{inv}, \mathbf{g}_v$	vector of inviscid, viscous flux in x_2 direction
H	channel half-width
h	computational-space grid interval
$\mathbf{h}_{inv}, \mathbf{h}_v$	vector of inviscid, viscous flux in x_3 direction
k	thermal conductivity
k_1, k_2	streamwise, spanwise wavenumber
$k^{(2)}, k^{(4)}$	user defined coefficients for the artificial dissipation
K	degree Kelvin
$\mathbb{L}$	matrix of eigenvalues
L	length
M	Mach number
M^k	k-th filter moment

N	deconvolution order
N_i	number of cells in each coordinate direction
$\mathbf{n}, n_i$	normal vector, components
n_{faces}	number of faces of a control volume
Pr	Prandtl number
p	pressure
Q	mass flow
q_i	heat flux due to conduction
$\mathbf{R}$	residual vector
Re	computational Reynolds number
Re_b	Reynolds number based on bulk quantities
Re_θ	Reynolds number based on the momentum thickness of the boundary layer
Re_τ	Reynolds number based on the friction velocity
$\mathbf{S}$	surface vector
S	cell surface
s	Sutherland's law constant
$\mathbb{T}$	matrix of eigenvectors
T	temperature
t	time
$\mathbf{U}$	state vector of conservative variables
$\mathbf{U}_i$	state vector of conservative variables averaged over the i-th cell
$\mathbf{u}, u_i$	velocity vector, components
u_τ	friction velocity
$\mathbf{V}$	state vector of primitive variables
V	control volume
$\mathbf{W}$	state vector of characteristic variables
x_i	coordinate directions

Greek symbols

α_i	filter coefficients
β	CFL number
γ	c_p/c_v
Δ	interval
δ_1	displacement thickness of the boundary layer
$\varepsilon^{(2)}, \varepsilon^{(4)}$	weights of artificial dissipation terms
Θ	compression ramp angle

λ_i	eigenvalues
$\rho(\mathbb{A})$	spectral radius of the matrix $\mathbb{A}$
ρ	density
μ	dynamic viscosity
ν	pressure switch
ν_l, ν_r	left, right filter stencil bound
ξ_i	coordinate directions in computational space
τ	shear stress
τ_{ij}	components of the shear stress tensor
φ_i	Runge-Kutta stage coefficients
χ	relaxation coefficient
ω	wavenumber
ω_i	vorticity vector components
ω_c	filter cutoff wavenumber
ω_n	numerical (Nyquist) cutoff wavenumber

Other symbols

det	determinant
$*$	convolution operator
∇	nabla operator
$\Im(\cdot)$	imaginary part
$<.>$	averaged quantities

Subscripts

$\cdot_b$	bulk quantity
$\cdot_c$	channel center quantity
$\cdot_{inv}$	inviscid quantity
$\cdot_n$	normal component of a vector
$\cdot_{ref}$	reference quantity
$\cdot_t$	tangent component of a vector
$\cdot_v$	viscous quantity
$\cdot_{VD}$	van-Driest-transformed quantity
$\cdot_w$	wall quantity
$\cdot_\infty$	free-stream quantity
$\cdot_{-1}$	variable of the second ghost cell
$\cdot_0$	variable of the first ghost cell
$\cdot_1$	variable of the first inner cell

$\cdot_2$	variable of the second inner cell

Superscripts

$\cdot^c$	contravariant quantity
$\cdot^s$	quantity of a shifted control volume
$\cdot^*$	dimensional quantity
$\bar{\cdot}$	filtered quantity
$\cdot^\star$	deconvolved quantity
$\breve{\cdot}^\star$	computed with deconvolved quantities
$\hat{\cdot}$	Fourier transform
$\cdot^+$	quantity in wall units
$\tilde{\cdot}$	Favre-averaged quantity
$\cdot'$	fluctuating quantity
$\cdot''$	Favre fluctuations

Abbreviations

ADM	approximate deconvolution model
CERFACS	Centre Européen de Recherche et de Formation Avancée en Calcule Scientifique
CFD	computational fluid dynamics
DES	detached-eddy simulation
DNS	direct numerical simulation
ENO	essentially nonoscillatory
EPFL	Ecole Polytechnique Fédérale de Lausanne
ETHZ	Eidgenössische Technische Hochschule Zürich
IFD	Institute of Fluid Dynamics
KTH	Kungl Tekniska Högskolan
LES	large-eddy simulation
LMF	Laboratoire de Mécanique des Fluides
MILES	Monotonically integrated LES
NSMB	Navier-Stokes Multi-Block
RANS	Reynolds-averaged Navier-Stokes
rms	root-mean square
TVD	total variation diminishing
URANS	unsteady RANS
WENO	weighted ENO

Abstract

The approximate deconvolution model (ADM) for large-eddy simulation (LES) is formulated for the finite-volume method and implemented in a CFD code which is being used in standard computational fluid dynamics design tasks in the aerospace industry.
Two flow configurations of increasing complexity are investigated to assess ADM in the finite-volume framework.
The turbulent channel flow at a Mach number of M=1.5 and a Reynolds number based on bulk quantities of Re_b=3000 is selected first to validate the adaptation of ADM to the finite-volume method and to evaluate the near-wall behavior of the model. Overall, the LES results show good agreement with the filtered data of a direct numerical simulation (DNS), performed for comparison. For this rather simple configuration and using a second-order spatial discretization, differences between ADM and computations without explicit subgrid-scale model are found to be small. The ability of standard artificial numerical dissipation to replace the relaxation regularization procedure of ADM is also investigated. Results show that this approach is pertinent provided adequate dissipation coefficients are found.
Second, the supersonic turbulent boundary layer along a compression ramp at a free-stream Mach number of M=3 and a Reynolds number (based on free-stream quantities and the mean momentum thickness at inflow) of Re_θ=1685 is computed to evaluate the ability of ADM to represent shock-turbulence interaction. It is observed that a unified modeling of discontinuities and turbulence requires a local adaptation to the flow of the secondary filter used in the relaxation regularization. The LES results are compared with corresponding filtered DNS data from literature. Very good agreement between the filtered DNS and the LES is observed for the mean, fluctuating, and averaged wall quantities.

Kurzfassung

Ein auf einer Approximation der Filter-Inversen beruhendes Modell (ADM) für die Grobstruktursimulation (LES) wird für Finite-Volumen-Verfahren formuliert und in ein industrielles Rechenprogramm implementiert.
Zwei Strömungen von zunehmender Komplexität werden untersucht, um ADM im Finite-Volumen-Rahmen zu bewerten.
Die turbulente Kanalströmung bei einer Machzahl von M=1.5 und einer Reynoldszahl bezogen auf Kanalmittelwerte von Re_b=3000 wird als erstes ausgewählt, um die Anpassung von ADM an das Finite-Volumen-Verfahren zu validieren und um das Verhalten des Modells in Wandnähe abschätzen zu können. Im allgemeinen zeigen die LES-Ergebnisse eine gute Übereinstimmung mit gefilterten Daten einer direkten numerischen Simulation (DNS), die zum Vergleich durchgeführt wurde. Für diese relativ einfache Strömungskonfiguration und mit Anwendung eines Verfahrens zweiter Ordnung wird beobachtet, dass die Unterschiede zwischen ADM und Berechnungen ohne explizitem Feinstrukturmodell gering sind. Weiterhin wird die Möglichkeit untersucht, den Relaxationsterm von ADM durch künstliche numerische Dissipation zu ersetzen. Die Ergebnisse zeigen, dass dieser Ansatz angemessen ist, falls passende Dissipationskoeffizienten gefunden werden.
Als zweites Problem wird die Überschallgrenzschicht entlang einer Kompressionsrampe mit einer Aussenströmungs-Machzahl von M=3 und einer Reynoldszahl (bezogen auf Aussenströmungsgrössen und die Impulsverlustdicke am Einströmrand) von Re_θ=1685 berechnet, um zu untersuchen, ob ADM die Stoss-Turbulenz-Wechselwirkung darstellen kann. Es wird festgestellt, dass eine lokale Anpassung des sekundären Filters an die Strömung notwendig ist, um eine Beschreibung von Stoss und Turbulenz mit einem einheitlichem Ansatz zu ermöglichen. Die LES-Ergebnisse werden mit gefilterten DNS-Daten aus der Literatur verglichen. Eine sehr gute Übereinstimmung zwischen gefilterter DNS und LES für Mittelwerte, Fluktuationen und Wandgrössen wird festgestellt.

Chapter 1

Introduction

1.1 Large-eddy simulation for industrial applications?

The maximal ratio between lift and aerodynamic drag for an airplane's wing, the optimal mixing of fuel and air in the combustion chamber of an engine or a turbine and the efficient cooling of a computer chip are examples of applications of great interest for the industry. A reduced drag of even less than one percent can contribute to the success or failure of an aircraft versus its competitor. To meet increasingly severe pollution norms and to achieve economical competitiveness, fuel efficiency in engines and turbines has become a major concern nowadays for airlines, power generation industry and engine manufacturers, to name only a few. Another example is the computer industry, where growing performance of CPUs together with miniaturization constraints has resulted in challenging cooling issues. Whether they concern aerodynamical, combustion, thermal problems or yet another domain, accurate prediction of the flow phenomena involved in these applications is essential to achieve an optimal design. In almost every case, the flow exhibits turbulent behavior. Turbulence, which is characterized by unsteady, three-dimensional, large- and small-scale fluctuations, increases the mixing and friction in flows. It plays therefore a significant role in technology, and independently of whether it is desired or not, engineers have to be able to predict turbulent flows.

More than a century ago, Reynolds (1883) described the structure of turbulence with its whirls of different sizes and became famous by finding that a flow changes from an orderly laminar state to a turbulent state depending on the value of a certain parameter, named the Reynolds number (Re), which measures the ratio between inertial and viscous forces. For decades, research in fluid mechanics remained confined to analytical theory and experiments. Progress in analytical theory rapidly encountered limits due to the complexity, in particular nonlinearity, of the problem, for which an analytical solution can only be obtained for very simple flows. Experimental research has been conducted for many

years and is still a method of fundamental importance.

The first working computer saw life in the second World War, but it was the invention of the transistors by the end of the 1950's that contributed to a wide-scale use of computers. Since then computer power has grown rapidly, first with the introduction of vector computers in the 1970's, followed by massively parallel computers in the 1990's. As an example, a problem which took one year of computing time in 1980 could in 2001 be solved in only 17 seconds. With the advent of substantial computer power and improved numerical methods came the interest in numerical simulation of flows, which is the subject of this study.

The starting point for the numerical simulation of flows is formed by the Navier-Stokes equations which express the conservation of mass, momentum and energy. Three approaches can be followed to solve numerically these equations for turbulent flows: direct numerical simulation (DNS), Reynolds-averaged Navier-Stokes simulation (RANS), and large-eddy simulation (LES).
DNS is the most straightforward approach and consists in solving the Navier-Stokes equations for all spatial and temporal scales of motion present in the flow. When it can be applied, DNS is unrivaled in accuracy and in the level of description provided. However, as even the smallest scales where the viscous dissipation takes place have to be resolved, the computational grid needs to be very fine. Even worse, as the Reynolds number becomes larger, the amount of scales in a turbulent flow increases and the computational mesh has to be refined dramatically. It can actually be shown that the computational cost of a simulation scales with Re^3 (Pope, 2000) so that the feasibility of DNS remains limited to low-Reynolds-number flows. Furthermore, DNS uses generally high-order accurate numerical methods for which the extension to complex geometries is not straightforward. DNS may thus be a very powerful tool for fundamental analysis of flows at low Reynolds number and in simple geometries, but is far from being applicable to computations of industrial interest where highly distorted meshes are prevalent and the Reynolds number is typically three orders of magnitude larger.

In order to reduce the amount of scales to be resolved, an ensemble-averaging operator can be applied to the Navier-Stokes equations leading to the RANS equations. In practice the ensemble averaging is carried out by time averaging in case of inhomogeneous turbulence and by space averaging in case of homogeneous turbulence so that the flow is only resolved in terms of time-averaged and space-averaged variables. The

averaging of the nonlinear terms introduces, however, new unknowns for which closure needs to be obtained by means of a turbulence model. A large variety of turbulence models has been derived over the years, starting with simple algebraic models and ending with more sophisticated two-equation models (see Wilcox (1994); Leschziner & Drikakis (2002)). Common numerical methods for the RANS simulations are finite-difference or finite-volume methods as they have proved their practicability on the complex grids needed for industrial flows. A decisive advantage of RANS is found also with its favorable computational cost at high Reynolds number. Indeed, as only the mean flow is resolved, RANS can be applied for flows at realistic high Reynolds number still at a reasonable computational cost. One drawback of RANS is that the quality of the results depends to a large extent on the appropriateness of a turbulence model to cope with a particular flow configuration, stressing thus the importance of experience and practice in the choice of the best model. For statistically stationary turbulence, RANS nevertheless provides an unbeatable ratio between flow prediction quality and computational cost which made it to become the favorite computational method for industrial simulations.

Unsteady phenomena, however, introduce a fundamental uncertainty into the RANS framework. Reynolds-averaging presupposes that the flow is statistically stationary. At the very least, the time-scale associated with the organized unsteady structures must be substantially larger than the time-scale of the turbulent fluctuations. This condition may be satisfied for low-frequency motion such as dynamic stall, but not necessarily in flutter, buffet, unsteady separation and reattachment, transition or vortex interaction, where RANS methods reach their limit. Mainly driven by the aeronautical and turbomachinery industry, where these flow phenomena are prevalent, alternative methods to circumvent the stationary assumption of RANS needed to be found.

A first solution is obtained with the so-called unsteady RANS (URANS) technique. In this case the high-frequency turbulent fluctuations are modeled whereas the large-scale motions are resolved as unsteady phenomena. In practice a dual time-stepping method is used in which the computation is advanced temporally in an outer loop while the convergence to a steady-state problem is pursued in an inner loop. The temporal integration of the outer loop is generally explicit and its time step directly determines the highest frequency of the unsteady motions that can be captured, whereas in the inner loop, fast convergence

is desired and implicit schemes are used. The results and the computational cost are obviously very much dependent on the outer-loop time step. Moreover, URANS is still tightly bound to the quality of the RANS models and accordingly its success is limited.

The last approach, LES, lies between DNS and RANS in terms of computational cost and resolved scales. In LES, the large eddies are resolved, which correspond to large scales, while the effect of the small eddies is modeled. The separation between large and small scales is obtained by application of a spatial filter to the Navier-Stokes equations yielding the filtered Navier-Stokes equations with corresponding filtered variables. The filter width, which is a characteristic length-scale, determines the scales that are still present in the filtered variables (resolved scales, larger than the filter width) and the ones that are removed (subgrid scales, smaller than the filter width). The filtering of the nonlinear terms introduces new unknown quantities, so-called subgrid-scale terms, which require modeling to close the system of equations.
Unlike RANS, in which only the mean flow is solved and the entire turbulence is modeled, LES models only the small-scale turbulence and the filtered variables contain thus much more information than the RANS variables. LES is therefore assumed to be destined to replace RANS as the preferred predictive approach to certain types of engineering flows. A lot of work in universities and research institutes has consequently been conducted to derive subgrid-scale models which have then been tested on canonical flow configurations. In order to evaluate the models, errors from the numerical discretization have to be minimized and high-order methods were used in priority. Although this validation process constituted a necessary first step, it did not demonstrate the practicability of LES for high-Reynolds-number industrial applications where distorted meshes are common and low-order numerical methods are preferred.

In fact, rather few attempts to bridge the gap between academic research and industrial applications have been undertaken to date. The most significant effort is certainly found with the LESFOIL project (Dahlström & Davidson, 2003). The task proposed to nine European teams coming from universities and research institutes consisted in computing the flow around an airfoil at high Reynolds number using LES and revealed serious difficulties in correctly predicting the separation region and the transition from laminar to turbulent flow. Two other examples are found with the computation of Sagaut (2001) of the flow around a delta wing with vortex breakdown and the transition on a low-pressure

turbine blade. The Reynolds number was of the order of 10^6 in the first case and 10^5 in the second case and although some discrepancies with experimental data were observed for the massively separated flow over the delta wing, the flow over the turbine blade compared very well with experiments. An even more impressive computation as regards the complexity of the geometry was performed by Kato *et al.* (2001) who were interested in the flow in a mixed-flow pump and in the aeroacoustical radiation of a high-speed train pantograph insulator. For the mixed-flow pump, the predicted mean-velocity distributions at the impeller's inlet and exit cross-section were in good agreement with the measured values. The correct sound-pressure level of the pantograph insulator was more difficult to predict, and some differences with wind-tunnel measurements were noted. Massively detached flows as observed behind a car or a bus have also been lately investigated by Krajnović (2002). Due to the computational cost, the Reynolds number had to be taken smaller than in reality, but the simulations provided useful qualitative information of the unsteady structure of the flow that can not be represented by RANS.

Fruitful conclusions could be drawn from these studies and others not listed here, but reserves had also to be expressed on the wide-scale use of LES for industrial applications.

First, the computational cost of LES compared to RANS, with an estimated increase of a factor of 50 to 500 times depending on geometry and type of flow (Dahlström & Davidson, 2003), remains very expensive for today's computers. The simulation of high-Reynolds-number wall-bounded flows is even impossible as LES requires the same near-wall resolution as DNS. One way to obtain a computationally tolerable cost is to adopt an approximate non-LES treatment to bridge the viscous wall region. LES is thus applied in the outer flow region only and approximations have to be made in the viscous layer. The near-wall approximations can be based on an assumed velocity distribution linking the velocity at the wall-nearest computational node to the wall or on a RANS model. The latter method, which is usually referred to as detached-eddy simulation (DES), has been shown to alleviate successfully the near-wall grid resolution (Spalart *et al.*, 1997).

Next, improvements on subgrid-scale modeling, particularly for compressible flows, need to be achieved. In this prospect, the behavior of a recently proposed subgrid-scale model will be further evaluated in this work.

Finally, the interaction between the subgrid-scale model and the nu-

merical discretization is unclear and the problem is often eluded by selecting high-order numerical schemes for which the error is small. In this domain also, the present work will hopefully give some answers on the feasibility of LES with low-order, nondissipative, finite-volume schemes.

1.2 Objectives and outline of the present work

In a general perspective, this project aims at contributing to make LES a valuable tool for computations of industrial relevance in the future. On a lower level, the objectives of the present work are to extend the approximate deconvolution model (ADM) to the finite-volume method, to implement it in an industrial finite-volume flow solver (NSMB) and to evaluate the model for two flow configurations of increasing complexity.

ADM was developed by Stolz *et al.* (Stolz & Adams, 1999; Stolz *et al.*, 2001*a*,*b*) at the Institute of Fluid Dynamics (IFD) of the Swiss Federal Institute of Technology (ETHZ). The model is based on an approximate defiltering (deconvolution) of the filtered variables to compute the nonlinear terms and a relaxation regularization to simulate the effect of nonrepresented scales by draining energy out of the resolved scales of the flow. Since its derivation, ADM has been applied successfully to a number of canonical flow configurations. However, the simulations to date were all performed with high-order compact finite-difference or spectral schemes implemented in research codes. In the prospect of using ADM for computations of industrial interest, the model remained to be extended to the finite-volume formulation and tested with low-order numerical schemes. Two flow configurations have been chosen here for this task.

As a first test case, the turbulent channel flow at a Mach number of 1.5 and a Reynolds number (based on the bulk quantities and channel half-width) of Re_b=3000 was selected to assess the model in the challenging near-wall area. The choice of this flow configuration permits also comparisons with the DNS results of Coleman *et al.* (1995) and the LES of Lenormand *et al.* (2000).

Second, following the good results obtained for smooth wall-bounded flows, the ability of ADM with low-order schemes to accurately represent shock-turbulence interaction was investigated. Therefore the flow over a compression ramp inclined at 18° at a Mach number of 3 and a Reynolds number (based on free-stream quantities and mean momentum thickness at inflow) of Re_θ=1685 was studied and compared with the DNS results

of Adams (2000).

Due to the two distinct flow configurations addressed in this work, the thesis is written in a way that each chapter can be read independently. Each chapter contains thus a relatively explicit introduction motivating the relevance of the problem and situating it in a general context.
The outline of this thesis is as follow:

Chapter 2 begins with a recapitulation of the governing equations and an introduction to the Navier-Stokes Multi-Block (NSMB) computational code. Among the wide choice of different numerical schemes and models available in NSMB, explanations are given on the specific features used for the present computations. These include a second- and fourth-order central spatial discretization of the fluxes, an explicit four-stage Runge-Kutta temporal integration and, in one case, artificial numerical dissipation. Finally, the boundary conditions imposed by means of ghost cells are detailed.

Chapter 3 begins by presenting the ADM in a general form, as it has been derived by Stolz *et al.* The particular and new formulation of ADM for the finite-volume method is outlined next.

Chapter 4 focuses on the compressible turbulent channel flow. The results are organized in three parts. First LES with ADM is compared with filtered DNS and results from a no-model computation or under-resolved DNS. For completeness, DNS data obtained with NSMB are also displayed. Second, results with standard artificial numerical dissipation replacing the relaxation term of ADM are shown. Third, the grid dependence and the influence of the discretization order is investigated.

Chapter 5 presents the results of the supersonic flow over a compression ramp. Tests of the effect of the deconvolution order on discontinuities and turbulent fluctuations reveal that local adaptation to the flow of the deconvolution order leads to a better modeling of the energy dissipation mechanisms. A locally adapted deconvolution order is then used to compute the flow over the compression ramp and results are compared with filtered DNS. Finally, the effect of grid refinement and discretization order is examined again.

Chapter 6 summarizes the thesis, addresses open questions and future developments.

Chapter 2

Governing equations and numerical method

This chapter first introduces the Navier-Stokes equations which govern the motion of every viscous fluid. An introduction on the origin of the computational code and a nonexhaustive list of its main options is outlined as second. The specific features, such as numerical discretization, artificial dissipation, time integration and boundary conditions, used in the frame of the present work are presented next.

2.1 The compressible Navier-Stokes equations

The compressible Navier-Stokes equations describe the conservation of mass, momentum and energy of any flow field. In a three-dimensional Cartesian coordinate system (x_1, x_2, x_3), with t being the time, these equations can be expressed in conservative form as

$$\frac{\partial \mathbf{U}}{\partial t} + \frac{\partial}{\partial x_1}(\mathbf{f}_{inv} - \mathbf{f}_v) + \frac{\partial}{\partial x_2}(\mathbf{g}_{inv} - \mathbf{g}_v) + \frac{\partial}{\partial x_3}(\mathbf{h}_{inv} - \mathbf{h}_v) = 0 \quad (2.1)$$

with the inviscid fluxes $\mathbf{f}_{inv}, \mathbf{g}_{inv}, \mathbf{h}_{inv}$ and the viscous fluxes $\mathbf{f}_v, \mathbf{g}_v, \mathbf{h}_v$ in each coordinate direction. An ideal gas with density ρ^*, velocity $\mathbf{u}^* = (u_1^*, u_2^*, u_3^*)$, pressure p^*, temperature T^* and total energy E^* is considered. The nondimensionalization of the variables is obtained with a reference velocity u_{ref}^*, density ρ_{ref}^*, temperature T_{ref}^*, and length scale L_{ref}^*. The time t is nondimensionalized with L_{ref}^*/u_{ref}^*. The state vector of the conservative nondimensional variables is then given by $\mathbf{U} = (\rho, \rho u_1, \rho u_2, \rho u_3, E)$, the convective fluxes are defined as

$$\mathbf{f}_{inv} = \begin{pmatrix} \rho u_1 \\ \rho u_1^2 + p \\ \rho u_1 u_2 \\ \rho u_1 u_3 \\ u_1(E+p) \end{pmatrix}, \mathbf{g}_{inv} = \begin{pmatrix} \rho u_2 \\ \rho u_2 u_1 \\ \rho u_2^2 + p \\ \rho u_2 u_3 \\ u_2(E+p) \end{pmatrix}, \mathbf{h}_{inv} = \begin{pmatrix} \rho u_3 \\ \rho u_3 u_1 \\ \rho u_3 u_2 \\ \rho u_3^2 + p \\ u_3(E+p) \end{pmatrix}, \quad (2.2)$$

and the viscous fluxes as

$$\mathbf{f}_v = \begin{pmatrix} 0 \\ \tau_{11} \\ \tau_{12} \\ \tau_{13} \\ (\tau\mathbf{u})_1 - q_1 \end{pmatrix}, \mathbf{g}_v = \begin{pmatrix} 0 \\ \tau_{21} \\ \tau_{22} \\ \tau_{23} \\ (\tau\mathbf{u})_2 - q_2 \end{pmatrix}, \mathbf{h}_v = \begin{pmatrix} 0 \\ \tau_{31} \\ \tau_{32} \\ \tau_{33} \\ (\tau\mathbf{u})_3 - q_3 \end{pmatrix}. \tag{2.3}$$

The shear stress tensor τ_{ij} is given by (the summation rule applies and $\delta_{ij} = 1$ for $i = j$ and 0 otherwise, $i, j = 1, 2, 3$)

$$\tau_{ij} = \frac{\mu(T)}{Re}\left(\frac{\partial u_i}{\partial x_j} + \frac{\partial u_j}{\partial x_i} - \frac{2}{3}\delta_{ij}\frac{\partial u_k}{\partial x_k}\right) \tag{2.4}$$

where $\mu(T)$ is the nondimensional viscosity and $Re = u^*_{ref}\rho^*_{ref}L^*_{ref}/\mu^*_{ref}$ the Reynolds number. The viscous dissipation in the energy equation can be calculated from

$$(\tau\mathbf{u})_i = \tau_{i1}u_1 + \tau_{i2}u_2 + \tau_{i3}u_3 \tag{2.5}$$

and the heat flux due to conduction is given by

$$q_i = -\frac{\mu(T)}{(\gamma-1)RePrM^2_{ref}}\frac{\partial T}{\partial x_i}, \tag{2.6}$$

where Pr is the Prandtl number (for air Pr=0.72), $\gamma = c_p/c_v$=1.4 the ratio of specific heats, and M_{ref} the reference Mach number. The nondimensional viscosity $\mu(T)$ is calculated from Sutherland's law

$$\mu(T) = T^{3/2}\frac{1+s}{T+s}, \tag{2.7}$$

where s is a parameter depending on the gas and the temperature range, set here to $110.3K/T^*_{ref}$ for air. Closure of the Navier-Stokes equations still requires the calculation of the pressure. For a calorically perfect gas, the pressure is related to the conservative variables through

$$p = (\gamma-1)E - \frac{\gamma-1}{2}\rho(u_1^2 + u_2^2 + u_3^2). \tag{2.8}$$

Finally, the temperature can be calculated with the thermal equation of state for perfect gases,

$$T = \frac{\gamma M^2_{ref}p}{\rho}. \tag{2.9}$$

2.2 The NSMB computer code

All numerical simulations presented in this work have been performed with the NSMB flow solver which has jointly been developed by the Fluid Mechanics Laboratory (LMF) of the Swiss Federal Institute of Technology (EPFL) in Lausanne, SAAB and the Royal Institute of Technology (KTH) in Sweden, and Aérospatiale and CERFACS in Toulouse.
The NSMB code, extensively described in Vos *et al.* (2000), has a block-parallel and vectorial structure and has been used on high-performance computers to solve complex industrial aerodynamic design tasks like the external-flow simulation around the Hermes space-shuttle (Vos *et al.*, 1993) various aeronautical computations for Airbus airplanes (Gacherieu *et al.*, 2000; Viala *et al.*, 2002) or internal-flow simulations for high speed-trains in tunnels (Mossi, 1999). We give here a nonexhaustive list of the options on the physical and numerical level of NSMB for an overview of the possibilities offered by the flow solver.

NSMB solves the compressible Navier-Stokes equations with a cell-centered finite-volume method. The resolution of the full Navier-Stokes equations leads to so-called DNS and is only feasible for low-Reynolds-number flows. Although a DNS of the channel flow at a Reynolds number of 3000 has been computed with NSMB in the present work (see chapter 4), computations at higher Reynolds numbers remain too expensive for DNS. Therefore alternatives to lower the computational cost have been developed in which subgrid-scale (in LES) or turbulence models (in RANS) account for the reduced resolution of the flow.
The Smagorinsky model (Smagorinsky, 1963, 1993) and the structure function model of Métais & Lesieur (1992) have recently been implemented in NSMB as regards LES subgrid-scale models. The implementation and validation of the ADM of Stolz *et al.* (chapter 3) constitutes furthermore the topic of the present work.
For RANS methods, numerous models are available in NSMB due to the industrial background of the code. The algebraic model of Baldwin-Lomax or Granville, the one-equation model of Spalart-Allmaras and the two-equation models such as $k-\epsilon$ or $k-\omega$ can be cited among others (see Wilcox (1994) for a survey of RANS turbulence models).

Concerning the numerical discretization, a large number of different spatial and temporal schemes have been implemented in the code. In the frame of this work, only Jameson-type (Jameson *et al.*, 1981) schemes which combine a central discretization of the spatial derivatives and an

explicit Runge-Kutta time integration have been used. A wide choice of upwind, total variation diminishing (TVD), nonoscillatory schemes (ENO, WENO) are also available. Temporal integration can be performed by means of explicit or implicit methods, or dual time stepping in case of unsteady RANS computations.
Finally several methods such as residual smoothing or multigrid can be switched on to accelerate the convergence.

2.3 Finite-volume discretization

In order to correctly capture discontinuities, it is important that the discretized Navier-Stokes equations also satisfy a conservative formulation (Lax & Wendroff, 1960). Integration of eq. (2.1) over a volume V yields

$$\int_V \frac{\partial \mathbf{U}}{\partial t} d\mathcal{V} + \int_V \nabla \cdot \mathbb{F}(\mathbf{U})\, d\mathcal{V} = 0\,, \tag{2.10}$$

where $\mathbb{F} = (\mathbf{f}_{inv} - \mathbf{f}_v, \mathbf{g}_{inv} - \mathbf{g}_v, \mathbf{h}_{inv} - \mathbf{h}_v)$ is the flux tensor. Application of the Gauss theorem yields

$$\int_V \frac{\partial \mathbf{U}}{\partial t} d\mathcal{V} + \int_S \mathbb{F}(\mathbf{U})\, \mathbf{n}\, d\mathcal{S} = 0\,, \tag{2.11}$$

where $\mathbf{n}$ is the unit normal pointing in the outward direction of the cell surface S of the volume V. Equation (2.11) states that the time rate of change of $\mathbf{U}$ in the domain V is equal to the sum of the fluxes entering and leaving V at the boundaries S. Let us define V in a Cartesian space as the volume of a cell with indices i, j, k and consider

$$\mathbf{U}_{i,j,k} = 1/V_{i,j,k} \int_{V_{i,j,k}} \mathbf{U} d\mathcal{V}\,, \tag{2.12}$$

located in the center of the cell, as the average of $\mathbf{U}$ in this cell. Then eq. (2.11) can be approximated by

$$\frac{d}{dt}(V_{i,j,k}\mathbf{U}_{i,j,k}) + \mathbf{F}_{i,j,k} = 0\,. \tag{2.13}$$

$\mathbf{F}_{i,j,k}$ is the net flux leaving and entering the cell i, j, k,

$$\begin{aligned} \mathbf{F}_{i,j,k} \quad = \quad & \mathbf{f}_{i+1/2,j,k} - \mathbf{f}_{i-1/2,j,k} + \mathbf{f}_{i,j+1/2,k} \\ & -\mathbf{f}_{i,j-1/2,k} + \mathbf{f}_{i,j,k+1/2} - \mathbf{f}_{i,j,k-1/2}\,, \end{aligned} \tag{2.14}$$

where $\mathbf{f}_{i-1/2,j,k}$ is the flux oriented in the I-direction at the cell surface S_{ABCD} (see figure 2.1). The flux at this cell side is defined as

$$\mathbf{f}_{i-1/2,j,k} = \int_{ABCD} \mathbb{F}(\mathbf{U})\,\mathbf{n}\,d\mathcal{S} \tag{2.15}$$

representing the integral on the surface S_{ABCD} of the scalar product between the flux tensor $\mathbb{F}(\mathbf{U})$ and the unit surface normal $\mathbf{n}$. This equals the flux projected on the surface, which represents respectively the mass flow, the momentum flow, and energy flow through the cell surface side S_{ABCD}. The next step is to approximate the value of the flux tensor $\mathbb{F}(\mathbf{U})$ at the surface S_{ABCD} in eq. (2.15). A distinction is made between the inviscid and viscous part of the flux tensor. The inviscid flux is discretized through a central second- or fourth-order scheme, whereas the gradients of the viscous flux are always calculated with a second-order scheme.

2.3.1 Inviscid flux calculation

The discretization of the inviscid flux tensor $\mathbb{F}_{inv} = (\mathbf{f}_{inv}, \mathbf{g}_{inv}, \mathbf{h}_{inv})$ plays a large role in the stability of the numerical scheme. It has been observed that the divergence formulation could lead to unstable computations whereas the skew-symmetric formulation, due to its intrinsic dealiasing property, has a beneficial effect on the stability of the computation (Blaisdell *et al.*, 1996). For this reason, the latter form has been used in the present work. Considering for simplicity a generic one-dimensional transport equation $\partial u/\partial t + \partial f/\partial x = 0$ with the flux $f = uv$, the skew-symmetric formulation of the flux is given by:

$$\left[\frac{\partial f}{\partial x}\right]^{skew} = \frac{1}{2}\left(\frac{\partial uv}{\partial x}\right) + \frac{1}{2}\left(u\frac{\partial v}{\partial x} + v\frac{\partial u}{\partial x}\right). \tag{2.16}$$

The discrete flux difference $(f_{i+1/2} - f_{i-1/2})/\Delta x$ has to be of the same form as the continuous flux (eq. 2.16). For a second-order discretization, this is achieved by taking the average value of u and v for the flux at the cell faces, i.e.,

$$f_{i+1/2} = f(u_{i+1/2}, v_{i+1/2}) = \frac{u_i + u_{i+1}}{2}\frac{v_i + v_{i+1}}{2}, \tag{2.17}$$

$$f_{i-1/2} = f(u_{i-1/2}, v_{i-1/2}) = \frac{u_i + u_{i-1}}{2}\frac{v_i + v_{i-1}}{2}. \tag{2.18}$$

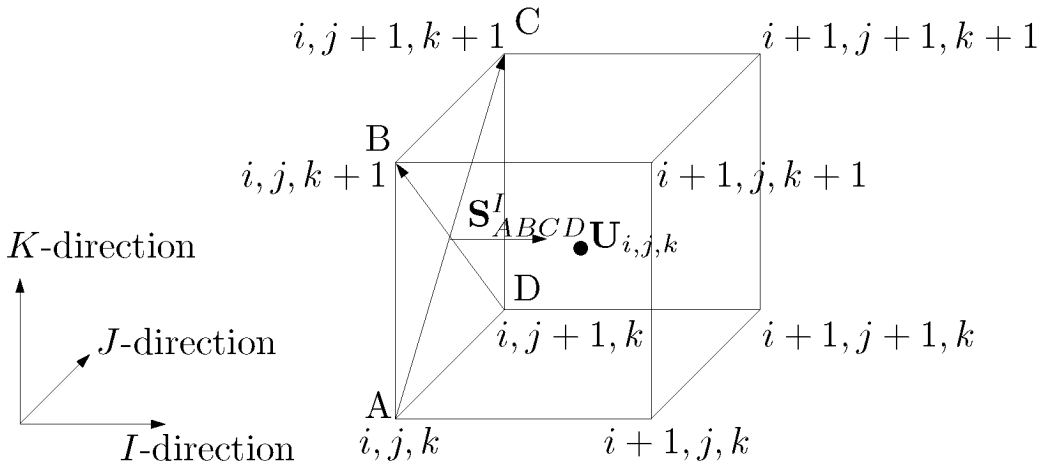

Figure 2.1: Definition of a finite-volume cell. $\mathbf{U}_{i,j,k}$ *is the cell-average value located in the center of the cell with volume* $V_{i,j,k}$. $\mathbf{S}^I_{ABCD}$ *is the surface vector in the* I*-direction of the cell face* S_{ABCD}.

Using eq. (2.17) and (2.18), the discrete flux becomes thus:

$$\frac{f_{i+1/2} - f_{i-1/2}}{\Delta x} = \frac{1}{2}\left(\frac{u_{i+1}v_{i+1} - u_{i-1}v_{i-1}}{2\Delta x}\right) + \frac{1}{2}\left(u_i \frac{v_{i+1} - v_{i-1}}{2\Delta x} + v_i \frac{u_{i+1} - u_{i-1}}{2\Delta x}\right) \tag{2.19}$$

which is the centrally discretized form of eq. (2.16).
The expression of the discrete flux for a fourth-order accuracy is developed in Ducros *et al.* (2000) and is given here without further details (similarly for $i - 1/2$),

$$f_{i+1/2} = \frac{1}{3}(u_i + u_{i+1})(v_i + v_{i+1}) - \frac{1}{24}(u_{i-1}v_{i-1} + u_{i-1}v_{i+1} + u_i v_i + u_i v_{i+2} + u_{i+1}v_{i+1} + u_{i+1}v_{i-1} + u_{i+2}v_i + u_{i+2}v_{i+2}). \tag{2.20}$$

The extension to the Navier-Stokes equations is obtained by replacing u and v in the above expressions by the corresponding variables, e.g., $u = \rho u_1$ and $v = u_1, u_2, u_3$ for the momentum in x_1 direction.

2.3.2 Viscous flux calculation

The viscous flux tensor $\mathbb{F}_v = (\mathbf{f}_v, \mathbf{g}_v, \mathbf{h}_v)$ is calculated using eq. (2.3), where the velocity gradients in the shear stresses and the temperature

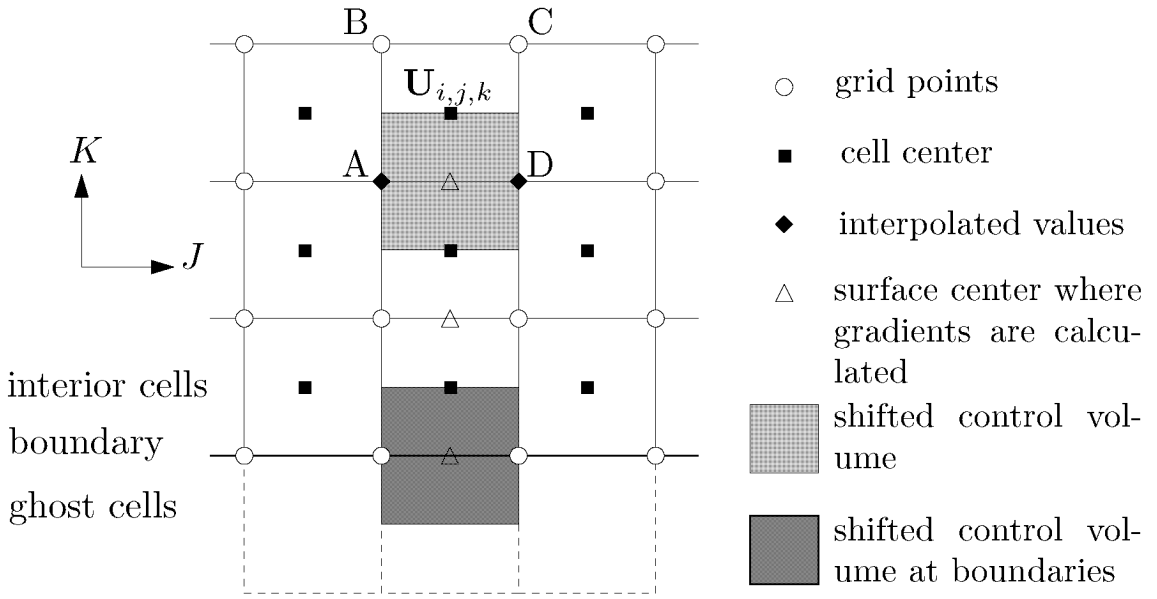

Figure 2.2: 2D grid layout used for the calculation of the gradients in the K-direction.

gradients in the heat flux are calculated at the surface center using the gradient theorem on a shifted control volume V^s with surface S^s (figure 2.2) (Peyret & Taylor, 1983)

$$\nabla\phi = \int_{V^s} \nabla\phi d\mathcal{V} \,/\, \int_{V^s} d\mathcal{V} = \frac{1}{V^s} \int_{S^s} \phi\, \mathbf{n}\, d\mathcal{S}^s \,. \tag{2.21}$$

In the above equation, the values of ϕ at the cell centers are directly available whereas the values at the cell corners are obtained by the averaging of the values from the neighboring cells.

2.4 Artificial numerical dissipation

Central schemes need to be augmented by the addition of artificial numerical dissipation to capture accurately discontinuities and damp high-frequency oscillations. Different forms of numerical dissipation exist. The most simple is the original scalar version of Jameson *et al.* (1981) where the dissipation is scaled with a scalar factor determined by the spectral radius of the Jacobian matrix for the inviscid flux across the cell face. This model has proven to be effective for many industrial applications but too dissipative for LES computations as Garnier *et al.* (1999)

have shown and as it has been confirmed here by several tests. To diminish the numerical dissipation, an improved model has been proposed by Swanson & Turkel (1992) where the dissipation is scaled by the appropriate eigenvalue of the flux Jacobian matrices of the Euler equations rather than the same spectral radius as for the scalar version of Jameson.

In the following, only the improved matrix dissipation is presented. A second-order artificial viscosity is used near discontinuities, and a fourth-order dissipation term to suppress odd/even oscillations. The dissipation terms use the second and fourth differences of the state vector $\mathbf{U}$ multiplied by the Jacobian matrix of the inviscid flux acting as a scaling matrix and a weight, the latter usually referred to as a switch. This switch is formed with the absolute value of the normalized second difference of the pressure, implying that the second-order term is small except in regions of large pressure gradients, as found in the neighborhood of shocks or stagnation points. The fourth-order dissipation term acts everywhere, except in regions where the second-order dissipation term is large, in order to prevent oscillations. After addition of the dissipative terms, the transport equation (2.11) results in

$$\int_V \frac{\partial \mathbf{U}}{\partial t} d\mathcal{V} + \int_S \mathbb{F}(\mathbf{U}) \cdot \mathbf{n}\, d\mathcal{S} - \mathbf{D}(\mathbf{U}) = 0 \ , \tag{2.22}$$

where $\mathbf{D}$ stands for the dissipation operator. Analogous to the discretization of the fluxes, the operator $\mathbf{D}$ can be split in its cell surface components as

$$\begin{aligned} \mathbf{D}_{i,j,k} \quad = \quad & \mathbf{d}_{i+1/2,j,k} - \mathbf{d}_{i-1/2,j,k} + \mathbf{d}_{i,j+1/2,k} \\ & - \mathbf{d}_{i,j-1/2,k} + \mathbf{d}_{i,j,k+1/2} - \mathbf{d}_{i,j,k-1/2} \ . \end{aligned} \tag{2.23}$$

The dissipative flux in I-direction at the cell side $i-1/2, j, k$ is calculated from

$$\begin{aligned} \mathbf{d}_{i-1/2,j,k} = |\mathbb{A}_{i-1/2,j,k}|[\varepsilon^{(2)}_{i-1/2,j,k}(\mathbf{U}_{i,j,k} - \mathbf{U}_{i-1,j,k}) - \\ \varepsilon^{(4)}_{i-1/2,j,k}(\mathbf{U}_{i+1,j,k} - 3\mathbf{U}_{i,j,k} + 3\mathbf{U}_{i-1,j,k} - \mathbf{U}_{i-2,j,k})] \cdot S_{i-1/2,j,k} \end{aligned} \tag{2.24}$$

and analogous expressions for the J- and K-directions are used. In eq. (2.24) $\mathbb{A}$ is the scaling matrix which depends on the absolute value of the eigenvalues for each equation and ε is the weight mentioned previously.

The scaling matrix $\mathbb{A}$ is defined from the relation

$$|\mathbb{A}_{i-1/2,j,k}| = \mathbb{T}_{i-1/2,j,k}|\mathbb{L}_{i-1/2,j,k}|\mathbb{T}^{-1}_{i-1/2,j,k} \tag{2.25}$$

where $\mathbb{L}_{i-1/2,j,k}$ is the diagonal matrix of eigenvalues and $\mathbb{T}_{i-1/2,j,k}$ the matrix of right eigenvectors at the cell surface $i-1/2, j, k$. If we define the increment of the conservative variables as $\delta\mathbf{U}$, the increment of the primitive variable as $\delta\mathbf{V}$, and the increment of the characteristic variables as $\delta\mathbf{W}$, then the matrix $\mathbb{T}$ is computed as

$$\mathbb{T} = \left(\frac{\delta\mathbf{V}}{\delta\mathbf{W}}\right)\left(\frac{\delta\mathbf{U}}{\delta\mathbf{V}}\right) . \tag{2.26}$$

For the sake of simplicity and efficiency, the vector differentiation and multiplication is replaced by the analytical formulas for the actual implementation (see chapter 16 of Hirsch (1990) and Vos *et al.* (2000)). The diagonal matrix of eigenvalues $\mathbb{L} = diag[\lambda_1, \lambda_2, \lambda_3, \lambda_4, \lambda_5]$ reads as follow:

$$\mathbb{L} = \begin{pmatrix} \mathbf{u}\cdot\mathbf{S} & \cdot & \cdot & \cdot & \cdot \\ \cdot & \mathbf{u}\cdot\mathbf{S} & \cdot & \cdot & \cdot \\ \cdot & \cdot & \mathbf{u}\cdot\mathbf{S} & \cdot & \cdot \\ \cdot & \cdot & \cdot & \mathbf{u}\cdot\mathbf{S}+c|\mathbf{S}| & \cdot \\ \cdot & \cdot & \cdot & \cdot & \mathbf{u}\cdot\mathbf{S}-c|\mathbf{S}| \end{pmatrix} \tag{2.27}$$

where $\mathbf{u}$ is the velocity vector, c the speed of sound and $|\mathbf{S}|$ the norm of the surface vector of the considered cell. To avoid numerical instabilities near stagnation points or sonic lines, where at least one of the eigenvalues approaches zero, Swanson & Turkel (1992) proposed limits on the eigenvalues based on the use of the spectral radius $\rho(\mathbb{A}) = \mathbf{u}\cdot\mathbf{S} + c|\mathbf{S}|$

$$\begin{aligned} |\lambda_i| &= max(|\lambda_i|, e_1\cdot\rho(\mathbb{A}))\,, \qquad i = 1,2,3 \\ |\lambda_4| &= max(|\lambda_2|, e_2\cdot\rho(\mathbb{A})) \\ |\lambda_5| &= max(|\lambda_3|, e_3\cdot\rho(\mathbb{A})) \end{aligned} \tag{2.28}$$

where the factors e_1, e_2 and e_3 have been set here equal to 0.05, 0.2 and 0.2 respectively (Swanson & Turkel, 1992).

The second- and fourth-order coefficients $\varepsilon^{(2)}$ and $\varepsilon^{(4)}$ adapt locally the dissipative fluxes depending on sharp gradients possibly present in the flow. As mentioned before, the second-order dissipation is directly

related to the normalized second-order difference of the pressure gradient. In the I-direction, this difference reads:

$$\Delta^p_{i,j,k} = \left| \frac{p_{i+1,j,k} - 2p_{i,j,k} + p_{i-1,j,k}}{p_{i+1,j,k} + 2p_{i,j,k} + p_{i-1,j,k}} \right| . \tag{2.29}$$

The switch is found from

$$\nu_{i-1/2,j,k} = \max(\Delta^p_{i-1,j,k}, \Delta^p_{i,j,k}) \tag{2.30}$$

and takes the largest second difference of the pressure in two points on each flux side. $\varepsilon^{(2)}$ and $\varepsilon^{(4)}$ are then defined as

$$\varepsilon^{(2)}_{i-1/2,j,k} = k^{(2)} \nu_{i-1/2,j,k} \tag{2.31}$$

$$\varepsilon^{(4)}_{i-1/2,j,k} = \max(0.0, k^{(4)} - \varepsilon^{(2)}_{i-1/2,j,k}) . \tag{2.32}$$

In this way, the fourth-order dissipation is automatically switched off in the vicinity of a discontinuity, where the second-order dissipation is large. The expressions for J- and K- directions are analogous. The parameters $k^{(2)}$ and $k^{(4)}$ are user-defined constants used to control the dissipation. Typical values range from 0.5 to 2.0 for $k^{(2)}$ and from 0.01 to 0.05 for $k^{(4)}$ (Vos *et al.*, 2000).

2.5 Time integration

The set of partial differential equations (2.13) is integrated in time explicitely with a low-storage four-stage Runge-Kutta method which is formally fourth-order accurate for linear equations but drops to second-order accuracy for a general nonlinear equation.
Assuming that the cell volume is constant and adding the total flux term $\mathbf{F}_{i,j,k}$ with possible dissipation terms and source terms to the residual $\mathbf{R}_{i,j,k}$, we can rewrite eq. (2.13) as

$$\frac{d}{dt}\mathbf{U}_{i,j,k} + \frac{1}{V_{i,j,k}}\mathbf{R}_{i,j,k} = 0. \tag{2.33}$$

Applying a q-stage Runge-Kutta scheme ($q \leqslant 5$) to the above equation yields

$$\begin{aligned}
\mathbf{U}_{i,j,k}^{n+1/q} &= \mathbf{U}_{i,j,k}^{n} - \beta\varphi_1 \frac{\Delta t_{i,j,k}}{V_{i,j,k}} \mathbf{R}(\mathbf{U}_{i,j,k}^{n+0/q}) \\
\mathbf{U}_{i,j,k}^{n+2/q} &= \mathbf{U}_{i,j,k}^{n} - \beta\varphi_2 \frac{\Delta t_{i,j,k}}{V_{i,j,k}} \mathbf{R}(\mathbf{U}_{i,j,k}^{n+1/q}) \\
&\vdots \\
\mathbf{U}_{i,j,k}^{n+1} &= \mathbf{U}_{i,j,k}^{n} - \beta\varphi_q \frac{\Delta t_{i,j,k}}{V_{i,j,k}} \mathbf{R}(\mathbf{U}_{i,j,k}^{n+(q-1)/q}) \,, \qquad (2.34)
\end{aligned}$$

where $\varphi_i = 1, ..., q$ are the coefficients of the q-stage Runge-Kutta scheme and β the Courant-Friedrichs-Lewy (CFL) number. For a four-stage scheme (q=4), the coefficients φ_i are

$$\varphi_1 = 1/4 \,,\ \varphi_2 = 1/3 \,,\ \varphi_3 = 1/2 \,,\ \varphi_4 = 1 \qquad (2.35)$$

giving a maximal theoretical CFL number of 2.8.

The exact computation of the time step that ensures stability requires the numerical analysis of the eigenvalues of the amplification matrix of the numerical scheme (Hirsch, 1990). Here a simplified analysis is followed. A distinction is made between the time step limit associated with the inviscid fluxes $\Delta t_{i,j,k}^{inv}$, and the time step limit associated with the viscous fluxes $\Delta t_{i,j,k}^{v}$. The local time step is then taken as the minimum of the inviscid and viscous time step,

$$\beta\Delta t_{i,j,k} = \min\left(CFL_{inv}\Delta t_{i,j,k}^{inv}, CFL_v\Delta t_{i,j,k}^{v}\right) \qquad (2.36)$$

where CFL_{inv} and CFL_v are respectively the CFL number for the inviscid and the viscous time step. For steady calculations the maximum allowable time step $\Delta t_{i,j,k}$ is taken for each cell, whereas for unsteady problems, the minimum time step among all the cells is used for all the cells.

The physical background of the inviscid time step using an explicit scheme is based on the advection between mesh cells. The reasoning is that one can not take a larger time step than the time required for the information to pass from one cell to its neighboring cell. This implies that if the flux through the cell is increased, the time step is decreased. The volume of the cell is used to estimate the cell size and the largest

eigenvalue of the Jacobian matrix of the inviscid flux across the cell face (eq. 2.27) is used to estimate the flux trough the cell leading to

$$\Delta(t^{inv}_{i,j,k})^I = \frac{V_{i,j,k}}{\lambda^I_{i,j,k}} \tag{2.37}$$

where $\lambda^I_{i,j,k} = \mathbf{u}_{i,j,k} \cdot \mathbf{S}^I_{i,j,k} + c|\mathbf{S}^I_{i,j,k}|$ with $\mathbf{S}^I_{i,j,k}$ being the average surface vector in the I-direction (average over the cell face $i-1/2$ and $i+1/2$, analogous for the J- and K-direction).
The inviscid time step is then computed as

$$\frac{1}{\Delta t^{inv}_{i,j,k}} = \frac{1}{(\Delta t^{inv}_{i,j,k})^I} + \frac{1}{(\Delta t^{inv}_{i,j,k})^J} + \frac{1}{(\Delta t^{inv}_{i,j,k})^K} \,. \tag{2.38}$$

The viscous time step is calculated from Müller & Rizzi (1990)

$$\Delta t^{vis}_{i,j,k} = \frac{\rho_{i,j,k} V^2_{i,j,k}}{\max\left(\frac{4}{3}\mu_{i,j,k}, \frac{\gamma-1}{R} k_{i,j,k}\right) \Omega_{i,j,k}} \tag{2.39}$$

where R is the gas constant, μ the viscosity, k the thermal conductivity and

$$\begin{aligned} \Omega_{i,j,k} \;=\; & (S^I_1)^2 + (S^I_2)^2 + (S^I_3)^2 + (S^J_1)^2 + (S^J_2)^2 + (S^J_3)^2 + \\ & (S^K_1)^2 + (S^K_2)^2 + (S^K_3)^2 + \left|S^I_1 S^J_1 + S^I_2 S^J_2 + S^I_3 S^J_3\right| + \\ & \left|S^I_1 S^K_1 + S^I_2 S^K_2 + S^I_3 S^K_3\right| + \left|S^J_1 S^K_1 + S^J_2 S^K_2 + S^J_3 S^K_3\right| \,, \end{aligned} \tag{2.40}$$

with S^I_1 being the x_1 component of the average surface vector in the I-direction, and similarly for the other indices (subscripts i, j, k were dropped on the right hand side for sake of clarity).

2.6 Boundary conditions

Boundary conditions are implemented by means of two rows of ghost cells added outside the computational domain. The values of the state vector $\mathbf{U}$ in these cells are determined by the physical and numerical boundary conditions. Physical values for the ghost cells are only possible for free-stream boundary conditions - for periodic or wall boundary conditions for example, no physical values for the ghost cells exist and

extrapolation procedures have to be defined. In this work the following boundary conditions have been used: Dirichlet (e.g. prescribed inflow conditions), periodic, solid surface and characteristic boundary conditions.
In this section, the variables in the first and second ghost cells will be designated by the subscript 0 and -1 respectively whereas the subscript 1 and 2 will stand for the variables in the first and second inner cells of the computational domain.
The application of Dirichlet and periodic conditions is straightforward. In the first case, the first row of cells of the computational domain is prescribed by the Dirichlet boundary conditions and the first and second row of ghost cells are filled with the same value so as to set every gradient to zero.
For the periodic conditions, assuming a periodicity of N cells, the first row of ghost cell is set to $\mathbf{U}_0 = \mathbf{U}_N$ and the second row is set to $\mathbf{U}_{-1} = \mathbf{U}_{N-1}$. The ghost cells $N+1$ and $N+2$ are filled in a similar way.
The solid wall and the characteristic boundary conditions are more involved and are outlined hereafter.

2.6.1 Solid surface boundary

At a solid surface, the only physical boundary condition required is the no-slip condition, i.e., the three velocity components vanish at the wall. From this condition it follows that the only contribution to the convective fluxes comes from the pressure. Here, it has been chosen to set the pressure gradient normal to the wall zero, i.e. $p_w = p_1$. The state vector in the first and second ghost cells is defined as,

$$\begin{aligned} \rho_0 &= \rho_1 & \qquad \rho_{-1} &= \rho_2 \\ (\rho u)_0 &= -(\rho u)_1 & \qquad (\rho u)_{-1} &= -(\rho u)_2 \\ (\rho v)_0 &= -(\rho v)_1 & \qquad (\rho v)_{-1} &= -(\rho v)_2 \\ (\rho w)_0 &= -(\rho w)_1 & \qquad (\rho w)_{-1} &= -(\rho w)_2 \\ E_0 &= E_1 & \qquad E_{-1} &= E_2 \end{aligned} \tag{2.41}$$

which enforces a zero density and energy gradient, and zero velocity at the wall. Boundary conditions for the temperature depend on whether the wall is adiabatic or isothermal, in the first case the normal temperature gradient is set to zero and in the second case

$$T_0 = 2T_w - T_1 \,. \tag{2.42}$$

A proper boundary condition is more difficult to find for the artificial dissipation because no physical value exists inside the ghost cells. Usually, the boundary conditions are prescribed so that the artificial dissipation, vanishes at the wall. This implies from eq. (2.24) that

$$\mathbf{U}_2 - 3\mathbf{U}_1 + 3\mathbf{U}_0 - \mathbf{U}_{-1} = 0\,, \tag{2.43}$$

and from eq. (2.23)

$$\mathbf{d}_{-1/2} = \mathbf{d}_{1/2} \;\Rightarrow\; \mathbf{U}_1 - 2\mathbf{U}_0 + \mathbf{U}_{-1} = 0 \tag{2.44}$$

which determines $\mathbf{U}_{-1}$ and $\mathbf{U}_0$. Note that it is not possible to fill the ghost cells in order to satisfy simultaneously the boundary conditions for the inviscid (eq. 2.41), viscous (eq. 2.42) and artificial dissipative fluxes (eq. 2.43 and 2.44). Therefore, the ghost cells are updated to fulfill the proper boundary conditions in each time step before the inviscid, viscous and artificial dissipative fluxes are computed.

2.6.2 Characteristic boundary conditions

Appropriate far-field or free-stream boundary conditions have to be imposed when an infinite physical flow domain is restricted to a finite computational domain. It is important for the convergence to steady state that the waves leaving the computational domain do not reenter it after reflection caused by the boundaries. To avoid the reflection of the outgoing waves, the conservative variables are extrapolated using characteristic variables. A detailed discussion of this method can be found in Hirsch (1990) and is only summarized here. The propagation of waves and disturbances is connected to the convective part of the Navier-Stokes equations, and for this reason only the Euler equations are considered here. In quasi-linear form and written with primitive variables $\mathbf{V} = (\rho, u_1, u_2, u_3, p)$, the Euler equations can be expressed as

$$\frac{\partial V}{\partial t} + \mathbb{A} \cdot \nabla \mathbf{V} = 0 \tag{2.45}$$

where $\mathbb{A}$ is the Jacobian matrix. The eigenvalues of this Jacobian matrix can be found by solving

$$\det|\lambda I - \mathbb{A} \cdot \mathbf{n}| = 0 \tag{2.46}$$

where $\mathbf{n}$ is the propagation direction of the waves. It is well-known (Hirsch, 1990) that the Euler equations have the following eigenvalues

$$\begin{aligned} \lambda_i &= \mathbf{u}\cdot\mathbf{n}, \qquad i = 1,2,3 \\ \lambda_4 &= \mathbf{u}\cdot\mathbf{n} + c \\ \lambda_5 &= \mathbf{u}\cdot\mathbf{n} - c \end{aligned} \tag{2.47}$$

where c is the speed of sound and $\mathbf{u}$ is the velocity vector. The eigenvalues determine the slope of the characteristics C_-, C_0, C_+ and thereby whether they enter or leave the computational domain. Since each characteristic direction can be considered as transporting a given information, expressed as a combination of primitive variables, the quantities transported from the inside of the domain towards the boundary will influence and modify the situation along this boundary. Hence, only variables transported from the boundaries towards the interior can be freely imposed as physical boundary conditions. The remaining variables will depend on the computed flow situations and are therefore part of the solution. However, from a numerical point of view, the only available physical boundary conditions are not sufficient to fill completely the state vector of the ghost cells at time level $t = n$ and in order to compute the solution at time $t = n + 1$, the state vector has to be completed in the ghost cells with numerical boundary conditions.
In figure 2.3 the characteristics C_+ and C_0 leave the computational domain whereas the characteristic C_- enters it, indicating that in this case one quantity can be freely set but two others are determined by the inner flow. Along each of these characteristics certain quantities, the Riemann invariants (Hirsch, 1990), are constants for linear systems. The Riemann invariant from the first interior cell is thus copied into the first ghost cell if the characteristic is outgoing. For the characteristic C_0 corresponding to the eigenvalue $\lambda_{1,2,3} = \mathbf{u}\cdot\mathbf{n}$, we have

$$(\mathbf{u}_t)_0 = (\mathbf{u}_t)_1 \tag{2.48}$$

$$\left(\frac{p}{\rho^\gamma}\right)_0 = \left(\frac{p}{\rho^\gamma}\right)_1 \tag{2.49}$$

i.e. conserved tangent velocity and entropy. For the characteristic C_- corresponding to the eigenvalue $\lambda_4 = \mathbf{u}\cdot\mathbf{n} - c$, we have

$$\left(\|\mathbf{u}_n\| - \frac{2c}{\gamma-1}\right)_0 = \left(\|\mathbf{u}_n\| - \frac{2c}{\gamma-1}\right)_1 \tag{2.50}$$

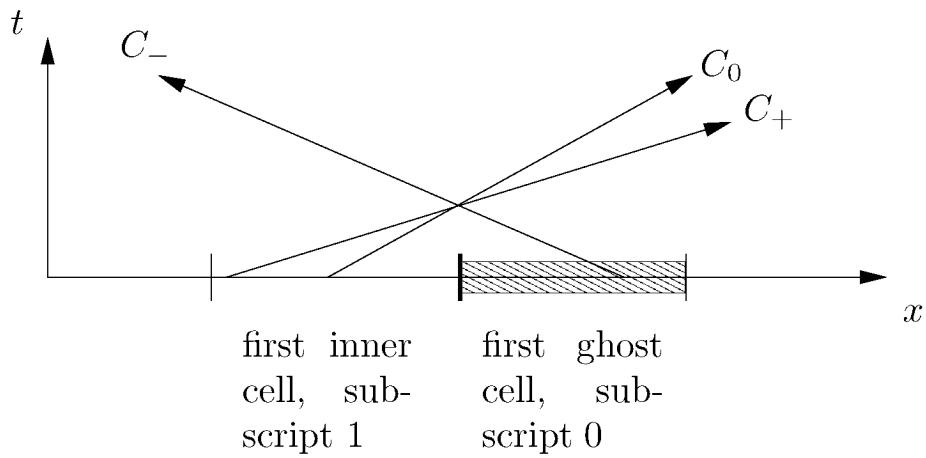

Figure 2.3: 1-D sketch of characteristics entering and leaving the computational domain at the boundary.

where $\mathbf{u}_n$ is the velocity normal to the boundary. For the characteristic C_+ corresponding to the eigenvalue $\lambda = \mathbf{u} \cdot \mathbf{n} + c$, we have

$$\left(\|\mathbf{u}_n\| + \frac{2c}{\gamma - 1} \right)_0 = \left(\|\mathbf{u}_n\| + \frac{2c}{\gamma - 1} \right)_1 . \tag{2.51}$$

From these relations it is possible to compute the speed of sound by subtracting eq. (2.50) and (2.51), and the velocity $\mathbf{u}$ by adding eq. (2.50) and (2.51) and using the known value of the tangent velocity $\mathbf{u}_t$. With help of the known entropy it is then possible to fully reconstruct the state vector in the ghost cells.
For ingoing characteristics, the value in the ghost cell can be freely imposed and the free-stream values are chosen here.
Similarly to the solid surface boundary conditions, the boundary conditions for the inviscid, viscous and artificial dissipative fluxes can not be satisfied simultaneously. Therefore, if the artificial numerical dissipation is activated, values for the ghost cells are subsequently overwritten according to eq. (2.43) and (2.44).

Chapter 3

Large-eddy simulation

For nearly four decades, LES has been the subject of increasing interest and research as it appears to be the most promising approach to circumvent the limitations of RANS and DNS. As a matter of fact, on the one hand unsteady turbulent motions averaged out with RANS models can be captured accurately with LES and on the other hand, the computational cost is significantly smaller than with DNS, allowing for computations of flows at higher Reynolds number.

In LES, the large three-dimensional unsteady turbulent motions are represented accurately on the computational mesh whereas the effect of the small scales has to be modeled. The separation of the large scales and the small scales is obtained by applying a low-pass filter to the Navier-Stokes equations. Any flow variable f can then be decomposed as $f = \overline{f} + f'$ where $\overline{f}$ represents the resolved scales (scales smaller than the low-pass filter cutoff ω_c), and f' the unresolved scales. The filtered quantity $\overline{f}$ is obtained by a convolution product with the filter kernel G_1 as

$$\overline{f}(x) = G_1 * f = \int G_1(x - x') f(x')\, dx' \tag{3.1}$$

where the bounds of the integral are defined by the compact support of the filter kernel. The filtering of the nonlinear terms of the Navier-Stokes equations introduces new unknowns, named subgrid-scale terms, which require modeling. The derivation of physically correct and numerically stable and efficient subgrid-scale models is at the center of the research in LES.

The first LES date back to the 1960's and early 1970's with the pioneering work for incompressible flows of Smagorinsky (1963), Lilly (1967) and Deardorff (1970). Since then, subgrid-scale modeling has matured considerably and can be classified in three general categories: eddy-viscosity models, scale-similarity models, and so-called mixed models which combine eddy-viscosity and scale-similarity expressions (see Lesieur & Métais (1996), Meneveau & Katz (2000), Sagaut (2000), Domaradzki & Adams (2002) for a recent survey of LES).
Eddy-viscosity models rely on the assumption that the subgrid-scale

term is proportional to the strain rate tensor - the proportionality factor being referred to as the eddy-viscosity. The most famous eddy-viscosity model is due to Smagorinsky (1963) and was motivated by meteorological applications. A number of improvements have later been brought to the model with the dynamic eddy-viscosity model of Germano *et al.* (1991) where the initial Smagorinsky constant is estimated dynamically from the local turbulent structures of the flow and with the extension of the model by Yoshizawa (1986) to compressible flows. An alternative to real space eddy-viscosity models has been derived by Chollet (1983) with a spectral eddy-viscosity that is wavenumber-dependent.
Different from eddy-viscosity type models, scale-similarity models are based on the assumption that velocities at different levels give rise to turbulent stresses with similar structures. The subgrid-scale stress tensor can then be computed by substituting unfiltered quantities by an appropriate approximation. Bardina *et al.* (1983) was the first to follow this path with the similarity model where the unfiltered velocities are approximated with their filtered counterparts. Slightly different, the scale-similarity model of Liu *et al.* (1994) and O'Neil & Meneveau (1997) uses a wider filter to compute an approximation to the subgrid-scale stress tensor.
Scale-similarity models have often been observed to suffer from a lack of sufficient subgrid-scale dissipation. A remedy is to combine an eddy-viscosity model which provides additional energy dissipation with a scale-similarity model. This blending of different subgrid-scale terms gives a mixed model. An example is found with the dynamic mixed model of Zang *et al.* (1993) which combines the similarity model of Bardina *et al.* (1983) with the dynamic eddy-viscosity of Germano *et al.* (1991). More recently Sagaut (2000) proposed mixed models with a refined determination of the eddy-viscosity incorporating the kinetic energy of the highest resolved frequencies and selective functions.

In the trail of the mixed models, Stolz & Adams (1999) recently proposed a model based on an approximate defiltering of the filtered variables and a relaxation regularization to account for the energy dissipation. So far this model, ADM, was successfully applied to incompressible turbulent channel flow (Stolz *et al.*, 2001*a*), shock-turbulence interaction on a compression ramp (Stolz *et al.*, 2001*b*), turbulent compressible rectangular jet flow (Rembold *et al.*, 2001), incompressible isotropic turbulence (Müller *et al.*, 2002) and supersonic boundary layer (Stolz & Adams, 2003). These simulations were all performed with high-order

compact finite-difference or spectral schemes implemented in research codes and the extension to numerical schemes more widely used in industrial flow solvers remains to be achieved - it is the topic of this chapter.

This chapter consists of two sections. In the first section, a summary is given in a general form of the main elements of the ADM used for the LES computations. The new extension of ADM to the finite-volume method for implementation in an industrial flow solver is the focus of the second section.

3.1 The approximate deconvolution model

The ADM has been developed by Stolz *et al.* and only a summary of the model is given here. A detailed presentation of ADM can be found in Stolz (2000); Stolz *et al.* (2001*a*,*b*).

In the following we will distinguish between *resolved wave numbers* $|\omega| \leqslant \omega_c$, where ω_c is the filter cutoff wavenumber, *represented wave numbers* $|\omega| \leqslant \omega_n$, which can be represented on the given mesh, and *nonrepresented wave numbers* $|\omega| > \omega_n$, where ω_n is the Nyquist wavenumber. ADM is based on three operations:
(*i*) An explicit filtering of the fluxes.
(*ii*) An approximation of the unfiltered variables which is obtained by defiltering (or deconvolving) the filtered field variables. Given this approximation, the nonlinear terms of the Navier-Stokes equations are computed directly.
(*iii*) The addition of a relaxation term which simulates the effect of scales not represented on the numerical grid by draining energy out of the flow.

3.1.1 Filtering

In most LES methods, the filtering operation (eq. 3.1) is performed implicitly by the projection of the equations onto the computational grid, formally including in the solution all wave numbers up to the Nyquist wavenumber ω_n. Since for finite-difference or finite-volume schemes the wavenumber up to which scales can be considered to be well resolved is often significantly smaller than ω_n, it is desirable to suppress the nonresolved range of the solution by application of an explicit filter operation (Stolz *et al.*, 2000).
With ADM, the explicit primary filtering given in eq. (3.1) is discretized

by a quadrature rule, defined in one space dimension as

$$\overline{f}_i = G_1|_i * f_i := \sum_{j=-\nu_l}^{\nu_r} \alpha_j f_{i+j} \tag{3.2}$$

for the grid function f_i, where $f_i = f(x_i)$. We consider discrete filters on a five-point stencil with $\nu_l + \nu_r = 4$ for interior cells and the filter coefficients α_j are determined by imposing five conditions:

(1) The transfer function is unity at $\omega = 0$ ($\hat{\cdot}$ indicates the Fourier transform of the filter),

$$\hat{G}_1(0) = 1\,. \tag{3.3}$$

(2) The transfer function vanishes at $\omega = \omega_n = \pi$,

$$\hat{G}_1(\pi) = 0\,. \tag{3.4}$$

(3) The first two moments

$$M^k(x) = \int G_1(x - x')(x - x')^k \, dx' \quad k = 1, 2 \tag{3.5}$$

are required to vanish.

(4) To minimize dispersion errors, the imaginary part $\Im(\hat{G}_1)$ of the transfer function should be small,

$$\int_0^\pi \left[\Im(\hat{G}_1)\right]^2 d\omega = \min\,. \tag{3.6}$$

A complete derivation of the coefficients α_j can be found in Stolz *et al.* (2001*a*) and Stolz (2000). The definition of the cutoff wavenumber ω_c is somewhat arbitrary for filters with smooth Fourier transform $\hat{G}(\omega)$. Here the criterion $|\hat{G}_1(\omega_c)| = 1/2$, leading to $\omega_c \approx 2/3\pi$ is used. The transfer function of the primary filter G_1 for an equidistant mesh is shown with the solid line on figure 3.1

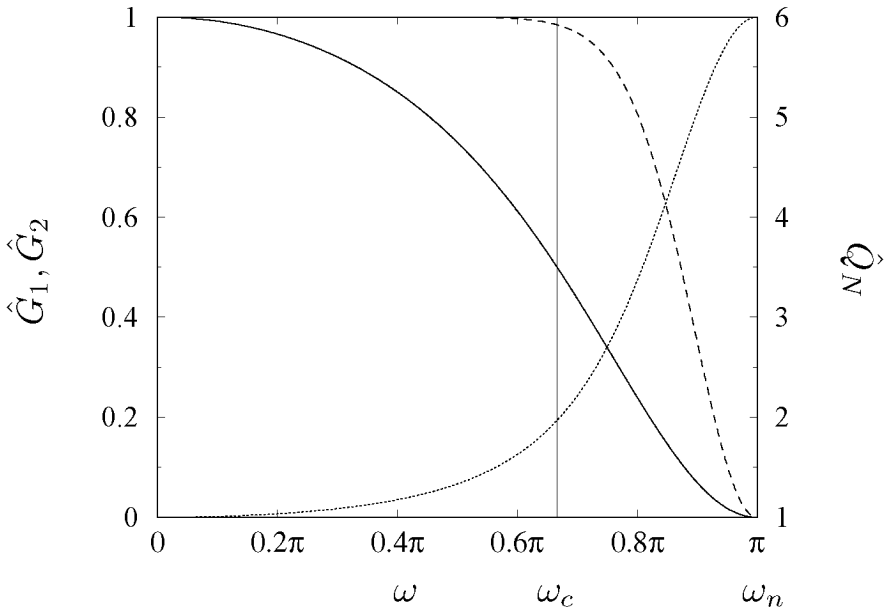

Figure 3.1: Transfer functions, ——— explicit primary filter for an equidistant mesh, ····· approximate inverse $\hat{Q}_N$, - - - - secondary filter $\hat{G}_2 = \hat{Q}_N \cdot \hat{G}_1$, for N=5.

3.1.2 Deconvolution

The represented but nonresolved scales $\omega_c < |\omega| \leqslant \omega_n$ are used to model the effect of the nonrepresented scales $|\omega| > \omega_n$ on the resolved scales $|\omega| \leqslant \omega_c$. Represented scales can be recovered partially by an approximate inversion of the filter (eq. 3.1) resulting in an approximation $f^\star$ of the unfiltered variable f. The approximate deconvolution $f^\star$ is obtained by applying an approximate inverse operator Q_N to $\overline{f}$,

$$f^\star = Q_N * \overline{f}\,. \tag{3.7}$$

The inverse of the filter G_1 can be expanded as an infinite series of filter operators and an approximate inverse operator Q_N is obtained by truncating the series at some N as

$$Q_N = \sum_{\nu=0}^{N} (I - G_1)^\nu \approx G_1^{-1}\,, \tag{3.8}$$

where I is the identity operator. A plot of the transfer function $\hat{Q}_N$ is shown on figure 3.1.

Stolz *et al.* (2001*a*) found that with high-order numerical methods, the deconvolution order $N = 5$ was giving very good results for a wide range of test cases. However, in the frame of the present work where lower-order numerical schemes were used, it was found that adapting the deconvolution order locally to the flow improved significantly the results. Using eq. (3.8), $f^\star$ can be computed by repeated filtering of $\overline{f}$ from

$$\begin{aligned} f^\star = Q_N * \overline{f} &= \overline{f} + (\overline{f} - \overline{\overline{f}}) + (\overline{f} - 2\overline{\overline{f}} + \overline{\overline{\overline{f}}}) + ... \\ &= 3\overline{f} - 3\overline{\overline{f}} + \overline{\overline{\overline{f}}} + ... \ . \end{aligned} \tag{3.9}$$

For the sake of simplicity we now introduce ADM with a generic scalar transport equation for the variable u with the flux $F(u)$,

$$\frac{\partial u}{\partial t} + \frac{\partial F(u)}{\partial x} = 0 \, . \tag{3.10}$$

Applying the filter operator of eq. (3.1) on eq. (3.10) yields:

$$\frac{\partial \overline{u}}{\partial t} + \overline{\frac{\partial F(u)}{\partial x}} = 0 \, . \tag{3.11}$$

Using the approximately deconvolved solution $u^\star = Q_N * \overline{u}$, the filtered flux can be approximated directly by replacing the unfiltered quantity u by $u^\star$ so that the left hand side of eq. (3.11) becomes

$$\frac{\partial \overline{u}}{\partial t} + \overline{\frac{\partial F(u^\star)}{\partial x}} \tag{3.12}$$

thus avoiding at this point the need of computing extra subgrid-scale terms.

3.1.3 Relaxation regularization

The energy transfer to nonrepresented scales $|\omega| > \omega_n$ is modeled only partially by using $u^\star$ in eq. (3.12). Stolz *et al.* (2001*a*,*b*) proposed a relaxation regularization derived from the requirement that the solution remains well-resolved within the range $|\omega| \leqslant \omega_c$. For this purpose, the integral energy of the nonresolved represented scales should not increase, although energy redistribution among these scales is permitted. In order

to model the energy transfer from scales $|\omega| \leqslant \omega_n$ to scales $|\omega| > \omega_n$ energy is drained from the range $\omega_c < |\omega| \leqslant \omega_n$ by subtracting a relaxation term $\chi(I - G_2) * \overline{u}$ from the right-hand side of the filtered differential conservation law (eq. 3.12). χ is a relaxation parameter corresponding to an inverse relaxation-time scale. G_2 is a secondary filter with larger cutoff wavenumber than the primary filter G_1 and is chosen according to Stolz *et al.* as $G_2 = Q_N * G_1$. An example of the transfer function of G_2 for interior points on an equidistant mesh is shown in figure 3.1. Since $(I - \hat{G}_2)$ is positive semidefinite by construction, the relaxation term is purely dissipative as long as χ is positive. Subtracting the relaxation term from the right hand side gives the complete ADM formulation for a scalar transport equation,

$$\frac{\partial \overline{u}}{\partial t} + \overline{\frac{\partial F(u^\star)}{\partial x}} = -\chi(I - G_2) * \overline{u}\,. \tag{3.13}$$

To close the model without requiring an *a priori* parameter choice, Stolz *et al.* estimate χ dynamically from the current solution $\overline{u}$ as a function of space and time. The underlying argument for determining χ is that in order to obtain a well-resolved representation of the filtered solution no energy should accumulate during time advancement in the wavenumber range $\omega_c < |\omega| \leqslant \omega_n$. The kinetic energy content of the considered wavenumber range can be estimated by the second-order structure function (Lesieur & Métais, 1996; Batchelor, 1953) applied to $\phi = (I - G_2) * \overline{u}$. The discrete form of the local second-order structure function in three dimensions, which requires the value of ϕ at the considered grid point in the computational space $\xi = (\xi_1, \xi_2, \xi_3)$ and its six next neighbors in the three computational-space coordinate directions, is given by

$$F_2(\xi, t) = \|\phi(\xi + \mathbf{r}, t) - \phi(\xi, t)\|^2_{\|\mathbf{r}\|=h} \tag{3.14}$$

where h is the computational-space grid spacing. Note again that the mapping of the physical space onto the computational space does not need to be known explicitly.

For an estimate of the relaxation parameter χ, eq. (3.13) is advanced by one Euler-forward time step with size Δt, once using χ=χ_0 and once using χ=0. χ_0 is some positive nonvanishing estimate of the parameter χ, e.g. the value from the previous time integration step or some positive constant of the order of $1/\Delta t$ at time t=0. The difference of the structure function $F_2(\xi, t + \Delta t)|_{\chi=0} - F_2(\xi, t)$ is an estimate for the integral energy generated within the time increment Δt in

the range of scales with wave numbers $\omega_c < |\omega| \leqslant \omega_n$. The difference $F_2(\xi, t+\Delta t)|_{\chi=0} - F_2(\xi, t+\Delta t)|_{\chi=\chi_0}$ estimates how much energy would be dissipated by the relaxation term using $\chi = \chi_0$. Accordingly, χ can be determined from

$$\chi = \chi_0 \frac{F_2(\xi, t+\Delta t)|_{\chi=0} - F_2(\xi, t)}{F_2(\xi, t+\Delta t)|_{\chi=0} - F_2(\xi, t+\Delta t)|_{\chi=\chi_0}} \,. \tag{3.15}$$

By construction, the dynamic parameter χ is now a function of space and time. To avoid the generation of nonresolved scales due to the nonlinear product of χ and $(I - G_2) * \overline{u}$, χ is smoothed with a second-order Padé filter (Lele, 1992) whose cutoff wavenumber ω_c' is set to $\pi/8$. Given a time-step size Δt, an upper and a lower bound $1/100\Delta t \leqslant \chi \leqslant 1/\Delta t$ is imposed for numerical stability at the given time step. If higher values of χ are admitted Δt has to be decreased accordingly.

As a concluding remark, let us mention that the use of the relaxation term can also be interpreted as applying a secondary filter to $\overline{u}$ every $1/\chi$ time steps, which poses the approach in a relation to the truncated Navier-Stokes approach with energy removal of Domaradzki & Radhakrishnan (2002) or the implicit LES approach with periodic filtering of the solution of Visbal *et al.* (2003).

3.2 ADM for the finite-volume method

A first look at finite volumes shows that the method itself involves the application of a top-hat filter when cell-average values are computed and a deconvolution when cell-face values are reconstructed from the cell averages, see e.g. Adams (2001). In addition to this implicit filtering and deconvolution, we will consider here an explicit filtering and deconvolution of the filtered cell-average values instead of the filtered node values of the finite-difference framework.

We write the Navier-Stokes equations as

$$\frac{\partial \mathbf{U}}{\partial t} + \nabla \cdot \mathbb{F}(\mathbf{U}) = 0 \tag{3.16}$$

where $\mathbf{U} = (\rho, \rho u_1, \rho u_2, \rho u_3, E)$ is the state vector and $\mathbb{F}(\mathbf{U}) = (\mathbf{f}_{inv} - \mathbf{f}_v, \mathbf{g}_{inv} - \mathbf{g}_v, \mathbf{h}_{inv} - \mathbf{h}_v)$ the flux tensor. After integrating the equation

above over some volume V and applying the divergence theorem, it can be rewritten as

$$\int_V \frac{\partial \mathbf{U}}{\partial t} d\mathcal{V} + \int_S \mathbb{F}(\mathbf{U})\, \mathbf{n}\, d\mathcal{S} = 0 \;, \tag{3.17}$$

with $\mathbf{n}$ being the outward normal vector at the cell surface S.
The discretization for the i-th cell with volume V_i and cell-average $\mathbf{U}_i = 1/V_i \int_{V_i} \mathbf{U}\, d\mathcal{V}$ is given by (the indices are written for a one-dimensional case for notational simplicity without loss of generality)

$$\frac{\partial \mathbf{U}_i}{\partial t} + \frac{1}{V_i} \sum_{j=1}^{n_{faces}} \mathbf{F}_{ij}(\mathbf{U}) \cdot S_j = 0 \,. \tag{3.18}$$

where $\mathbf{F}_{ij}(\mathbf{U})$ is the discrete flux vector through the j-th cell face of the i-th cell and n_{faces} are the number of faces of the cell (see eq. 2.14).
In the frame of the finite-volume formulation, the cell-average values located in the cell centers constitute the discrete grid function on which the discrete filter (eq. 3.2) is applied. The filtered cell-average value is defined as

$$\begin{aligned} \overline{\mathbf{U}}_i \;\; = \;\; G_1|_i * \mathbf{U}_i := \sum_{k=-\nu_l}^{\nu_r} \alpha_k \mathbf{U}_{i+k} = \\ \sum_{k=-\nu_l}^{\nu_r} \alpha_k \left[\frac{1}{V_{i+k}} \int_{V_{i+k}} \mathbf{U}\, d\mathcal{V} \right] \end{aligned} \tag{3.19}$$

where the volume of the cell, which is a function of space for irregular grids, has to be included in the filter operation. Applying the discrete filter (eq. 3.19) to the discrete transport equation (3.18) yields

$$G_1|_i * \frac{\partial \mathbf{U}_i}{\partial t} + G_1|_i * \left(\frac{1}{V_i} \sum_{j=1}^{n_{faces}} \mathbf{F}_{ij}(\mathbf{U}) \cdot S_j \right) = 0 \,. \tag{3.20}$$

Using the approximately deconvolved solution $\mathbf{U}^\star = Q_N * \overline{\mathbf{U}}$, the filtered flux can be approximated directly by replacing the unfiltered quantity $\mathbf{U}$ by $\mathbf{U}^\star$ so that the left hand side of eq. 3.20 becomes

$$\frac{\partial \overline{\mathbf{U}}_i}{\partial t} + G_1|_i * \left(\frac{1}{V_i} \sum_{j=1}^{n_{faces}} \mathbf{F}_{ij}(\mathbf{U}^\star) \cdot S_j \right) . \tag{3.21}$$

The relaxation term $\chi(I-G_2)*\overline{\mathbf{U}}$ is next subtracted from the right-hand side of the filtered differential conservation law (eq. 3.21). For this vector transport equation, χ is now a vector of three elements $(\chi_\rho, \chi_{\rho\mathbf{u}}, \chi_E)$. The complete ADM formulation for finite volumes finally reads for the continuity, momentum and energy equation

$$\frac{\partial \overline{\rho}_i}{\partial t} + \overline{\frac{1}{V_i}\sum_{j=1}^{n_{faces}} F_{ij}^1(\mathbf{U}^\star)\cdot S_j} = -\chi_\rho (I-G_2)*\overline{\rho}_i\,, \tag{3.22}$$

$$\frac{\partial (\overline{\rho u_1})_i}{\partial t} + \overline{\frac{1}{V_i}\sum_{j=1}^{n_{faces}} F_{ij}^2(\mathbf{U}^\star)\cdot S_j} = -\chi_{\rho\mathbf{u}} (I-G_2)*(\overline{\rho u_1})_i\,, \tag{3.23}$$

$$\frac{\partial (\overline{\rho u_2})_i}{\partial t} + \overline{\frac{1}{V_i}\sum_{j=1}^{n_{faces}} F_{ij}^3(\mathbf{U}^\star)\cdot S_j} = -\chi_{\rho\mathbf{u}} (I-G_2)*(\overline{\rho u_2})_i\,, \tag{3.24}$$

$$\frac{\partial (\overline{\rho u_3})_i}{\partial t} + \overline{\frac{1}{V_i}\sum_{j=1}^{n_{faces}} F_{ij}^4(\mathbf{U}^\star)\cdot S_j} = -\chi_{\rho\mathbf{u}} (I-G_2)*(\overline{\rho u_3})_i\,, \tag{3.25}$$

$$\frac{\partial \overline{E}_i}{\partial t} + \overline{\frac{1}{V_i}\sum_{j=1}^{n_{faces}} F_{ij}^5(\mathbf{U}^\star)\cdot S_j} = -\chi_E (I-G_2)*\overline{E}_i\,, \tag{3.26}$$

with the flux (summation over repeated indices, k, l=1, 2, 3)

$$\mathbf{F}_{ij}(\mathbf{U}^\star) = \begin{pmatrix} (\rho u_k)^\star n_k \\ (\rho u_1)^\star \frac{(\rho u_k)^\star}{\rho^\star} n_k + \check{p}^\star n_1 - \check{\tau}_{1k}^\star n_k \\ (\rho u_2)^\star \frac{(\rho u_k)^\star}{\rho^\star} n_k + \check{p}^\star n_2 - \check{\tau}_{2k}^\star n_k \\ (\rho u_3)^\star \frac{(\rho u_k)^\star}{\rho^\star} n_k + \check{p}^\star n_3 - \check{\tau}_{3k}^\star n_k \\ (E^\star + \check{p}^\star)\frac{(\rho u_k)^\star}{\rho^\star} n_k - \check{\tau}_{kl}^\star \frac{(\rho u_l)^\star}{\rho^\star} n_k - \check{q}_k^\star n_k \end{pmatrix}_{ij} \tag{3.27}$$

where the conservative variables are evaluated at the j-th cell face of the i-th cell. The reconstruction of the cell-face values depends on the numerical discretization and is addressed in the section 2.3.1 and 2.3.2. The notation $\check{\bullet}^\star$ indicates that the quantities are computed from the deconvolved solution, e.g., $\check{p}^\star = (\gamma-1)(E^\star - (\rho u_i)^\star(\rho u_i)^\star/(2\rho^\star))$.

Chapter 4

Wall-bounded flow

Most flows of practical interest are bounded by a solid surface. Examples include internal flows such as the flow through pipes, channels, ducts and tunnels; external flows such as the flow around aircraft, cars, ships or other vehicles; and flows in the environment such as the atmospheric streams on the earth surface or the flow of rivers.

In wall-bounded flows, crucial physical phenomena such as the production and dissipation of turbulent kinetic energy, its distribution, viscous shear stress and the Reynolds-stress anisotropy all reach their peak values within 20 viscous lengthscales from the wall. Depending on the Reynolds number of the flow, this represents approximatively 20% of the channel half-width for a Reynolds number based on the channel half-width and the bulk (averaged over the wall-normal direction) velocity of 3000 but only 0.1% of the channel half-width for a Reynolds number of 10^6 (Pope, 2000). To capture correctly the near-wall physics, Coleman *et al.* (1995) concentrated the 10 first grid points within a distance of 8 viscous lengthscales for their DNS of the compressible channel flow at a Reynolds number of 3000. The Reynolds number of wall-bounded flows of industrial interest is, however, typically a factor 10^3 higher, and requiring the same near-wall resolution as in Coleman's computation would result in a mesh size which is beyond today's computer capacity, or would require a mesh stretching which leads to numerical problems. LES is faced with the same near-wall computational bottleneck since subgrid-scale models require DNS-like resolution in absence of wall-layer models. The latter give however only limited success, in particular for complex flow configurations as recently shown by Piomelli & Balaras (2002).

To alleviate this near-wall resolution problem, engineering applications at high Reynolds number are computed mainly with the RANS equations which solve only the mean flow. The resolution requirement for the mean flow is much lower but the effect of the nonrepresented turbulence has to be modeled. Despite simplifying assumptions, some of these turbulence models (Pope, 2000; Wilcox, 1994) have been able to predict accurately the near-wall mean flow of simple wall-bounded flows. In presence of more complex phenomena like unsteady separation, reat-

tachment, shock flutter or transition, RANS computations fail to obtain satisfactory results and only LES is expected to achieve improvements at an acceptable computational cost. Before coping with these complex flows, it is however necessary to assess the LES subgrid-scale models for simple and well documented flows. It is in this prospect that the compressible turbulent channel flow has been selected as a test case in the present chapter.

The first LES of wall-bounded flow date back to the 1970's when Deardorff (1970) performed with only 6720 grid points the first LES simulation of incompressible channel flow at infinitely large Reynolds number using the Smagorinsky model (Smagorinsky, 1963). Fast growing computer resources allowed Moin & Kim (1982) a few years later to carry out a LES on a grid almost 10 times the size of Deardorff's and at a Reynolds number, based on channel half-width and mean centerline velocity, of Re=13800. Nevertheless, the first DNS computed by Kim *et al.* (1987) was only affordable in the mid-80's and used about four millions grid points to simulate the turbulent incompressible channel flow at a Reynolds number of Re=3253. A similar DNS at slightly higher Reynolds number followed with the simulations of Gilbert & Kleiser (1991). These DNS results provided an unprecedented insight into the details of near-wall flow phenomena and allowed for assessments and improvements of RANS turbulence models and LES subgrid-scale models.

The effect of compressibility on wall-bounded flows has been investigated experimentally by Morkovin (1962) and Bradshaw (1977). They concluded that for a Mach number up to 5 and in the absence of massive heat transfer at the wall, small-scale turbulent fluctuations were little affected by compressibility (often referred to as Morkovin's hypothesis in the literature). Numerical confirmation of this hypothesis came first with the DNS of the supersonic channel flow of Coleman *et al.* (1995), followed by the DNS of supersonic boundary layers of Guarini *et al.* (2000) and Maeder *et al.* (2001). The straightforward use of incompressible LES subgrid-scale models to compressible flows with the so-called variable-density eddy-viscosity extension (Vreman, 1995) thus also found a numerical justification for compressible wall-bounded flows. However, only a few attempts to compute compressible wall-bounded flows by means of LES have been reported in the literature. We cite the LES of a supersonic boundary layer of Normand & Lesieur (1992) and Ducros *et al.* (1995). More recently, Coleman's simulation has been reproduced using LES by Lenormand *et al.* (2000) with several subgrid-scale models

based on mixed-scale assumptions.

Two reasons mainly motivate the choice of the turbulent compressible channel flow for investigation with LES and the ADM in this chapter. First, already mentioned, it allows to evaluate the subgrid-scale model in the challenging near-wall region. Second, both DNS reference data and other LES computations permit to validate the present DNS computation and to compare LES using ADM with other subgrid-scale models.

This chapter is organized as follow: first, the simulation parameters are outlined, followed by an explanation of the forcing term needed to drive the flow in the absence of a pressure gradient. The discussion of the results are made in three parts: first LES with ADM is compared with filtered DNS and no-model or underresolved DNS. For completeness, DNS data obtained with NSMB are also displayed. Second, results with artificial numerical dissipation replacing the relaxation term of ADM are shown. Third, the grid dependence and the influence of the discretization order is investigated.

4.1 The compressible channel flow

4.1.1 Problem formulation

The compressible channel flow at a Reynolds number based on the bulk quantities and channel half-width of Re_b=3000 and a Mach number of M_0=1.5 is considered. This flow configuration permits to compare our DNS results with those of Coleman *et al.* (1995), while our LES results can be compared with the results of Lenormand *et al.* (2000).
The computational domain is spanned by a Cartesian coordinate system, x_1, x_2, x_3 in the streamwise, spanwise and wall-normal direction, respectively. The flow is described by the compressible Navier-Stokes equations for an ideal gas with ratio of specific heats $\gamma = c_p/c_v = 1.4$ and variables are nondimensionalized with the wall temperature T_w^*, the channel half-width H^*, the bulk velocity $u_b^* = \int_V \rho^* u_1^* d\mathcal{V}/(V\rho_b^*)$, and density $\rho_b^* = \int_V \rho^* d\mathcal{V}/V$. The time t is nondimensionalized with H^*/u_b^*. The Reynolds number is defined with the bulk quantities and the channel half-width H^* as $Re_b = \rho_b^* u_b^* H^*/\mu^*(T_w^*)$ and the Mach number is computed according to $M_0 = u_b^*/\sqrt{\gamma R T_w^*}$. The nondimensional dynamic viscosity is calculated as a power law of the nondimensional temperature (Coleman *et al.*, 1995)

$$\mu(T) = T^{0.7}\,. \tag{4.1}$$

	DNS Coleman *et al.* (1995)	DNS NSMB	DNS filtered	ADM	no-model
L_1	4π	4π	4π	4π	4π
L_2	$4\pi/3$	$4\pi/3$	$4\pi/3$	$4\pi/3$	$4\pi/3$
L_3	2	2	2	2	2
N_1	144	288	72	72	72
N_2	80	160	40	40	40
N_3	119	237	60	60	60
M_0	1.5	1.5	-	1.5	1.5
Re_b	3000	3000	-	3000	3000
u_b	1	1	-	1	1
ρ_b	1	1	-	1	1
T_w	1	1	-	1	1

Table 4.1: Parameters of the numerical simulation. Subscript b and w indicate bulk and wall values, respectively.

The channel flow is periodic in the streamwise (x_1) and spanwise (x_2) directions. The wall boundary conditions are no-slip for the velocity and isothermal for the temperature. The grid spacing is constant in the streamwise and spanwise directions and is stretched with a hyperbolic tangent function in the wall-normal direction. Table 4.1 gives an overview of the parameters of the simulation.

Except for the DNS, all simulations were initialized with a laminar velocity profile with a random disturbance superimposed in each of the three coordinate directions. The maximal amplitude of the disturbances was chosen to be 10% of the bulk velocity. The initial density was $\rho(t=0)=1$ and the initial temperature was computed according to the laminar distribution $T(t=0) = 1 + 1/3(\gamma-1)\ Pr\ M_0^2\ u_{1max}\ (1-(x_3-1)^4)$ where u_{1max} is the maximum streamwise laminar velocity which is equal to 1.5. To save computer time, the DNS simulation was started from a turbulent profile obtained from a computation on a $72 \times 40 \times 60$ grid, interpolated onto the fine DNS mesh.

The numerical integration is then carried out with the second-order central scheme of section 2.3.1 and 2.3.2 for the inviscid and viscous fluxes, and the explicit four-stage Runge-Kutta scheme of section 2.5 is used for the temporal integration.

4.1.2 Forcing term

In absence of a streamwise pressure gradient, a forcing term, which unlike the pressure gradient guarantees homogeneity, has to be added to the streamwise momentum and energy equations in order to compensate the wall-friction forces and to maintain a statistically stationary flow. Following Deschamps (1988), the flow is driven in the streamwise direction with a body force $f_1(t)$ adjusted to the instantaneous solution such that the total mass flow rate remains constant, i.e., conserves its initial value.

To obtain the expression of $f_1(t)$, the momentum equation in the streamwise direction is averaged over x_1-x_2 planes and integrated in the wall-normal direction (x_3). Introducing the mass flow rate $Q(t)$ across the transverse plane, one obtains

$$\frac{\partial Q}{\partial t} = \frac{1}{Re_b} L_2 \left[\mu(T) \frac{\partial < \overline{u}_1 >}{\partial x_3} \right]_{x_3=0}^{x_3=2} - L_2 L_3 f_1(t) \,, \tag{4.2}$$

where Q represents the mass flow across a transverse plane and L_2, L_3 are respectively the channel width and height. Using the symmetry of the channel $\partial_{x_3} <\overline{u}_1> |_{x_3=0} = -\partial_{x_3} <\overline{u}_1> |_{x_3=2}$, this expression simplifies to

$$\frac{\partial Q}{\partial t} = -\frac{2}{Re_b} L_2 \mu(T_w) \left. \frac{\partial < \overline{u}_1 >}{\partial x_3} \right|_{x_3=0} - L_2 L_3 f_1(t) \,. \tag{4.3}$$

Physically, this equation shows that if the forcing term remains constant and the flow undergoes transition from laminar to turbulent, the mass flow will decrease as $\partial_{x_3} <\overline{u}_1> |_w$ increases. Note that artificial numerical dissipation or subgrid-scale terms are not taken into account as they vanish at the wall. The mass flow is then kept constant by adjusting at each time step the forcing term such that $\partial_t Q$=0 (eq. 4.3). An extension to compressible flows by Lenormand *et al.* (2000) of the algorithm proposed by Deschamps (1988) is used to update the forcing term at each time step. Assuming that the forcing term f_1^n at time $n\Delta t$ is known, then f_1^{n+1} is computed according to

$$f_1^{n+1} = f_1^n + \frac{\Delta t}{L_2 L_3} [a(Q^{n+1} - Q^0) + b(Q^n - Q^0)] \tag{4.4}$$

where $Q^0 = L_3 L_2 \rho_b u_b$ is the initial mass flow to be conserved, Q^n the mass flow at the time $n\Delta t$ and Q^{n+1} a first-order prediction at time

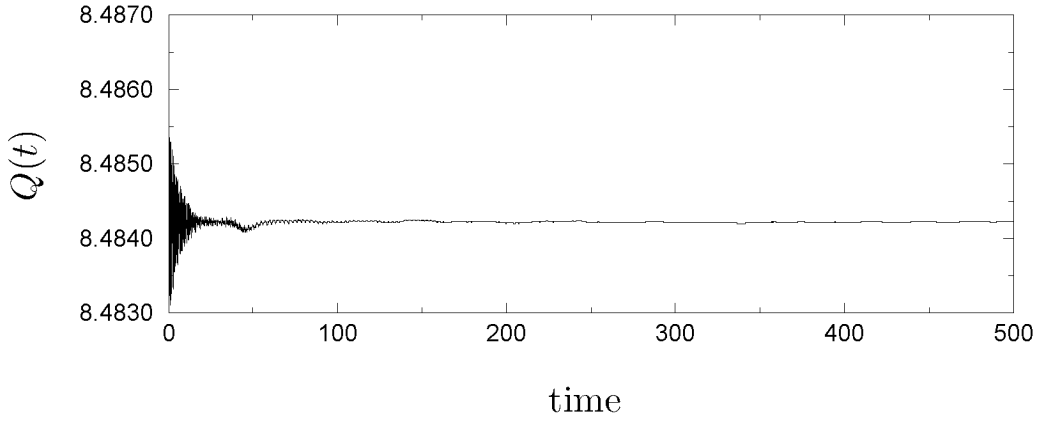

Figure 4.1: Temporal evolution of the mass flow $Q(t)$, (ADM computation).

$(n+1)\Delta t$ given by

$$Q^{n+1} = Q^n - \Delta t \left[L_2 L_3 f_1^n + 2L_2 \frac{\mu(T_w)}{Re_b} \frac{\partial <\overline{u}_1>}{\partial x_3}\bigg|_{x_3=0} \right] . \tag{4.5}$$

The initial value f_1^0 is computed by taking $\partial_t Q$=0 in eq. (4.3), i.e.

$$f_1^0 = -\frac{2\mu(T_w)}{Re_b\, L_3} \frac{\partial <\overline{u}_1>}{\partial x_3}\bigg|_{x_3=0} . \tag{4.6}$$

For incompressible flows, Deschamps has shown using a stability analysis that the algorithm is most efficient if a=$2/\Delta t$ and b=-$0.2/\Delta t$, so that the same coefficients are used here although the flow is compressible.

The temporal evolution of the mass flow $Q(t)$ and the forcing $f_1(t)$ are shown in figures 4.1 and 4.2 respectively. Oscillations coming from the transient regime due to the initial flow field are observed before the flow undergoes transition to a turbulent regime between time $t = 50$ and approximately $t = 120$.

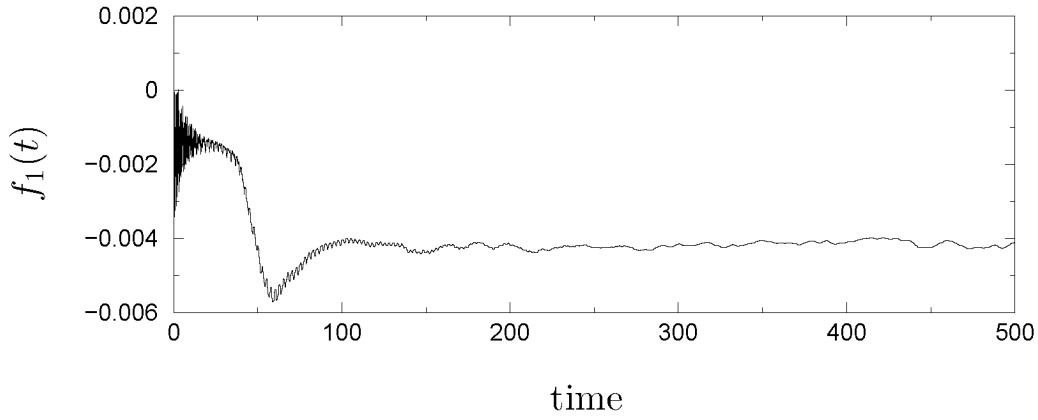

Figure 4.2: Temporal evolution of the forcing $f_1(t)$, (ADM computation).

4.2 Results

First, three different simulations have been performed: a DNS, a no-model computation or underresolved DNS on the same mesh as the LES, and a LES with ADM. For consistency, the LES results are compared with DNS filtered with the filter of ADM and for evaluation of the effect of the model, ADM is also compared with the no-model computation. Next, ADM has been modified in a specific industrial perspective, and simulations with artificial numerical dissipation replacing the relaxation term have been performed. Finally, the results of mesh refinement studies and of computations using a higher-order spatial discretization are presented.

4.2.1 LES with ADM

Starting from the disturbed laminar solution, the computation is advanced for all LES cases for 300 time units $t = t^* u_b^*/H^*$. Transition from laminar to turbulent flow is observed between time $t = 50$ and $t = 120$. The statistics presented here are sampled from time $t = 300$ to $t = 500$ with a sampling interval of 0.1. By inspection of the time evolution of the mass flow or the forcing (figures 4.1 and 4.2), the stationary flow regime is reached at $t = 120$ already, however certain quantities such as the temperature attain a stationary state only rather slowly and

it was thus preferred to wait until $t = 300$ before starting to compute the statistics. For the DNS, the statistics were obtained after an initial transient of 160 time units during an additional 140 time units with a sampling interval of 0.1. The filtered DNS data were computed from 29 DNS samples evenly spaced between time $t = 160$ and $t = 300$. The number of samples was found to be sufficient for the computed statistics to be symmetric across the channel halves. The filtered DNS data are generated by interpolating the DNS onto the LES mesh and subsequent filtering. All statistics presented here are averaged over wall-parallel planes and over both channel halves ($<.>$).

Figure 4.3 gives a qualitative impression of the instantaneous flow close to the wall. Shown are iso-contours of the wall-normal vorticity in a near-wall plane. Clearly visible are the near-wall streak structures. Each simulation represents a different realization of this flow, so that the agreement of these flow snapshots can only be qualitative.

Table 4.2 gives averaged flow quantities measured at the wall and at the channel center. There are slight differences between the DNS of Coleman *et al.* (1995) and our DNS results. In our case the friction-velocity Reynolds number $Re_\tau = Re_b \; u_\tau \rho_w / (u_b \rho_b)$ is smaller and the centerline velocity u_{1c} is larger. Also, a larger centerline temperature T_c and a smaller centerline density ρ_c are observed. These differences may be due to the different numerical method (spectral Fourier-Legendre space differentiation and third-order time integration for Coleman *et al.*), but may also be related to differences in the definition of the forcing $f_1(t)$.

A comparison of ADM results with filtered DNS shows that all quantities of table 4.2 are within a reasonable error margin, e.g., the Reynolds number Re_τ differs by 4.7% from the filtered DNS. The near-wall velocity gradient is slightly overpredicted by the LES, resulting in a larger Reynolds number Re_τ. Due to the interpolation on different grids, the initial mass flow for the DNS and the LES calculations differs by about 0.5%. Since the forcing $f_1(t)$ is adjusted such that the initial mass flow is kept constant throughout the simulation, the centerline velocity u_{1c} of ADM and of the filtered DNS can be equal despite the steeper near-wall velocity gradient of ADM.
As shown in figures 4.4 and 4.5, the mean velocity, density and temperature profiles of the LES calculation are in good agreement with the filtered DNS results. For the velocity profile, a steeper slope near the wall can be seen which is responsible for the larger Reynolds number Re_τ with ADM. A similar overprediction of u_τ accounts for the differ-

(a)

(b)

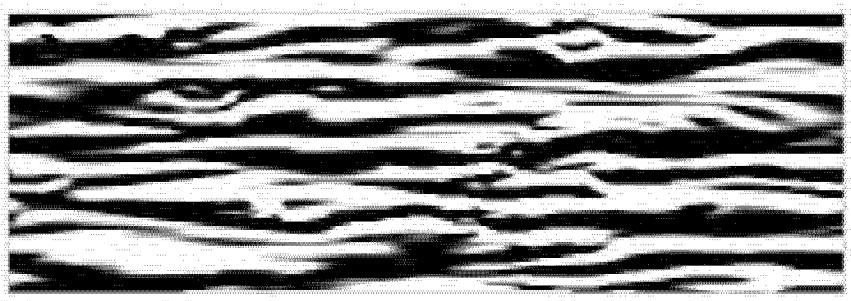

(c)

Figure 4.3: Contours of instantaneous wall-normal vorticity ω_3 in (x_1, x_2)-plane at $x_3^+ \approx 10$, (a) ADM, (b) no-model (nonfiltered), (c) DNS; $\omega_3 \geqslant 0$ in light regions, $\omega_3 < 0$ in dark regions.

ence of the mean streamwise velocity profile in wall units between ADM and filtered DNS in the outer layer as can be seen from the van-Driest-transformed profile $<\overline{u}_{1VD}>^+$ (figure 4.5 (b)) which is computed as

$$<\overline{u}_{1VD}>^+ = \int_0^{<\overline{u}_1>^+} \sqrt{\frac{\overline{\rho}}{\overline{\rho}_w}}\, d<\overline{u}_1>^+ \quad . \tag{4.7}$$

The von Karman constant is, however, predicted accurately.
For the velocity fluctuations $u_i' = u_i - <u_i>$ and Reynolds-stress (fig-

	DNS Coleman *et al.* (1995)	DNS NSMB	DNS filtered	ADM	no-model (nonfiltered)
Re_τ	222	216	214	224	217
τ_w	12.12	11.41	11.35	12.44	11.61
u_τ	0.0545	0.0529	0.0530	0.0554	0.0534
$\Delta^+_{x_1}$	19	9.4	37	39	38
$\Delta^+_{x_2}$	12	5.6	22	23	23
$\Delta^+_{x_3}\|w$	0.1	0.38	1	1	1
u_{1c}	1.16	1.18	1.18	1.18	1.19
T_c	1.378	1.39	1.39	1.40	1.41
ρ_c	0.980	0.977	0.977	0.979	0.977
ρ_w	1.355	1.359	1.359	1.353	1.360

Table 4.2: Mean flow variables. Subscript c and w indicate center and wall values, respectively.

ures 4.6 and 4.7) trends are somewhat more difficult to determine. Amplitude errors reach a maximum of 6% for the wall-normal fluctuations (figure 4.7 (a)) and spatial shifts of the fluctuation peaks are also visible (figure 4.6 (b)).

Results (nonfiltered) from the no-model computation compare surprisingly well with the DNS. Except for the mean temperature, which is overpredicted, the mean profiles show all very good agreement with the DNS. The mean velocity profile of the no-model computation plotted in wall units (figure 4.5 (b)) demonstrates even a perfect overlapping with the DNS. This good behavior can be attributed to the scaling with the wall quantities (table 4.2), for which differences with the DNS values are minimal. For the turbulent fluctuations also (figures 4.6 and 4.7), the agreement with the DNS is on average as good as the one observed between ADM and filtered DNS. In terms of computational cost finally, the no-model computations ran approximatively 1/3 faster than the ADM calculations which needed about 2% of the computational time of the DNS.

The inspection of the energy spectra puts however the success of the no-model computation slightly into perspective. The one-dimensional Fourier spectra in the wall-parallel directions are integrated in the transverse and the wall-normal direction as

$$E_1(k_1) = \int_0^{2H} |\hat{u}_i(k_1, 0, x_3)|^2 dx_3/2H\,, \qquad i = 1, 2, 3 \tag{4.8}$$

for the spectra in the streamwise direction x_1 and

$$E_2(k_2) = \int_0^{2H} |\hat{u}_i(0, k_2, x_3)|^2 dx_3/2H\,, \qquad i = 1, 2, 3 \tag{4.9}$$

for the spectra in the spanwise direction x_2, where k_1 and k_2 are the wavenumbers in streamwise and spanwise directions.
Comparisons of ADM and filtered DNS spectra in streamwise and spanwise directions for the three velocity components are shown in figures 4.8, 4.9 and 4.10. The large scales of the ADM computations show a good agreement with the filtered DNS whereas some discrepancies are observed in the smaller, nonresolved scales.
The spectra of the no-model computation are next compared with the spectra of the DNS truncated to the coarse grid resolution. Similarly to ADM, the large scales of the no-model compare very well with the DNS. For the small scales, no clear trend can be deduced as the energy level of the no-model is either underpredicted (figures 4.8 (a), 4.9 (a) and 4.10 (a)), in good agreement (figures 4.8 (b) and 4.10 (b)), or even overpredicted (figure 4.9 (b)). As a central scheme is used, no dissipation is formally present in the discretization and the energy decay at the high-wavenumber end of the spectrum has to be attributed to the skew-symmetric formulation of the convective terms which combines a conservative and nonconservative flux formulation. Blaisdell *et al.* (1996) noticed that the aliasing errors of the conservative and nonconservative flux terms interact in a positive manner by preventing an unphysical energy pile-up in the high-wavenumber range of the spectra. This characteristic of the skew-symmetric form may be responsible here for some deficiencies in the high-wavenumber range of the spectra (apparent dissipation in the streamwise spectra) but explains also why the no-model computation remained stable without any artificial dissipation terms. The fact that no-model computations with the flux terms discretized in conservative form only became unstable, brings a further confirmation to the above assertions. Of interest is that in this case the relaxation term of ADM was able to provide enough dissipation to stabilize the computation, the results remained however slightly less accurate than with the skew-symmetric form.

Different from the good no-model results obtained here, Stolz *et al.* (2001*a*) observed a visible deterioration of the turbulence statistics for no-model coarse-grid computations of the turbulent incompressible channel flow computed with a spectral method. For this reason, we believe

that the main source of error in the ADM simulations with the present primary-filter choice does not come from the subgrid-scale model but rather from the numerical discretization. Similar observations were made by Mossi (1999) and Garnier *et al.* (1999) who also found that the effect of different subgrid-scale models employed with the present numerical method was rather small. Filtering of the no-model computation would probably give results very close to ADM which suggests a small influence of the model in this particular case. Considering, however, the already good quality of the no-model computation, the ADM results can be seen positively compared to other subgrid-scale models which proved even to deteriorate results (Mossi, 1999). No-model computations of more complex flows such as shock-turbulence interaction were found to be unstable. In this case the regularizing effect of the skew-symmetric form is insufficient and an explicit relaxation term has to be used.

Figure 4.11 shows the time- and plane-average, and root-mean square (rms) fluctuations of the relaxation parameter χ. The same deconvolution order $N = 5$ (see eq. 3.8) as used by Stolz *et al.* (2001*a*) for the incompressible turbulent channel flow was chosen here. The average distribution is almost constant across the channel height and the largest relaxation parameter value is obtained for the momentum equation indicating that the energy removal frequency is the highest there. The rms fluctuations all show a peak near the wall and a constant level across the channel height. Unlike the time- and plane-average profiles, the largest values are obtained for the continuity equation. It is also observed that none of the profiles exhibits perfect symmetry over the channel half-width (neither anti-symmetry despite the appearance). This is due to the relaxation parameter procedure which is very sensitive to the smallest variations of ρ, $\rho\mathbf{u}$ and E, respectively.

Some comparisons with the simulations of Lenormand *et al.* (2000) who recently evaluated several subgrid-scale models for the same channel flow configuration may be of interest to conclude this section. Similar to the present computations, the convective terms were discretized in skew-symmetric form with a fourth-order finite-difference scheme whereas the diffusive terms were discretized with a second-order scheme. Six different subgrid-scale models were tested on a coarse and a fine mesh (only these latter results will be considered here). Different from our computations, the streamwise extent of the computational domain was only 2π. The number of grid points in the wall-normal direction was two times larger (N_3=119) than in our case and the spanwise number of grid points was

3/2 times larger. Two of the tested subgrid-scale models were based on the Smagorinsky model, whereas the four others were based on a newly proposed mixed-scale model, which estimates the subgrid-scale kinetic energy by means of a test filter and scale-similarity arguments. Linear hybridization with a Bardina-type model (Bardina *et al.*, 1980, 1983) was also considered, together with the use of a turbulent scale selection function. *A priori* tests suggested the use of the hybrid models, and a comparison of these models with the DNS data (nonfiltered) of Coleman *et al.* (1995), showed results of similar quality as ours. The mean quantities were predicted accurately except for the temperature where, as in our case, the LES slightly overpredicted the temperature in the channel center. Clear trends for the velocity fluctuations and the Reynolds-stress were also difficult to determine, but differences in the peak magnitude and location were visible.

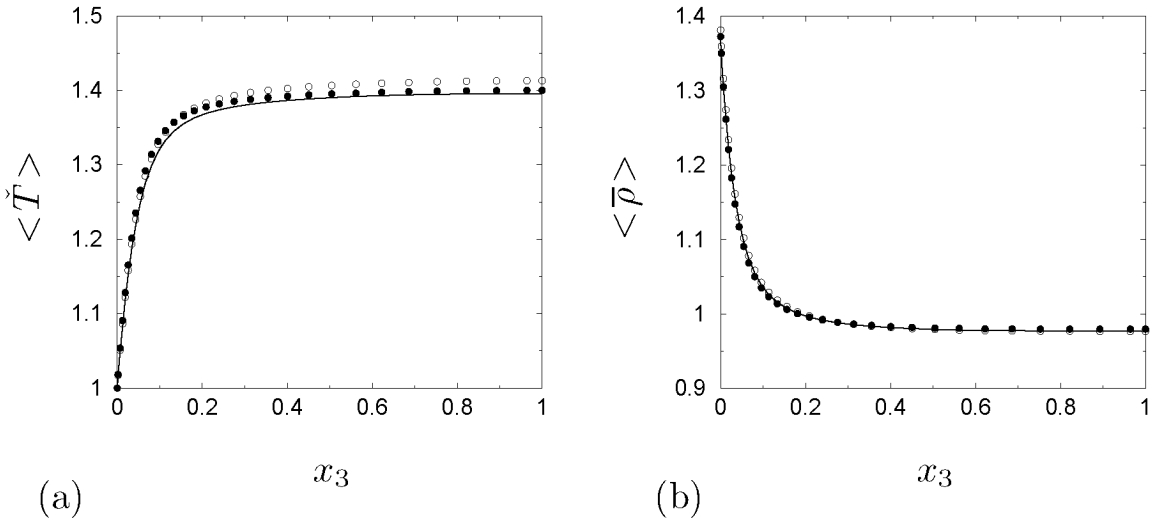

Figure 4.4: (a) Mean temperature profile, (b) Mean density profile; ——— *DNS,* • *ADM,* ——— *filtered DNS,* ∘ *no-model (nonfiltered).* $\check{\bullet}$ *indicates that the quantity is computed from the filtered solution. Note that the filtered DNS collapses with the DNS.*

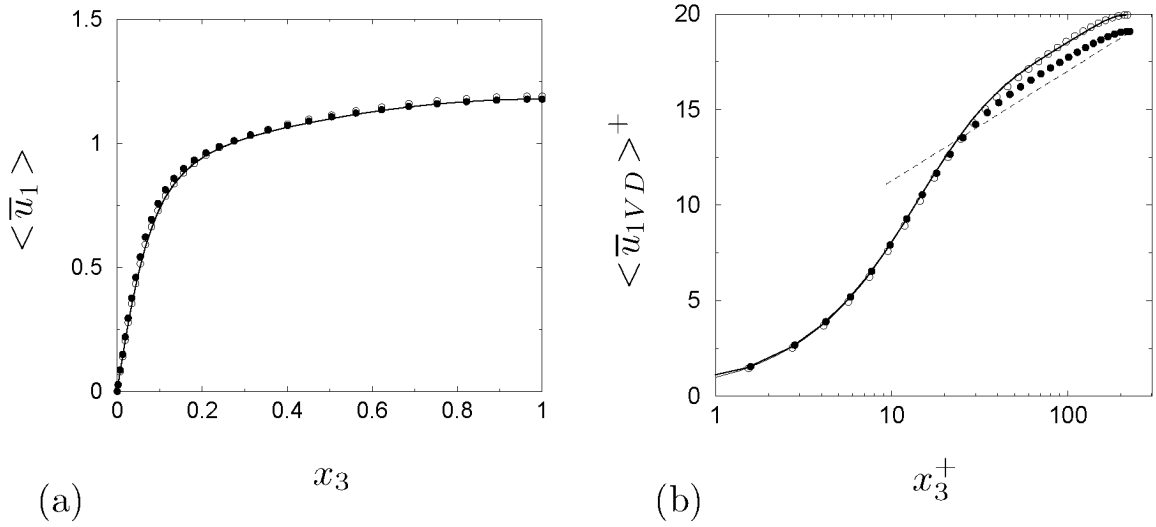

Figure 4.5: Mean velocity profile, (a) linear plot, (b) van-Driest-transformed logarithmic plot; ——— *DNS,* • *ADM,* ——— *filtered DNS,* ∘ *no-model (nonfiltered),* - - - - $2.5\ ln\ x_3^+ + 5.5$.

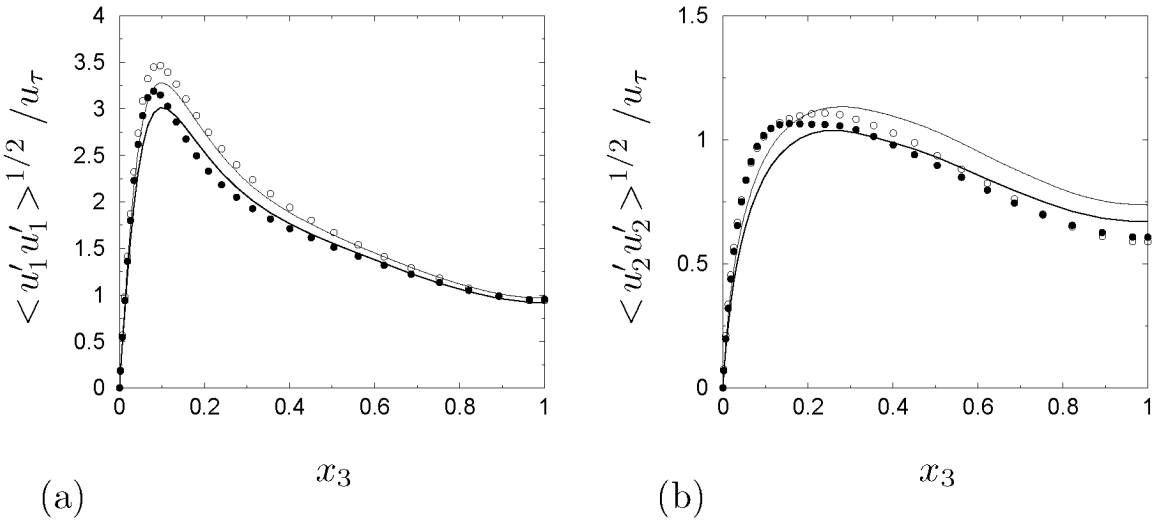

Figure 4.6: Velocity fluctuations, (a) streamwise velocity, (b) spanwise velocity; ——— *DNS,* • *ADM,* ——— *filtered DNS,* ∘ *no-model (nonfiltered).*

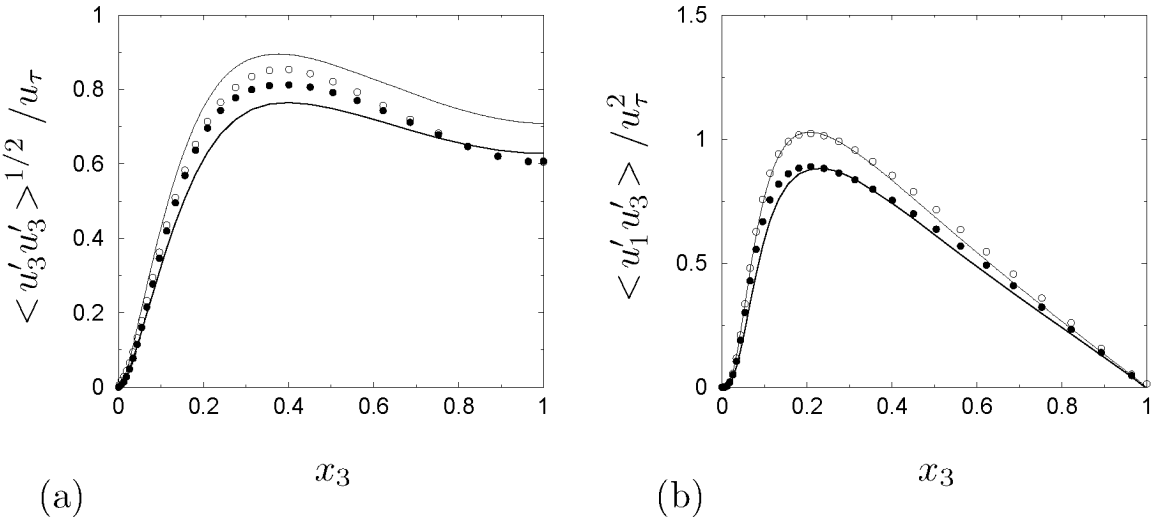

Figure 4.7: (a) Velocity fluctuations in wall-normal direction, (b) Reynolds-stress; ——— *DNS,* • *ADM,* ——— *filtered DNS,* ∘ *no-model (nonfiltered).*

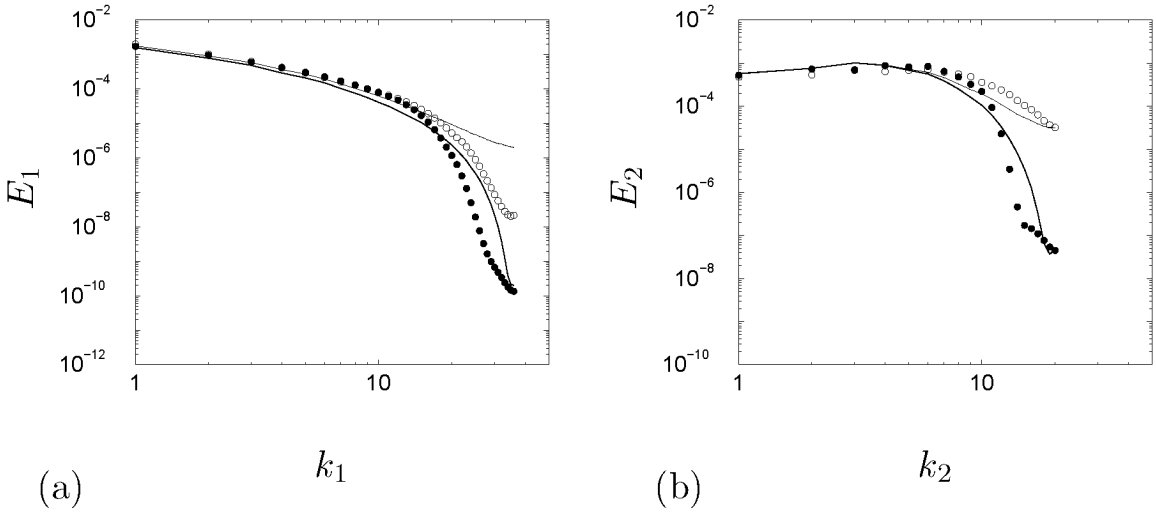

Figure 4.8: One-dimensional energy spectra for the streamwise velocity u_1; ——— DNS (truncated), • ADM, ——— filtered DNS, ∘ no-model (nonfiltered). (a) streamwise direction, (b) spanwise direction.

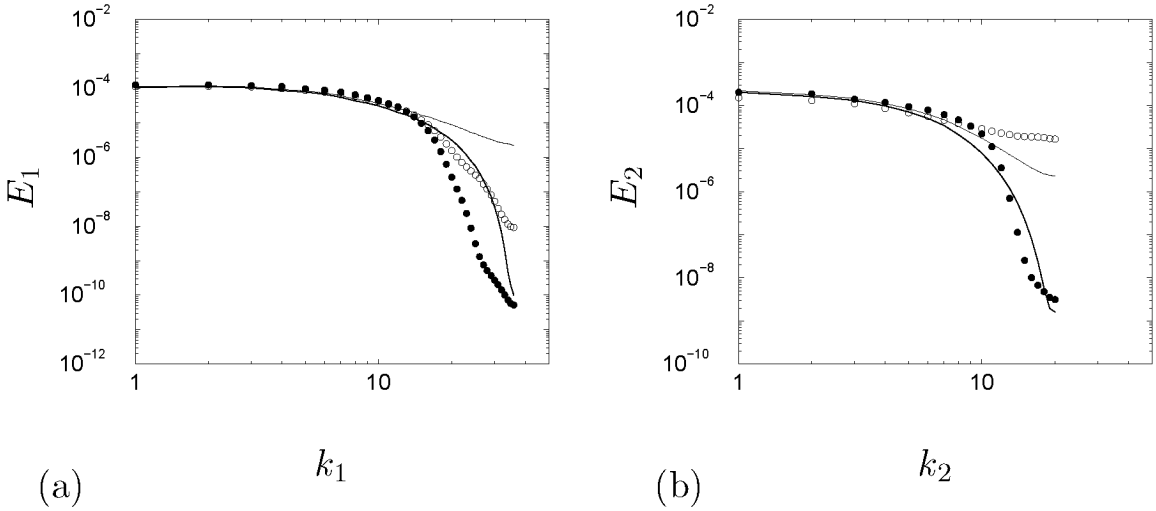

Figure 4.9: One-dimensional energy spectra for the spanwise velocity u_2; ——— DNS (truncated), • ADM, ——— filtered DNS, ∘ no-model (nonfiltered). (a) streamwise direction, (b) spanwise direction.

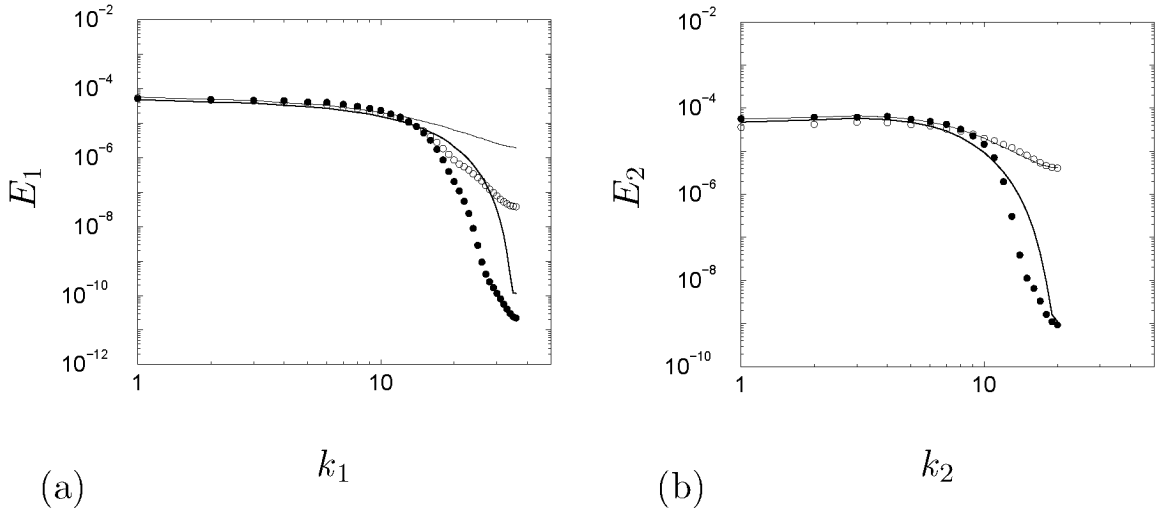

Figure 4.10: One-dimensional energy spectra for the wall-normal velocity u_3; ——— DNS (truncated), • ADM, ——— filtered DNS, ○ no-model (nonfiltered). (a) streamwise direction, (b) spanwise direction.

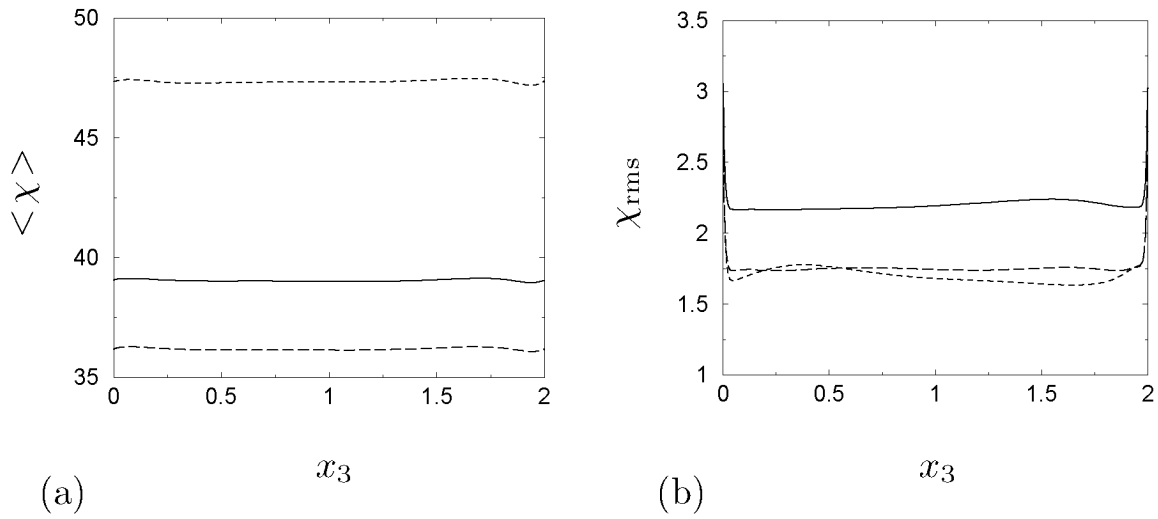

Figure 4.11: ——— χ_ρ, ····· $\chi_{\rho\mathbf{u}}$, - - - - χ_E; (a) time- and plane-average, (b) root-mean square.

4.2.2 Mixed model with deconvolution and artificial numerical dissipation

In this section, we investigate whether ADM can be simplified by using an artificial numerical dissipation term as introduced by Jameson and later extended by Swanson & Turkel (1987) to replace the relaxation term originally present in ADM. The benefit of this modification is a simpler implementation of ADM in industrial flow solvers using the finite-volume method and employing this kind of numerical dissipation. The flow and mesh parameters are identical to the previous ADM computation and are summarized in table 4.1.

The artificial numerical dissipation terms (see section 2.4) are calculated from deconvolved variables and filtered afterwards. Replacing the relaxation term of eq. (3.22)-(3.26) by an artificial numerical dissipation term, we obtain

$$\frac{\partial \overline{\rho}_i}{\partial t} + \overline{\frac{1}{V_i} \sum_{j=1}^{n_{faces}} F_{ij}^1(\mathbf{U}^\star) \cdot S_j} = \overline{\frac{1}{V_i} D_i^1(\rho^\star)}\,, \tag{4.10}$$

$$\frac{\partial (\overline{\rho u_1})_i}{\partial t} + \overline{\frac{1}{V_i} \sum_{j=1}^{n_{faces}} F_{ij}^2(\mathbf{U}^\star) \cdot S_j} = -f_1 + \overline{\frac{1}{V_i} D_i^2((\rho u_1)^\star)}\,, \tag{4.11}$$

$$\frac{\partial (\overline{\rho u_2})_i}{\partial t} + \overline{\frac{1}{V_i} \sum_{j=1}^{n_{faces}} F_{ij}^3(\mathbf{U}^\star) \cdot S_j} = \overline{\frac{1}{V_i} D_i^3((\rho u_2)^\star)}\,, \tag{4.12}$$

$$\frac{\partial (\overline{\rho u_3})_i}{\partial t} + \overline{\frac{1}{V_i} \sum_{j=1}^{n_{faces}} F_{ij}^4(\mathbf{U}^\star) \cdot S_j} = \overline{\frac{1}{V_i} D_i^4((\rho u_3)^\star)}\,, \tag{4.13}$$

$$\frac{\partial \overline{E}_i}{\partial t} + \overline{\frac{1}{V_i} \sum_{j=1}^{n_{faces}} F_{ij}^5(\mathbf{U}^\star) \cdot S_j} = -f_1 \overline{u}_1 + \overline{\frac{1}{V_i} D_i^5(E^\star)}\,, \tag{4.14}$$

where D_i^k is the k-th element of the vector of artificial numerical dissipation for the i-th cell and $f_1(t)$ the forcing term described in section 4.1.2. This model is from now on referred to as ADM-dissip.

The ADM-dissip simulations are initiated with a turbulent flow solution obtained from the no-model computation of the previous section. After a transient period of 200 time units, the statistics are computed during an additional period of 200 time units with a sampling interval

	DNS filtered	ADM	ADM-dissip1	ADM-dissip2
$k^{(2)}, k^{(4)}$	-	-	0.5, 0.01	2.0, 0.05
Re_τ	214	224	210	178
τ_w	11.35	12.44	10.89	7.94
u_τ	0.0530	0.0554	0.0517	0.0439
Δ_1^+	37	39	36.7	31.2
Δ_2^+	22	23	22.0	18.7
$\Delta_3^+\|_w$	1	1	0.95	0.8
u_{1c}	1.178	1.176	1.195	1.229
T_c	1.396	1.394	1.408	1.411
ρ_c	0.977	0.979	0.976	0.969
ρ_w	1.346	1.353	1.356	1.355

Table 4.3: Mean flow variables of different simulations, including use of artificial numerical dissipation terms. Subscript c and w indicate center and wall values, respectively.

of 0.1. To determine the best choice of the values of the parameters $k^{(2)}$ and $k^{(4)}$ would require many computations and is not the priority of the present investigation. The point is to clarify whether some typical parameter set gives acceptable results, and therefore both extrema of the commonly used range for the dissipation coefficient $k^{(2)}$ and $k^{(4)}$ have been tested, i.e. $k^{(2)}$=0.5, $k^{(4)}$=0.01 (ADM-dissip1) and $k^{(2)}$=2.0, $k^{(4)}$=0.05 (ADM-dissip2).

Table 4.3 shows the value of averaged quantities at the wall and at the center of the channel. Considering first the ADM-dissip2 results, we observe that the value of Re_τ is significantly underpredicted, indicating a too large dissipation. Similarly, the centerline velocity u_{1c} is overpredicted. The overprediction of the centerline temperature T_c is larger than in the ADM computation of the previous section and consequently the centerline density ρ_c is smaller. The graphs of the mean temperature, density and velocity (figures 4.12 and 4.13 (a)) clearly show the overdissipative behavior of the numerical dissipation, particularly in the near-wall region. The van Driest velocity profile (figure 4.13 (b)) shows a significant deviation from the filtered DNS data in the core of the channel which is due to the cumulated effect of the overpredicted centerline velocity and the underpredicted friction velocity u_τ.
Turbulent fluctuations are also represented poorly as can be seen in figure 4.14 (a). In particular, the spanwise and wall-normal velocity

fluctuations are highly damped whereas the streamwise fluctuations are overpredicted due to the friction velocity normalization. Finally, the peak location of the Reynolds-stress is not predicted accurately as can be observed in figure 4.14 (b). Reducing $k^{(2)}$ and $k^{(4)}$ to 0.5 and 0.01 (ADM-dissip1) dramatically improves the results. Wall and centerline mean quantities are within the same error margin as the ADM results, as can be read from table 4.3. The mean velocity and density profiles of the ADM agree slightly better with the filtered DNS than the ADM-dissip1 simulation (figures 4.12 and 4.13) but turbulent quantities are better predicted by the latter in the near wall region (figure 4.14). However, reducing the amount of dissipation further leads to unstable simulations.

Despite the strong dependence of the results on the values of the dissipation coefficients, we have shown that for certain values of $k^{(2)}$ and $k^{(4)}$, the simplified method is able to compete with the relaxation term of ADM, but results deteriorate quickly for inappropriate values of these coefficients (excessive dissipation for large values, unstable simulations for too small values). The best choice of the values of the dissipation coefficients is grid and flow dependent and can only be found by trial and experience. The computational time of both variants is very much the same. However, the successive computations necessary to find optimal dissipation coefficients are much more time consuming than a single ADM computation.

4.2.3 Numerical tests

Computations with the convective terms discretized with a fourth-order skew-symmetric scheme (see section 2.3.1) were also performed. The mesh, the flow and the other numerical parameters are identical to the previous ADM computations.
For the mean profiles of figures 4.15 and 4.16, no significant difference can be seen between the fourth-order and the second-order discretization.
For the fluctuating quantities of figure 4.17, no improvement of the results can be observed compared to the results obtained with the second-order scheme. Surprisingly, no improvement of the friction-velocity Reynolds number Re_τ is observed with the discretization order as Re_τ rises to 229 for the fourth-order scheme (Re_τ=214 for the filtered DNS and 224 for ADM with the second-order scheme).

Mesh dependence was investigated by refining the computational

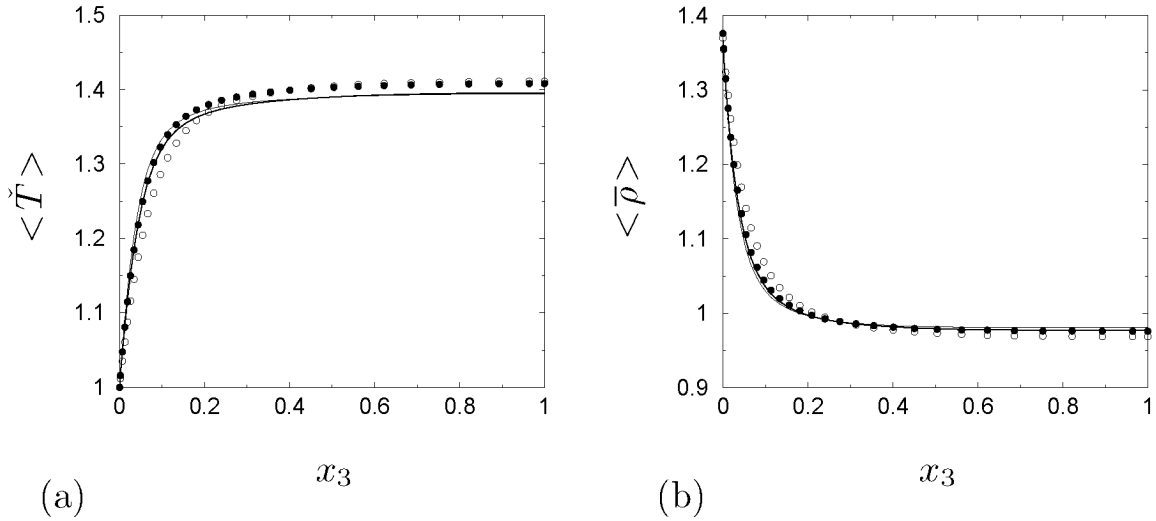

Figure 4.12: (a) Mean temperature profile, (b) Mean density profile; • *ADM-dissip1,* ——— *filtered DNS,* ○ *ADM-dissip2,* ——— *ADM.* ˇ *indicates that the quantity is computed from the filtered solution.*

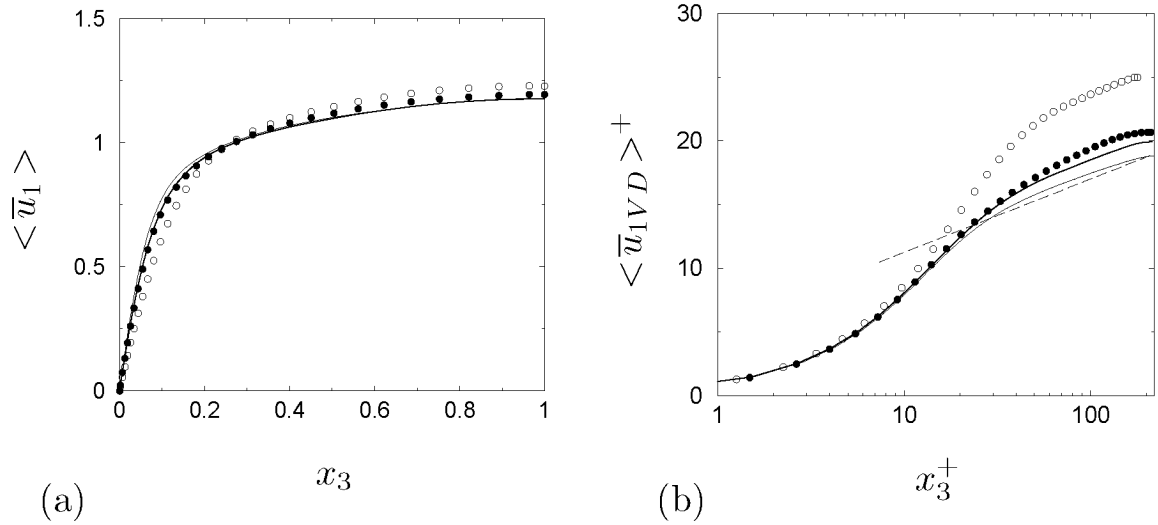

Figure 4.13: Mean velocity profile, (a) linear plot, (b) van-Driest-transformed logarithmic plot; • *ADM-dissip1,* ——— *filtered DNS,* ○ *ADM-dissip2,* ——— *ADM,* - - - - *2.5 ln* x_3^+ *+ 5.5.*

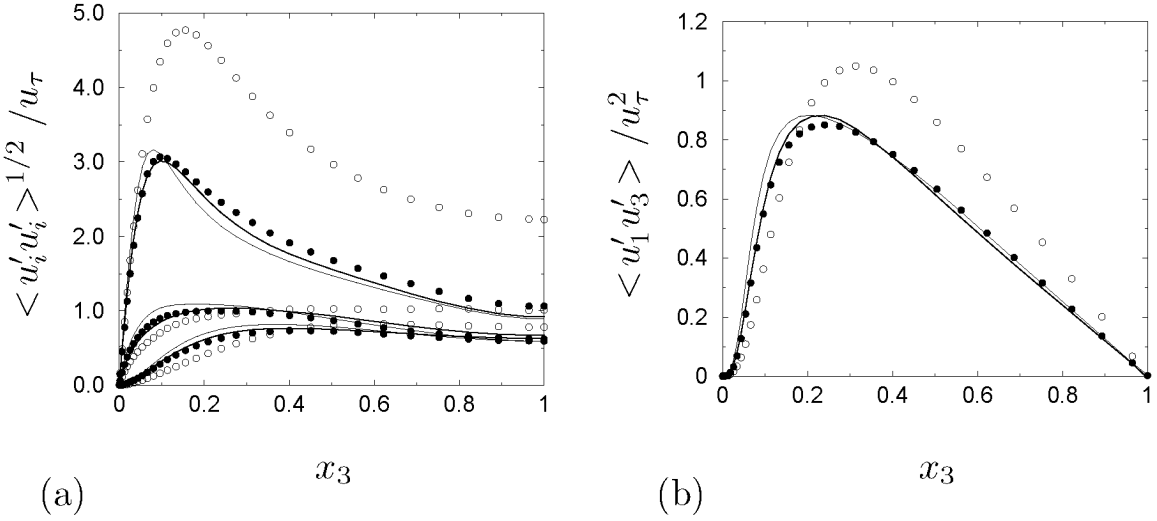

Figure 4.14: (a) Velocity fluctuations, from top down, streamwise, spanwise and wall-normal, (b) Reynolds-stress; • ADM-dissip1, ——— filtered DNS, ○ ADM-dissip2, ——— ADM.

mesh to N_1=144, N_2=80, and N_3=120 cells (1/2 in each direction of the number of grid points of the NSMB DNS). All other flow and numerical parameters are identical to the previous ADM simulations.
For the mean profiles (figures 4.18 and 4.19), the agreement between filtered DNS and LES is excellent, in particular the prediction of the temperature is improved. With a lower value for Re_τ of 220 (Re_τ=214 for the filtered DNS), the velocity gradient at the wall compares better with the filtered DNS on the fine mesh. All the other wall quantities follow the same trend as Re_τ. The velocity fluctuations are also slightly better predicted (figure 4.20 (a)) on the fine mesh. The agreement of the Reynolds-stress (figure 4.20 (b)) does not improve on the fine mesh and is comparable with the results obtained on the coarser mesh.
Comparing the effect of the discretization order and mesh size, we can conclude that results are more sensitive to mesh refinement than to the discretization order.

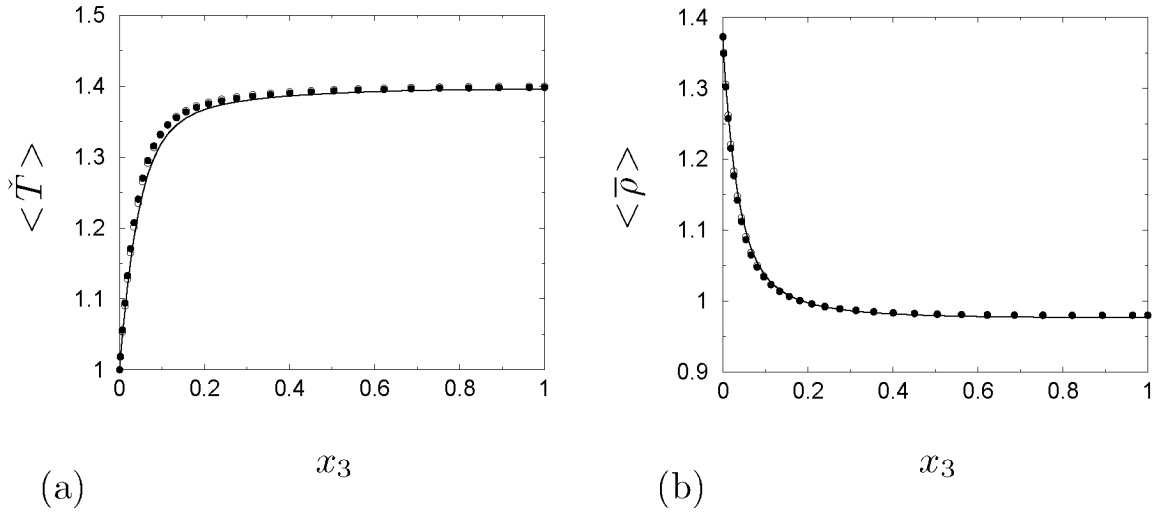

Figure 4.15: (a) Mean temperature profile, (b) Mean density profile; • ADM with a fourth-order scheme, ——— filtered DNS, ○ ADM with a second-order scheme. ˇ indicates that the quantity is computed from the filtered solution.

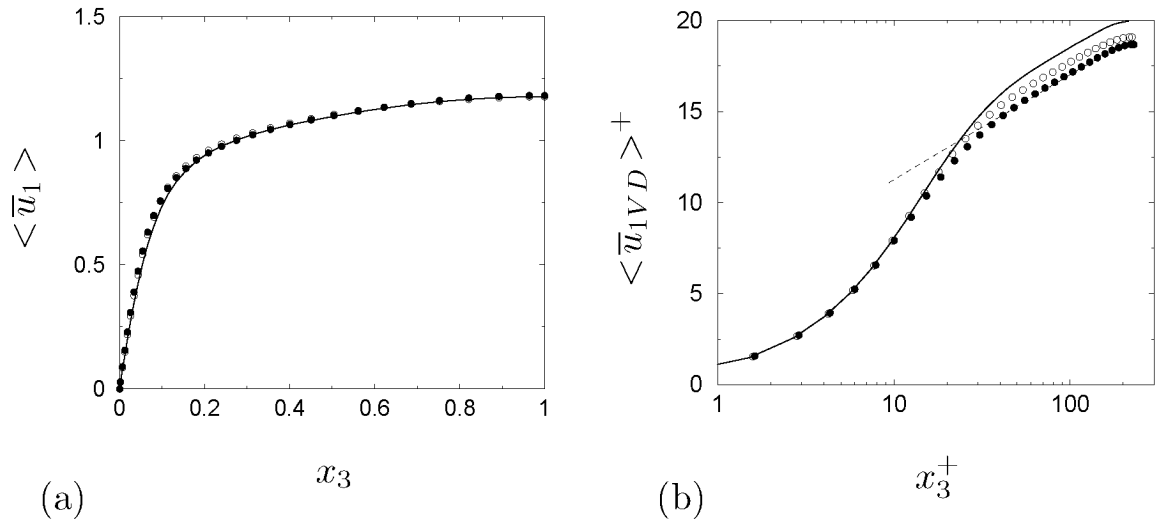

Figure 4.16: Mean velocity profile, (a) linear plot, (b) van Driest transformed logarithmic plot; • ADM with a fourth-order scheme, ——— filtered DNS, ○ ADM with a second-order scheme, - - - - 2.5 ln x_3^+ + 5.5.

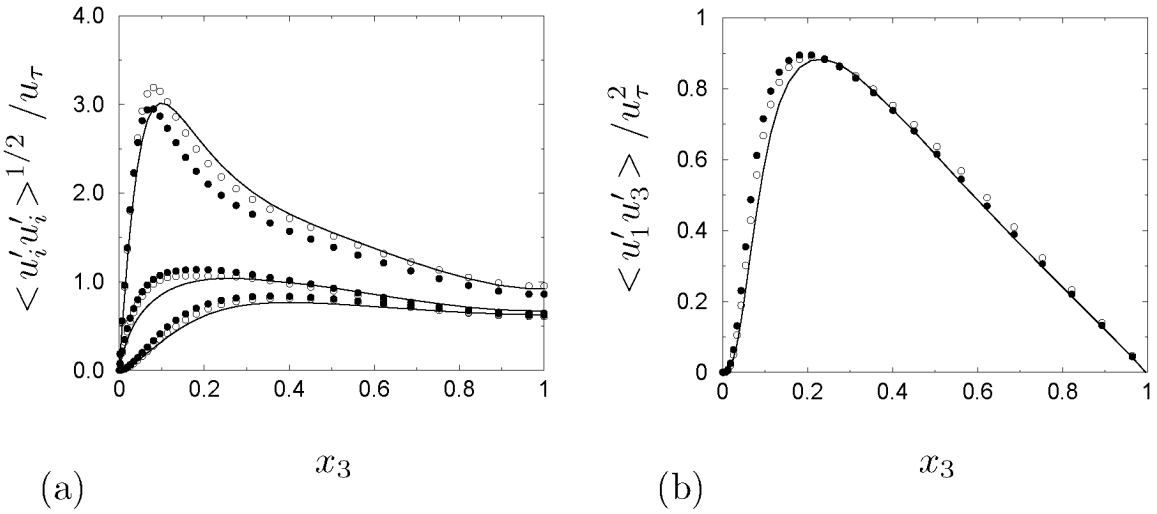

Figure 4.17: (a) Velocity fluctuations, from top down, streamwise, spanwise and wall-normal, (b) Reynolds-stress; • ADM with a fourth-order scheme, ——— filtered DNS, ○ ADM with a second-order scheme.

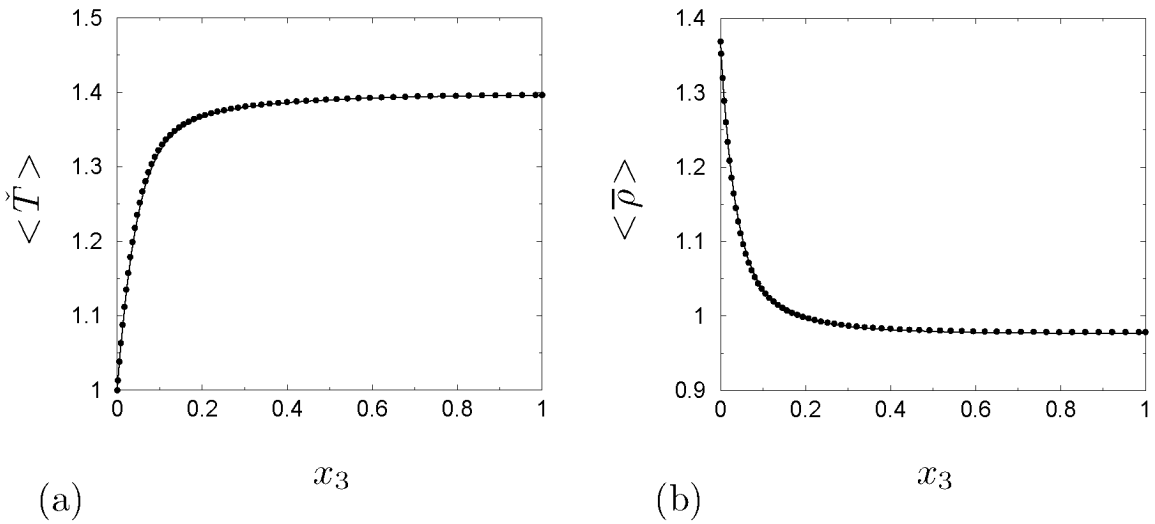

Figure 4.18: Results on a refined mesh with N_1=144, N_2=80, and N_3=120. (a) Mean temperature profile, (b) Mean density profile; • ADM, ——— filtered DNS. ˇ indicates that the quantity is computed from the filtered solution.

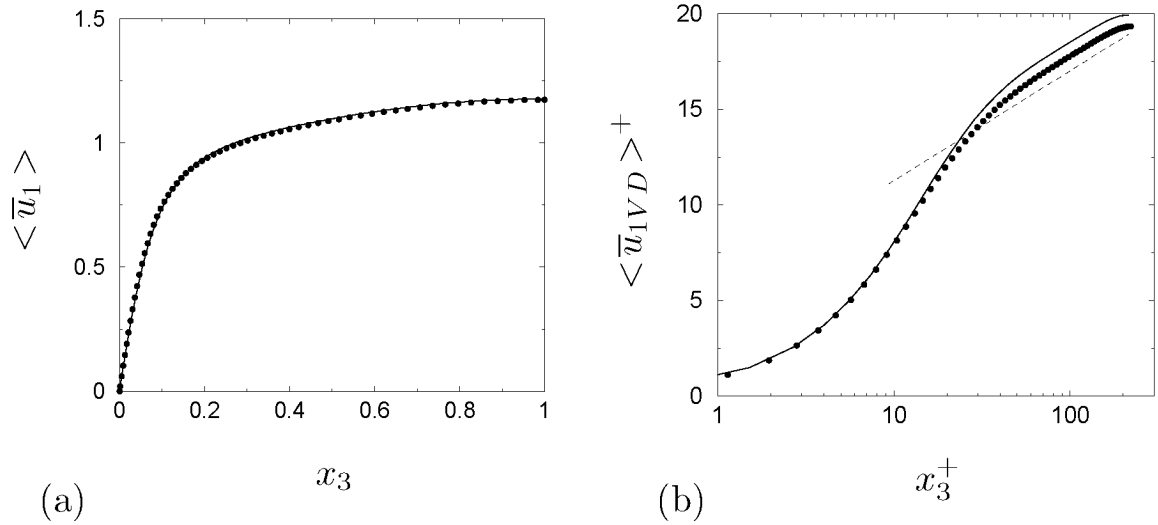

Figure 4.19: Results on a refined mesh with N_1=144, N_2=80, and N_3=120. Mean velocity profile, (a) linear plot, (b) van Driest transformed logarithmic plot; • ADM, ——— filtered DNS, - - - - 2.5 ln x_3^+ + 5.5.

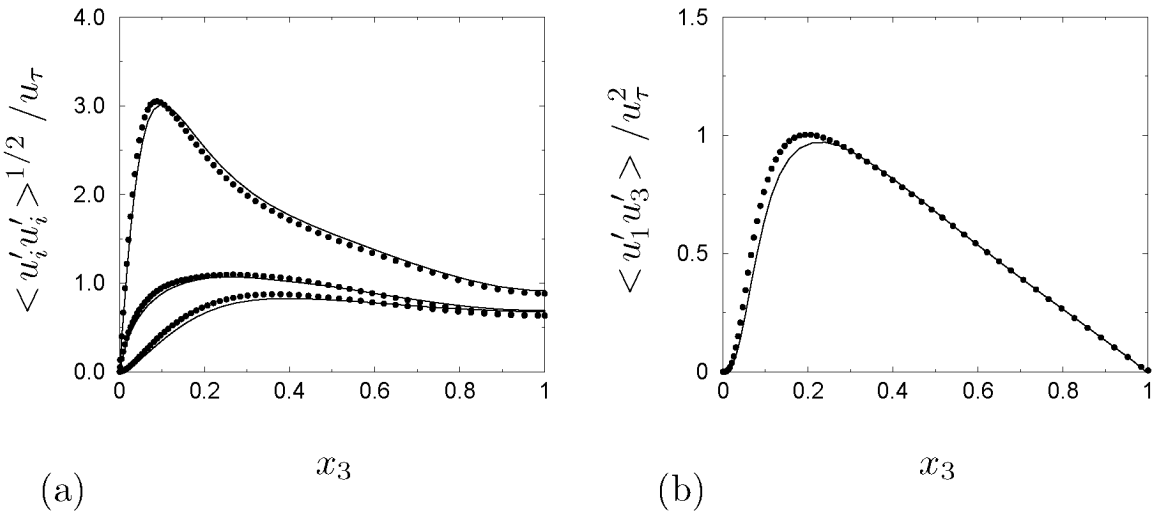

Figure 4.20: Results on a refined mesh with N_1=144, N_2=80, and N_3=120. (a) Velocity fluctuations, from top down, streamwise, spanwise and wall-normal, (b) Reynolds-stress; • ADM, ——— filtered DNS.

Chapter 5

Shock-boundary-layer interaction

Accurate computations of shock-boundary-layer interaction are needed in many aerospace and aeronautical applications to predict, for example, flows around transonic airfoils, supersonic air intakes or deflected control surfaces of vehicles at transonic or supersonic speed. To achieve an optimal and safe design of these high-speed vehicles or vehicle components, critical quantities such as skin-friction, heat transfer rates, fluctuating pressure and thermal loads have to be known precisely.

Experimental research in shock-boundary-layer interaction started in the mid-40's with the work of Ackeret *et al.* (1946) and has shown a constant interest since then (see Dolling (2001)). Numerical simulations of supersonic shock-boundary-layer interaction using Reynolds-averaged Navier-Stokes equations (RANS) methods are being made since the end of the 1970's. For example, Settles *et al.* (1979) compared experimental data with computations of the flow over a compression corner at high Reynolds number and observed that the RANS turbulence models at that time were unable to predict accurately the skin-friction, the location of the flow separation and reattachment, the surface pressure and the heat transfer for strong shock-turbulence interaction. More recently, Knight & Degrez (1997) made an evaluation on how well widely used turbulence models could predict these complex flows. Their conclusions were also rather disappointing for flows with significant separation, since quantities critical for the design of high-speed vehicles, such as the skin-friction and the heat transfer rates, could not be predicted with confidence whereas other parameters, such as the fluctuating pressure and thermal loads, could not be computed at all with RANS. Knight & Degrez (1997) attributed the poor results mainly to two causes. First, RANS calculations do not model flowfield unsteadiness. This can alter mean quantities since low-frequency unsteady phenomena are expected to influence these quantities. Second, turbulent eddy viscosity models characterize the turbulence using a single length scale, which is incorrect in separated flows. Other uncertainties in RANS simulations come from three-dimensional flow structures and compressibility effects.

Due to the limitations of RANS, LES is becoming more and more attractive to simulate numerically these kind of flows although today

it still can not be used straightforwardly. Challenges for LES of shock-turbulence interaction are identified on two levels: first, on the numerical level with the use of accurate, nondissipative and stable schemes, and second, on the level of LES with the requirement of a subgrid-scale model capable of providing a unified modeling of the turbulent and nonturbulent subgrid scales (shocks).

The development of numerical schemes for flows with discontinuities started well before one was thinking about using LES for this kind of flows. Lax & Wendroff (1960) already worked on this challenging task and derived the fundamental condition for a numerical discretization to correctly represent discontinuities. They stated that the numerical discretization of a conservation law had to be conservative in order to converge to the correct entropy solution of the problem. The convergence to a stable, nonoscillatory solution is however not assured.
Godunov (1959) with his upwind method, solved exact Riemann problems at cell interfaces but his method remained first-order accurate due to piecewise constant reconstruction of the cell value. The extension of similar upwind methods to higher-order accuracy came up against another difficulty, namely that in order to converge to the correct entropy solution in a nonoscillatory manner, the numerical method has to be monotone. Unfortunately, as demonstrated by Godunov, linear monotone methods are at most first order accurate, giving poor accuracy in smooth regions of the flow and smeared representation of discontinuities. Higher-order methods give much better accuracy on smooth solutions but fail near discontinuities, where oscillations are generated. The idea with high-resolution methods is to combine the advantages of the low- and high-order discretization properties. This can only be achieved by adding nonlinear terms to the second- or higher-order discretized conservation law. A wide variety of these nonlinear terms have been devised over the years. Artificial viscosity terms (von Neumann & Richtmyer, 1950; Swanson & Turkel, 1992) may be widely spread in CFD codes but the proper amount of artificial numerical dissipation is difficult to determine (see subsection 4.2.2). Therefore, flux-limiter and slope-limiter methods (Harten, 1983; Harten *et al.*, 1983; Sweby, 1984) which lead to so-called total variation diminishing (TVD) schemes have been developed. The TVD condition has been observed to be too strict in some cases, e.g. at extremal values, and a looser condition is obtained with the class of essentially nonoscillatory (ENO) schemes where the fluxes are computed via high-order cell-face reconstructed values (Harten *et al.*,

1987; Harten & Chakravarthy, 1991).
These different methods, commonly referred to as shock-capturing schemes, have shown to improve significantly the numerical representation of discontinuities and a detailed survey can be found in the book of Leveque (2002).

One open question with shock-capturing schemes is whether they qualify for LES since the dissipation introduced by the additional nonlinear terms may mask the effect of subgrid-scale models. This fundamental question was addressed by Garnier *et al.* (1999) who investigated the interaction between some widely used shock-capturing schemes and the Smagorinsky (1963) and the dynamic model of Germano *et al.* (1991). They came to the conclusion that in many cases the intrinsic numerical dissipation of the shock-capturing schemes masks the effect of the subgrid-scale model.
The idea of using the artificial dissipation of a numerical scheme in a turbulence modeling prospect was first proposed by Boris *et al.* (1992) who argued that it could mimic the effect of a subgrid-scale model. This approach is known as MILES (Monotonically integrated LES) and was investigated lately in more detail by Fureby & Grinstein (1999) and Garnier *et al.* (1999). The implicit modeling in MILES of the subgrid-scale terms has shown to give rather good results for free shear flow and forced homogeneous turbulence at higher Reynolds number whereas it does not perform so well for decaying turbulence or at lower Reynolds number. Recently, good results were also obtained for wall-bounded flows (Fureby & Grinstein, 2002).

Few studies have been undertaken so far to investigate the influence of subgrid-scale models on shocks. Subgrid-scale models have been developed to account for the energy transfer from resolved scales to nonrepresented scales and are often based on assumptions of turbulence isotropy or scale similarity which are not valid in the presence of a discontinuity. A challenge for the subgrid-scale model is to provide a unified modeling of the turbulent and nonturbulent subgrid scales (shocks).

Without any special shock treatment, Stolz *et al.* (2001*b*) obtained very good results of LES with ADM using a sixth-order compact finite difference discretization for the same flow configuration as considered in this chapter, i.e. the Mach 3 compression ramp. Recently, Adams & Stolz (2002) investigated more in depth if ADM was able to provide a unified treatment of flow discontinuities and turbulent subgrid scales. Using a sixth-order compact finite difference method, they varied the

order of the filter used for the relaxation regularization and performed tests for shock solutions of the Burgers and Euler equations. Low-order filters were observed to be more suitable for properly modeling the dissipation mechanism across a shock.
Garnier *et al.* (2002) studied shock-boundary-layer interaction by means of LES. They selected the two-dimensional interaction of an oblique shock on a flat plate boundary layer to assess the ability of the mixed-scale model (Sagaut, 2000) to cope with complex flows. The numerical scheme employed a combination of a fourth-order centered base scheme with a fifth-order accurate WENO filter. The results were compared with experimental data and showed good agreement except for cross term fluctuations that appeared underestimated. In relation with the MILES approach, they also performed computations without an explicit subgrid-scale model to evaluate the effect of the subgrid-scale model and noted that, except for an improved prediction of the skin-friction coefficient, its effect was globally rather small compared with the intrinsic dissipation of the numerical method.
Identical to the flow configuration studied here, Rizzetta & Visbal (2001) performed simulations of the flow over a supersonic compression ramp. They employed a sixth-order compact finite difference scheme in conjunction with a tenth-order nondispersive filter which is periodically applied to the solution. Because of the excessive diffusion of the shock due to the repeated filtering, they replaced the compact-differencing of the convective derivatives and filter operation by a third-order Roe upwind-biased method locally in regions of shock waves. The subgrid-scale terms were accounted for by the dynamic Smagorinsky model. The results of the numerical simulations were compared with experimental data, the latter were however obtained with significantly different flow parameters (Reynolds number two orders of magnitude higher) and geometric configuration (the sidewall end plates in the experiment were not modeled in the numerical simulation). Accordingly, the agreement between computed results and experimental data was rather qualitative than quantitative.

In this chapter, the computation of the supersonic flow over a compression ramp as performed with DNS by Adams (2000) and with LES and ADM by Stolz *et al.* (2001*b*) is reproduced. Unlike Stolz *et al.* who used a sixth-order compact finite difference scheme, a fourth-order finite volume scheme is used here. The aim is to evaluate the ability of ADM implemented in a lower order industrial flow solver to cope with complex

flows.
We begin by presenting the physical flow configuration and summarizing the parameters of the simulation. The results of LES with ADM where the deconvolution order is adapted locally to the flow are then compared with the filtered DNS data of Adams (2000).

5.1 The supersonic compression ramp

Following the flow configuration of Adams (2000), the turbulent boundary layer along a compression ramp with a deflection angle of 18° at a free-stream Mach number of M=3 and a Reynolds number of $Re_\theta = 1685$ with respect to free-stream quantities and mean momentum thickness at inflow is considered. Figure 5.1 gives a schematic representation of the flow. The compressible Navier-Stokes equations written in conservative form and nondimensionalized by the free-stream velocity u^*_∞, density ρ^*_∞, temperature T^*_∞, and the displacement thickness δ^*_1 of the mean boundary layer at inflow are solved. The time t is nondimensionalized with δ^*_1/u^*_∞. The fluid is assumed to be a perfect gas with a specific heat ratio of $\gamma = c_p/c_v = 1.4$. The nondimensional viscosity $\mu(T)$ is calculated from Sutherland's law

$$\mu(T) = T^{3/2}\frac{1+s}{T+s} \tag{5.1}$$

where s is a parameter depending on the gas and the temperature range, set here to $110.3K/T^*_\infty$. Table 5.1 gives an overview of the parameters of the simulation. At inflow, a turbulent boundary layer profile obtained from filtering DNS data from Adams (2000) are imposed. Non-reflecting boundary conditions are used at the outflow and on the upper boundary of the computational domain. No-slip isothermal conditions are applied at the wall and the flow is periodic in the spanwise direction (see section 2.6).

Results obtained with a second- and fourth-order discretization (see section 5.2.3) showed that the latter discretization reduced the oscillation amplitudes in the vicinity of the discontinuity and was therefore preferred here. The viscous fluxes are next computed using the gradient theorem on a shifted volume and the time integration is performed with an explicit four-stage Runge-Kutta scheme. See chapter 2 for more information.

parameter	value	comment
M_∞	3	free-stream Mach number
Re_{δ_1}	8977	Reynolds number based on the displacement thickness at the inflow (station 0), $u_\infty \rho_\infty \delta_1 / \mu_\infty$
Re_θ	1685	Reynolds number based on the momentum thickness at the inflow and ν_∞
Re_{δ_2}	732	Reynolds number based on the momentum thickness at the inflow and ν_w
δ_0	2.38	boundary layer thickness at inflow
θ	0.19	momentum thickness at inflow
T^*_∞	115K	free-stream temperature
T^*_w	2.522 T^*_∞	wall temperature
s^*	110.3K	Sutherland's law constant
Θ	18°	compression ramp angle
L_1	63.80	streamwise dimension
L_2	2.90	spanwise dimension
L_3	10.87	wall normal dimension at the inflow
L_3	21.40	wall normal dimension at the outflow
N_1	332	number of cells in streamwise dimension (1/3 of DNS Adams)
N_2	30	number of cells in spanwise dimension (3/8 of DNS Adams)
N_3	90	number of cells in wall normal dimension (1/2 of DNS Adams)
$\Delta_1^+\|_w$	18	streamwise cell size in wall units at inflow
$\Delta_2^+\|_w$	8.8	spanwise cell size in wall units at inflow
$\Delta_3^+\|_w$	1.4	wall normal cell size in wall units at inflow
$\Delta_1^+\|_w$	37.8	streamwise cell size in wall units at station 10
$\Delta_2^+\|_w$	20.4	spanwise cell size in wall units at station 10
$\Delta_3^+\|_w$	4.3	wall normal cell size in wall units at station 10

Table 5.1: Parameters of the numerical simulation. Subscript w indicates wall values.

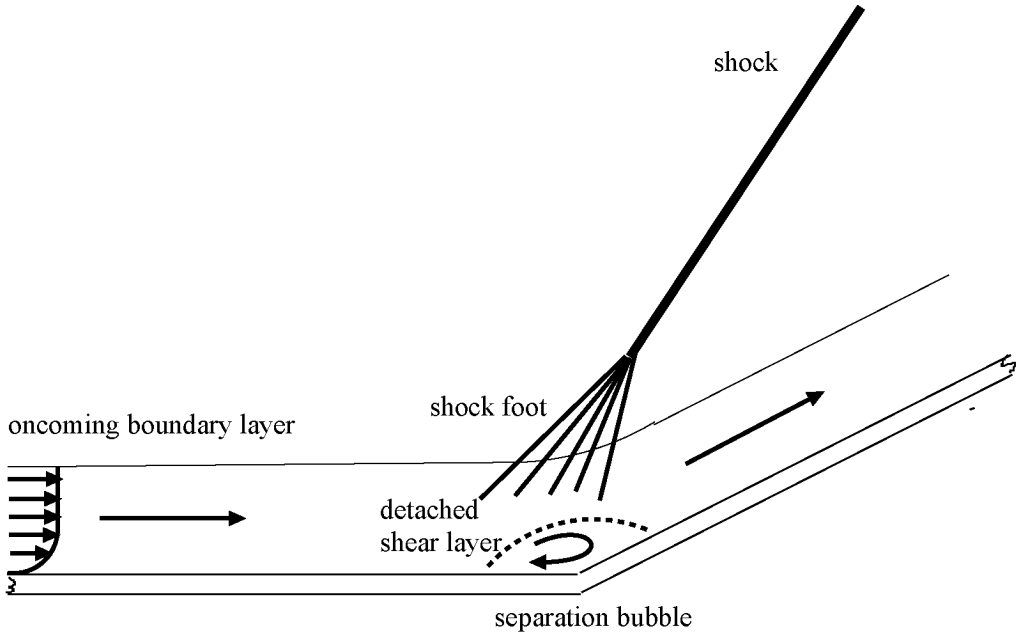

Figure 5.1: Sketch of the compression ramp configuration, from Adams (2000).

5.2 Results

In order to represent the turbulent flow and the shock properly, the computational mesh requested 1/3 of the number of points of the DNS of Adams (2000) in the streamwise direction, 3/8 in the spanwise direction and 1/2 in the wall-normal direction, leading to $N_1 = 332$, $N_2 = 30$, $N_3 = 90$ cells.
The simulation was started with interpolated DNS data from Adams and sampling was performed after an initial transient when a statistically steady state was reached. Angles $<.>$ indicate spanwise- and time-averaging and Favre filtered variables are denoted by $\tilde{f} = \overline{\rho f}/\overline{\rho}$. To obtain a consistent definition across the integration domain, in particularly near the corner of the ramp, the velocity vector is projected to a Cartesian system aligned with the wall. The contravariant velocities $\tilde{u}_i^c$ are defined as

$$\tilde{u}_1^c = \frac{\tilde{u}_1 \frac{\partial \xi_1}{\partial x_1} + \tilde{u}_3 \frac{\partial \xi_1}{\partial x_3}}{\sqrt{\left(\frac{\partial \xi_1}{\partial x_1}\right)^2 + \left(\frac{\partial \xi_1}{\partial x_3}\right)^2}} \tag{5.2}$$

$$\tilde{u}_2^c = \tilde{u}_2 \tag{5.3}$$

$$\tilde{u}_3^c = \frac{\tilde{u}_1 \frac{\partial \xi_3}{\partial x_1} + \tilde{u}_3 \frac{\partial \xi_3}{\partial x_3}}{\sqrt{\left(\frac{\partial \xi_3}{\partial x_1}\right)^2 + \left(\frac{\partial \xi_3}{\partial x_3}\right)^2}} \tag{5.4}$$

where $\xi_i = constant$ defines the grid lines of the computational mesh.

The remaining of this section is organized in three parts. First, the effect of the deconvolution order on the flow solution is examined. Second, based on the observations of the effect of the different deconvolution orders, the results of the supersonic compression ramp flow with the deconvolution order being locally adapted to the flow are presented and compared to DNS results. Finally, the grid dependence and the influence of the discretization order are investigated.

5.2.1 Effect of the deconvolution order

The difficulty for the subgrid-scale modeling consists in representing accurately the turbulent structures in the boundary layer, the detached shear layer of the separation bubble and the sharp gradients of the shock. We recall that a central scheme is used and that this kind of discretization generates oscillations in the vicinity of a discontinuity leading to nonlinear instability. A solution to prevent these oscillations would be to use an upwind scheme locally in the shock vicinity or to switch on artificial dissipation terms. This approach was consciously not followed in this evaluation phase of ADM with the finite volume method, since the effect of the subgrid-scale model would have been inseparable from the dissipation of the upwind scheme or from the artificial dissipation terms. The aim here is to obtain a stable and accurate representation of the discontinuity by acting on the subgrid-scale model instead of the discretization scheme and we therefore focus on suitably adapting the deconvolution order of the inverse filter (eq. 3.8) of ADM.

In eq. (3.22)-(3.26), the deconvolution order influences the deconvolved quantity $\mathbf{U}^\star = Q_N * \overline{\mathbf{U}} = \sum_{\nu=0}^{N} (I - G_1)^\nu * \overline{\mathbf{U}}$ and the relaxation term $-\chi(I - G_2) * \overline{\mathbf{U}}$. Reducing the deconvolution order has thus a double effect. First, the deconvolved quantity $\mathbf{U}^\star$ will be a poorer approximation of the exact unfiltered quantity $\mathbf{U}$, provided that the scales near the filter cutoff are well represented by the numerical discretization. For low-order schemes (including the fourth-order scheme used here), the error for wavenumbers near the cutoff is significantly larger than with

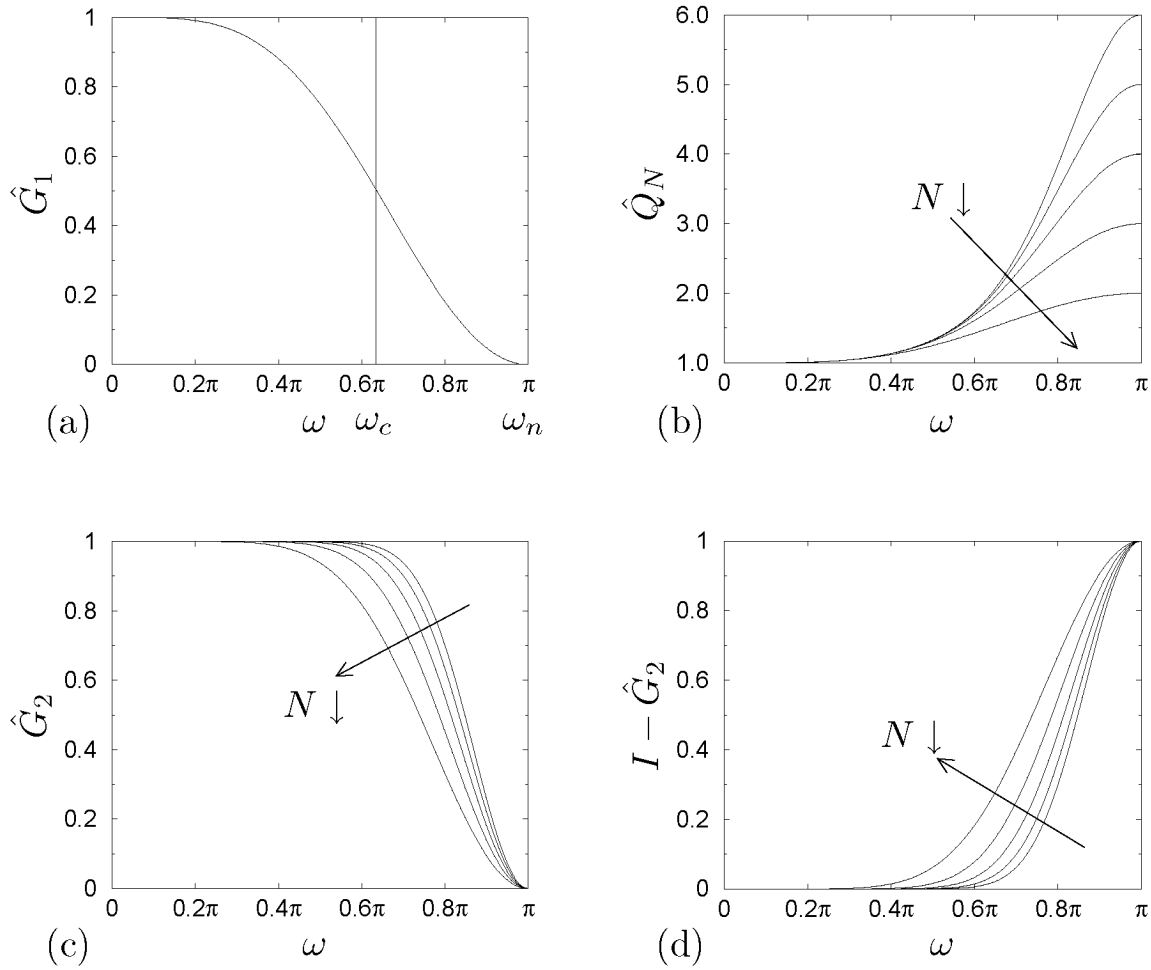

Figure 5.2: Transfer functions on an equidistant mesh; (a) primary filter $\hat{G}_1$, (b) approximate inverse $\hat{Q}_N$ (note that $\hat{Q}_N(\pi) = N + 1$), (c) secondary filter $\hat{G}_2 = \hat{Q}_N \cdot \hat{G}_1$, and (d) $I - \hat{G}_2$ for decreasing deconvolution order from $N = 5$ to $N = 1$.

a spectral representation (Lele, 1992). In this case, high-order deconvolution often only amplifies numerical noise and is not desired. The small-scale amplification effect with increasing deconvolution order N of the approximate inverse filter Q_N can be seen in figure 5.2 (b). Second, the wavenumber range from which energy is removed by the relaxation term will grow towards larger scales, damping larger-scale oscillations as they develop in the vicinity of a discontinuity. The increase of the range of scales being damped by the secondary filter G_2 with decreasing deconvolution order N can be seen in figure 5.2 (c) and (d). The effect on the flow of the relaxation term is comparable to a dissipation term,

e.g. the Jameson dissipation (Jameson *et al.*, 1981) and the reduction of the deconvolution order smoothes the solution in a similar way as artificial numerical dissipation. The difference between the two approaches resides in the fact that ADM does not modify the underlying differential equation in the resolved wavenumber range whereas classical numerical dissipation terms add high-order terms to the conservation law.

By applying the same deconvolution order (N=5) that had given good results for the supersonic channel flow (chapter 4; von Kaenel *et al.* (2003)), the oscillations near the shock permitted by the central schemes were not sufficiently damped and slowly grew and propagated away from the discontinuity until the calculation became unstable. Stable computations were obtained by reducing the deconvolution order, but the solution deteriorated then in the boundary layer where the cumulated effect of the physical viscosity and the low-order relaxation regularization showed an overdissipative behavior. The contradictory requirement of having a small dissipation in the boundary layer and sufficient dissipation in the vicinity of the discontinuity was solved by varying the deconvolution order as a function of the distance to the wall. Expressed in wall units ($.^+$), the deconvolution order is set to N=5 for $x_3^+ \lesssim 20$, N=4 for $20 \lesssim x_3^+ \lesssim 40$, N=3 for $40 \lesssim x_3^+ \lesssim 200$, N=2 for $200 \lesssim x_3^+ \lesssim 240$, N=1 for $240 \lesssim x_3^+$. With this repartition, the viscous wall region ($x_3^+ \lesssim 50$) is situated in the high deconvolution order region whereas the shock is entirely located in the N=1 area. Between the two extrema, the deconvolution order varies gradually (figure 5.3).

The positive effect of the variable deconvolution order on the skin-friction coefficient, which measures the velocity gradient at the wall, can be seen in figure 5.4 (a). Low-order deconvolution (N=1) near the wall clearly underpredicts the wall velocity gradient which is typical of an overdissipative behavior. The turbulent fluctuations in the boundary layer also show an overshoot with low-order deconvolution as can be observed in figures 5.4 (b), (c), and (d). The insufficient damping of the large scales oscillations is set in evidence in figures 5.4 (b) and (d) where the root-mean square (rms) fluctuations of the density and the Favre-averaged fluctuations of the Reynolds-stress are overpredicted in the vicinity of the shock when using a third-order deconvolution (the same trend is observed for the other fluctuating quantities but the differences in the mean quantities are only minimal). The results obtained with decreasing deconvolution order as a function of the wall distance show a better agreement with the reference data in the near wall region

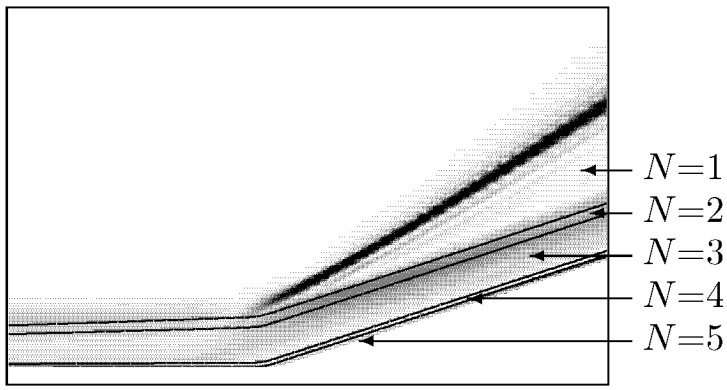

Figure 5.3: Decreasing deconvolution order N as a function of the wall distance with the density gradient magnitude shown in background. N=5 for $x_3^+ \lesssim 20$, N=4 for $20 \lesssim x_3^+ \lesssim 40$, N=3 for $40 \lesssim x_3^+ \lesssim 200$, N=2 for $200 \lesssim x_3^+ \lesssim 240$, N=1 for $240 \lesssim x_3^+$.

(figure 5.4 (a)), in the boundary layer and in the shock vicinity (figure 5.4 (b), (c), (d)).

Additional results on the effect of the deconvolution order, its influence on the relaxation coefficient χ and relaxation term $-\chi(I - G_2) * \overline{\mathbf{U}}$ are presented in the appendix A for the test problem of shock-wave propagation in a shock-tube.

5.2.2 Local adaptation of the deconvolution order

Based on the results of the previous subsection and of the appendix A, the benefit of the variable deconvolution order has become obvious, and all the results discussed further were obtained with decreasing deconvolution order as a function of the wall distance as described in section 5.2.1.

The density gradient magnitude averaged over the spanwise direction, displayed in figure 5.5, gives an overview of the flow. The DNS of Adams (2000) is shown on the left and the LES on the right. The instantaneous density gradient (figures 5.5 (a), (b)) corresponds to different flow realizations and can only be compared qualitatively. It can be seen that, due to the coarser mesh, the shock of the LES is slightly more smeared out but overall the LES exhibits the same flow patterns as the DNS.

For the mean and turbulent profiles, we compare ADM results with

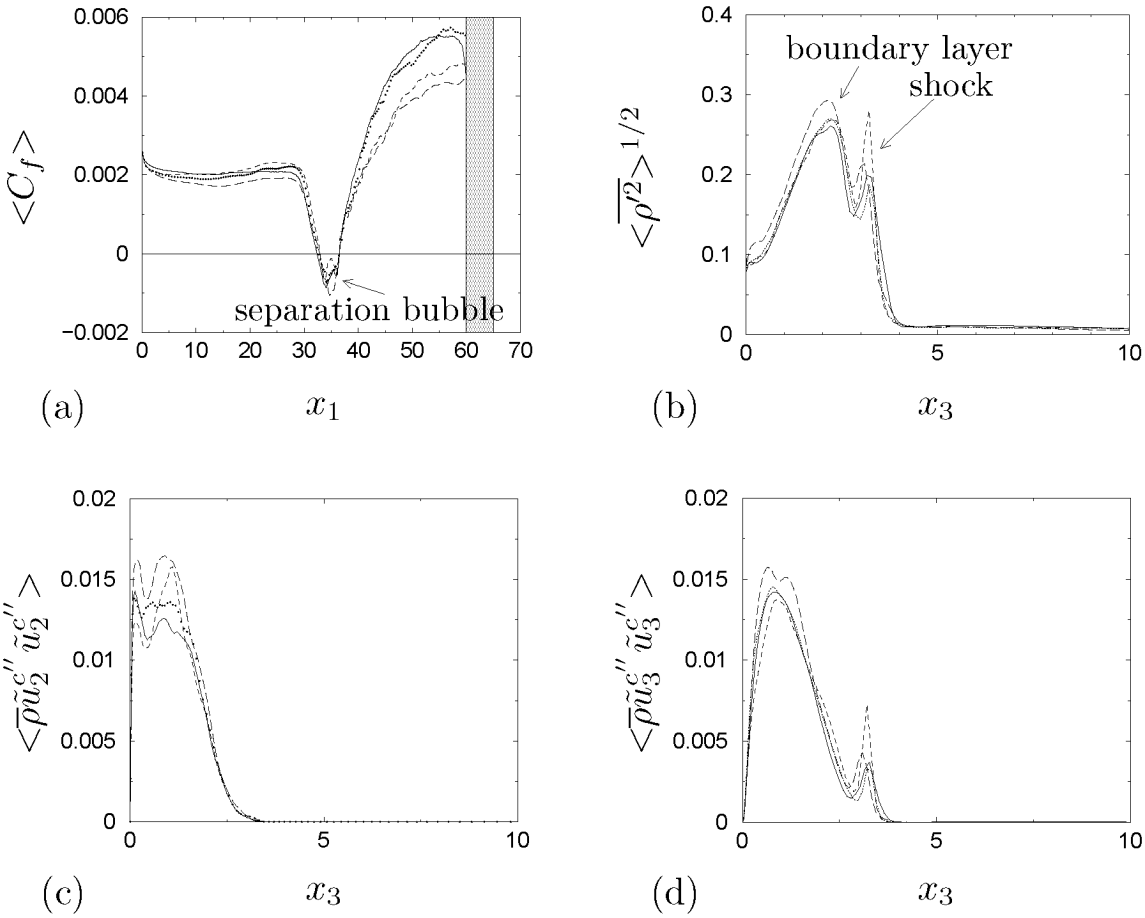

Figure 5.4: (a) Skin-friction coefficient $<C_f>$: ——— DNS, (b) density rms fluctuations $<\overline{\rho'^2}>^{1/2}$, (c) Reynolds-stress $<\overline{\rho}\tilde{u}_2^{c''}\tilde{u}_2^{c''}>$, (d) $<\overline{\rho}\tilde{u}_3^{c''}\tilde{u}_3^{c''}>$ at station 9 of figure 5.6: ——— filtered DNS, ····· decreasing deconvolution order from $N = 5$ near the wall to $N = 1$ above the boundary layer, - - - constant deconvolution order $N = 3$, ——— constant deconvolution order $N = 1$. The shaded area of graph (a) indicates the sponge region used as outflow boundary treatment in the DNS of Adams (2000).

the filtered DNS results of Adams at 10 different downstream stations along the computational mesh lines (see figure 5.6). The time-averaging covers 150 time units with a sampling period of 0.1. All mean profiles are very well predicted. Figure 5.8 show the Favre-averaged filtered contravariant velocity, temperature, pressure, and density profiles. Only small wiggles are observed near the shock, and the shock position and the boundary layer are very well predicted by the LES. The same trend can be observed for the contravariant momentum displayed in figure 5.9.

The van-Driest-transformed mean streamwise velocity $<\tilde{u}_1^c>_{VD}^+$ for a compressible boundary layer is defined as

$$<\tilde{u}_1^c>_{VD}^+ = \int_0^{<\tilde{u}_1^c>^+} \sqrt{\frac{\overline{\rho}}{\overline{\rho}_w}}\, d<\tilde{u}_1^c>^+ \quad . \tag{5.5}$$

This transformation accounts for the density variation across the boundary layer and allows for comparison with the logarithmic law of the velocity profile $2.5\ln x_3^+ + 5.5$. Figure 5.7 shows the mean, and van-Driest-transformed velocity profile scaled in wall units before (station 1) and after (station 10) the corner. As no shock is present before the compression corner, the flow is identical with a supersonic boundary layer and the agreement of the LES with the filtered DNS and the logarithmic law is very good. However, behind the compression corner the shock crosses the upper part of the computational domain and deviations from the logarithmic law can be observed in figure 5.7 (b). Some discrepancies between the filtered DNS and the LES can also be seen in the vicinity of the shock.

Wall quantities, e.g. the skin-friction coefficient which is computed as the gradient in the wall normal direction of the velocity parallel to the wall $<C_f> = 2\mu <\partial u_1^{\parallel}/\partial n>|_{wall}$, are among the most difficult quantities to predict correctly. Figure 5.10 (a) shows a very good agreement of the LES with the DNS and gives the correct location and length of the flow separation around the corner (region where $<C_f> \leqslant 0$). The wall pressure (figure 5.10(b)) shows also excellent agreement with the filtered DNS.

The turbulent fluctuations of the flow are analyzed by means of the Reynolds- and the Favre-averaged fluctuations which are computed as $f' := f - <f>$ and $f'' = f - <\overline{\rho}f> \,/\, <\overline{\rho}>$, respectively. The overall agreement between filtered DNS and LES is very good as can be seen for the density rms fluctuations $<\overline{\rho'^2}>^{1/2}$, the temperature Favre-averaged fluctuations $<\check{T}''^2>^{1/2}$, the streamwise contravariant momentum rms fluctuations $<\overline{\rho u_1^c}'^2>^{1/2}$, and the streamwise contravariant velocity Favre-averaged fluctuations $<\tilde{u}_1^{c''2}>^{1/2}$ in figure 5.11. The fluctuations within the boundary layer (first peak) and around the shock (second peak) are very well represented except for a slight discrepancy visible in the boundary layer around the corner of the ramp (stations 6-9) which coincides also with the foot of the shock. The same trend is observed for the Reynolds-stress Favre-averaged fluctuations $<\overline{\rho}\tilde{u}_1^{c''}\tilde{u}_1^{c''}>$,

$<\overline{\rho}\tilde{u}_2^{c''}\tilde{u}_2^{c''}>$, $<\overline{\rho}\tilde{u}_3^{c''}\tilde{u}_3^{c''}>$, and $<\overline{\rho}\tilde{u}_1^{c''}\tilde{u}_3^{c''}>$ shown in figure 5.12. The maximum deviation is less than 10% and occurs in the area of the corner of the ramp.
In comparison with the results of Stolz *et al.* (2001*b*) obtained with a sixth-order compact finite difference scheme, the mean and turbulent statistics here are of the same quality despite the lower order numerical method. The notable difference, however, is that in the present case, local adaptation of the deconvolution order was necessary whereas Stolz *et al.* used the deconvolution order $N = 5$ throughout the whole computational domain.

Figure 5.13 shows the time- and spanwise-averaged value of the relaxation coefficient χ for the continuity, momentum and energy equation. The relaxation parameter χ has the dimension of an inverse time scale and represents the frequency with which energy is annihilated by driving the filtered solution $\overline{\mathbf{U}}$ to a somewhat smoother solution $G_2 * \overline{\mathbf{U}}$ as the cutoff wavenumber of the secondary filter G_2 is significantly larger than the one of the primary filter G_1.
The largest values of the relaxation coefficient occur in the boundary layer which corresponds also to the region where the deconvolution order is high (N=5) to moderate (N=3). The large values of the relaxation parameter indicate that the frequency of the energy removal is high however mainly small scales are affected. Above the boundary layer, the deconvolution order is low ($N \leqslant 2$) and so the values of the relaxation parameter. This can be interpreted by the fact that in this area energy is removed over a larger scale spectrum and accordingly, the energy removal frequency is lower.
Figure 5.14 shows the root-mean square fluctuations of the relaxation coefficients. It is observed that the largest fluctuations appear in the vicinity of the shock which indicates that the energy fluctuations there are important. Although the relaxation term reached peak values in the boundary layer, the energy fluctuations are much smaller.

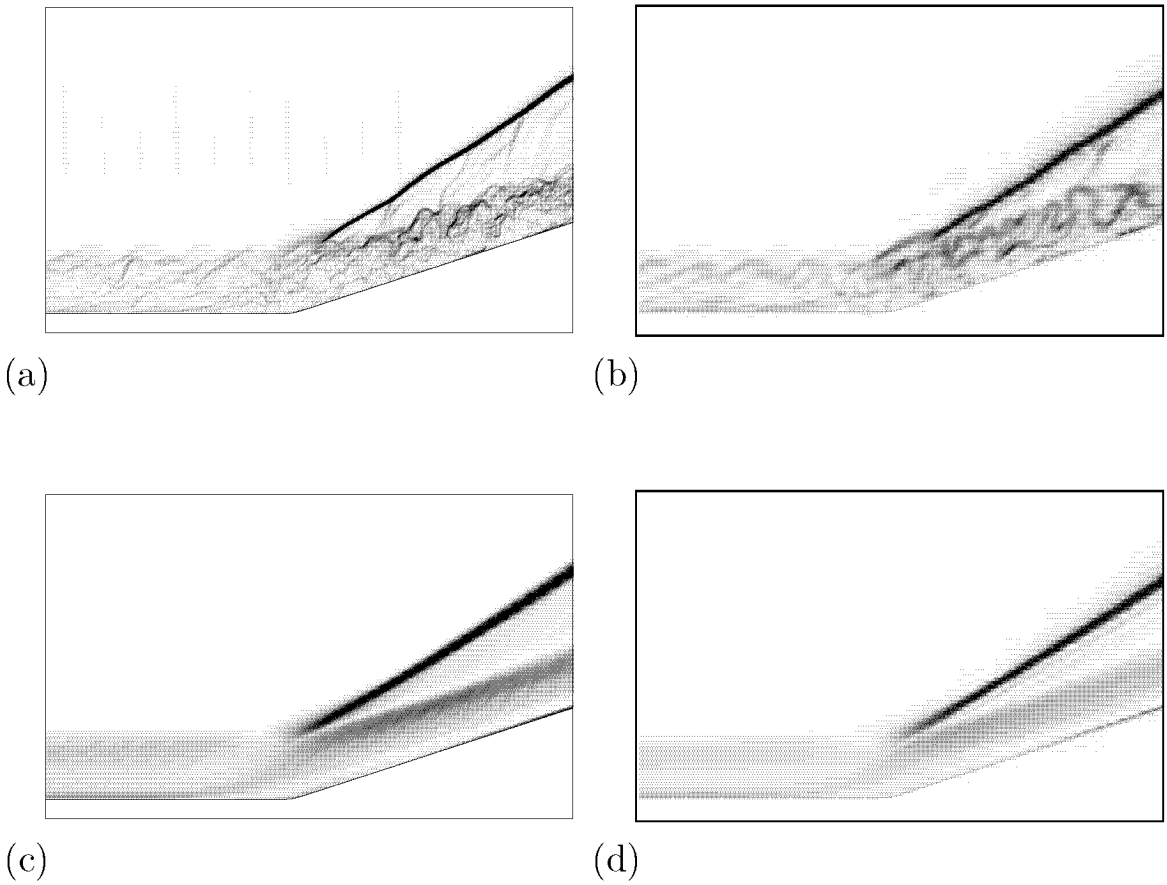

Figure 5.5: Flow-field Schlieren imitation $||\nabla\rho||$ contours; (a) spanwise-averaged DNS Adams (2000), (b) spanwise-averaged LES, (c) spanwise- and time-averaged DNS, (d) spanwise- and time-averaged LES.

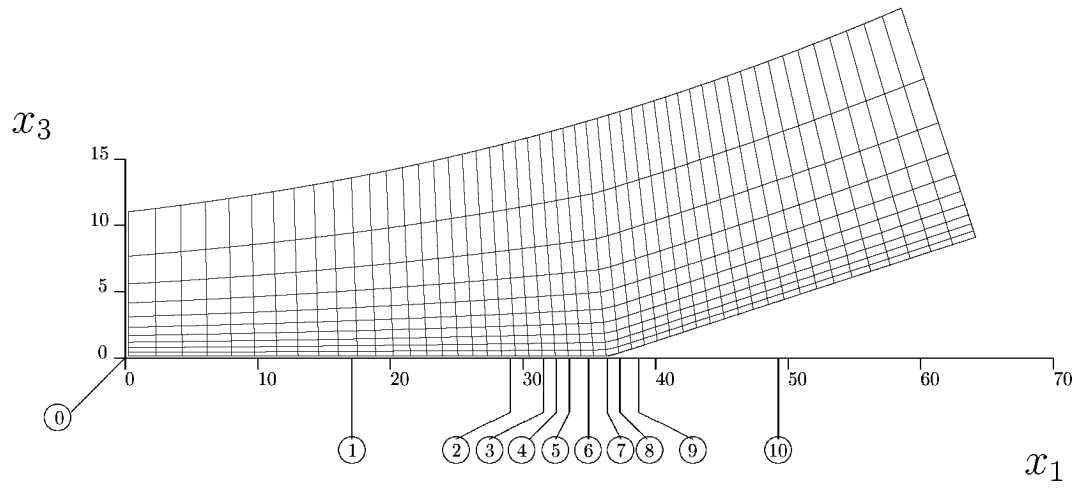

Figure 5.6: Computational mesh (each 9th line is shown); numbers in circles indicate stations where profiles are shown the following graphs.

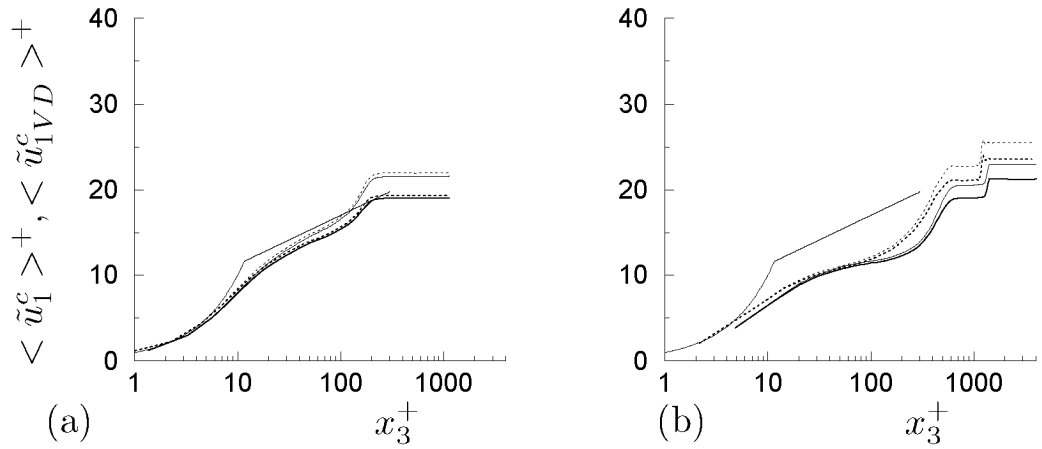

Figure 5.7: Contravariant velocity profiles scaled in wall units; (a) at station 1 and (b) at station 10; mean velocity $< \tilde{u}_1^c >^+$: ——— filtered DNS, ····· ADM; van Driest transformed mean velocity $< \tilde{u}_{1VD}^c >^+$: ——— filtered DNS, ----- ADM; ——— linear and logarithmic law (2.5 ln z^+ +5.5).

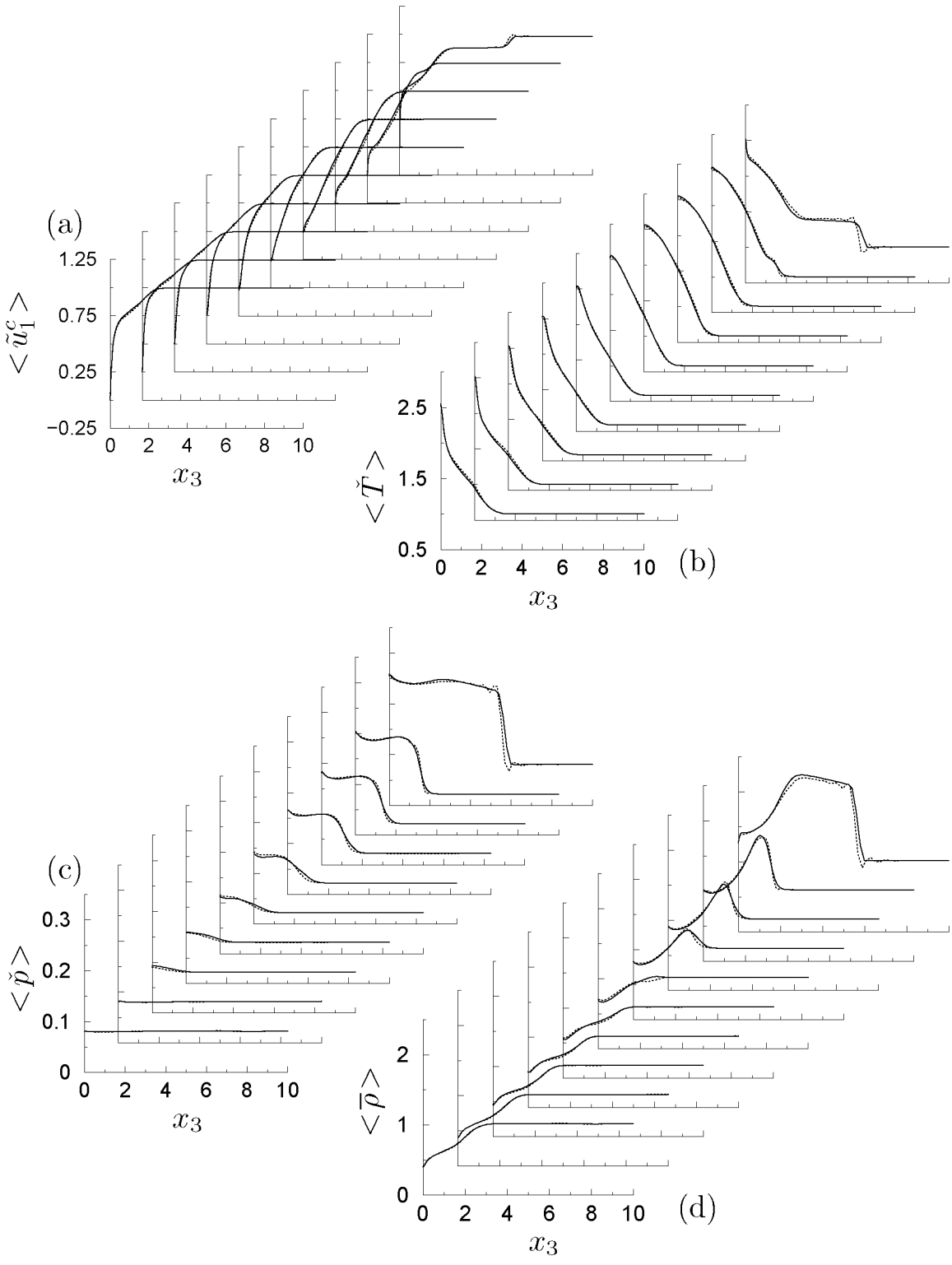

Figure 5.8: (a) Contravariant velocity $<\tilde{u}_1^c>$, (b) temperature $<\check{T}>$, (c) pressure $<\check{p}>$, (d) density $<\overline{\rho}>$, at the streamwise stations 1-10 according to fig. 5.6; ——— filtered DNS, ····· LES with ADM. The notation $\check{\bullet}$ indicates that the quantity is computed from the filtered solution, e.g., $\check{p} = (\gamma - 1)(\overline{E} - \overline{\rho u_i}\,\overline{\rho u_i}/(2\overline{\rho}))$.

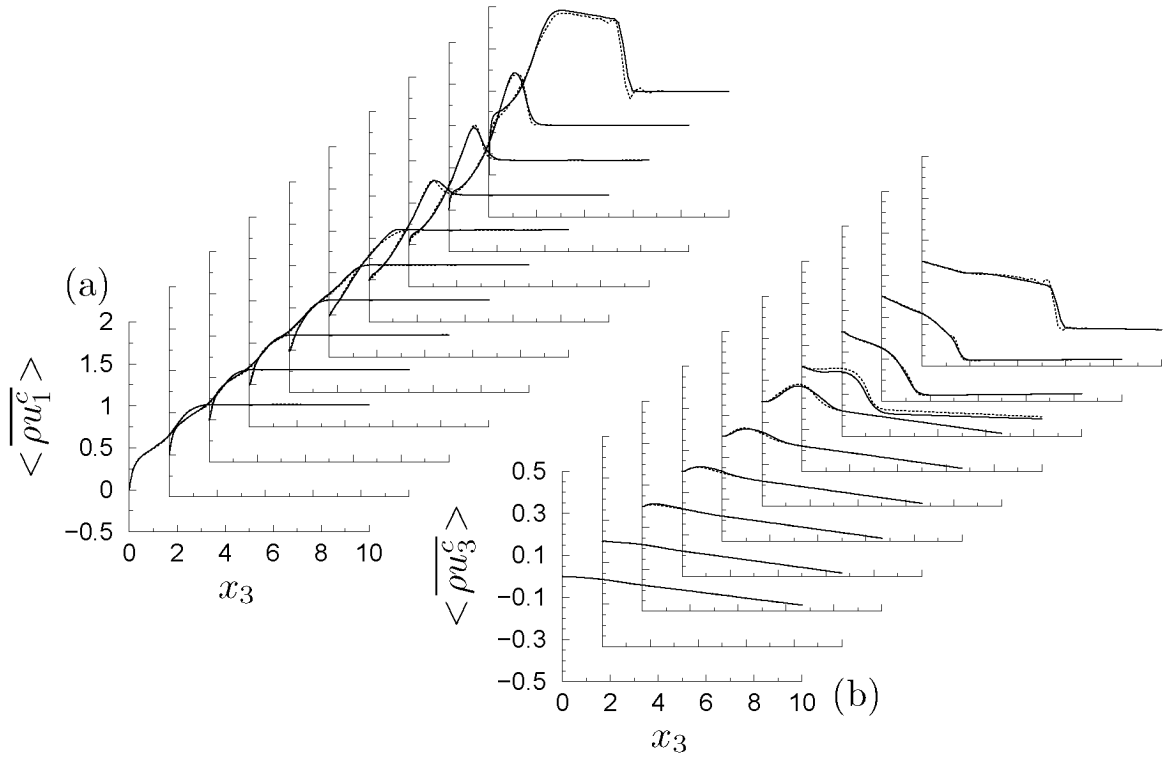

Figure 5.9: Contravariant momentum (a) streamwise $<\overline{\rho u_1^c}>$, (b) wall normal $<\overline{\rho u_3^c}>$, at the streamwise stations 1-10 according to fig. 5.6; ——— filtered DNS, ····· LES with ADM.

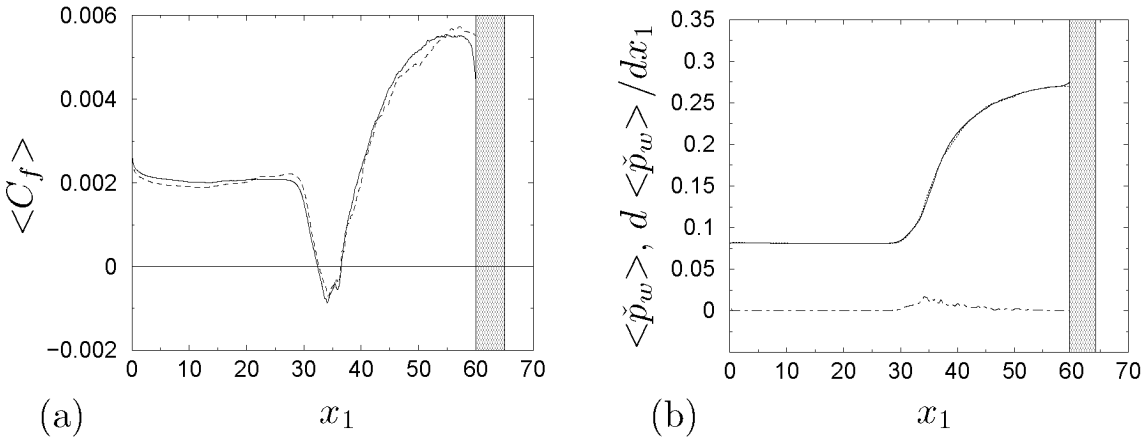

Figure 5.10: (a) Skin-friction coefficient $<C_f>$: ——— DNS, ····· ADM; (b) wall pressure $<\check{p}_w>$: ——— DNS, ····· ADM; streamwise pressure gradient: $d<\check{p}_w>/dx_1$: —·— ADM. The shaded area of graph (a) indicates the sponge region used as outflow boundary treatment in the DNS of Adams (2000).

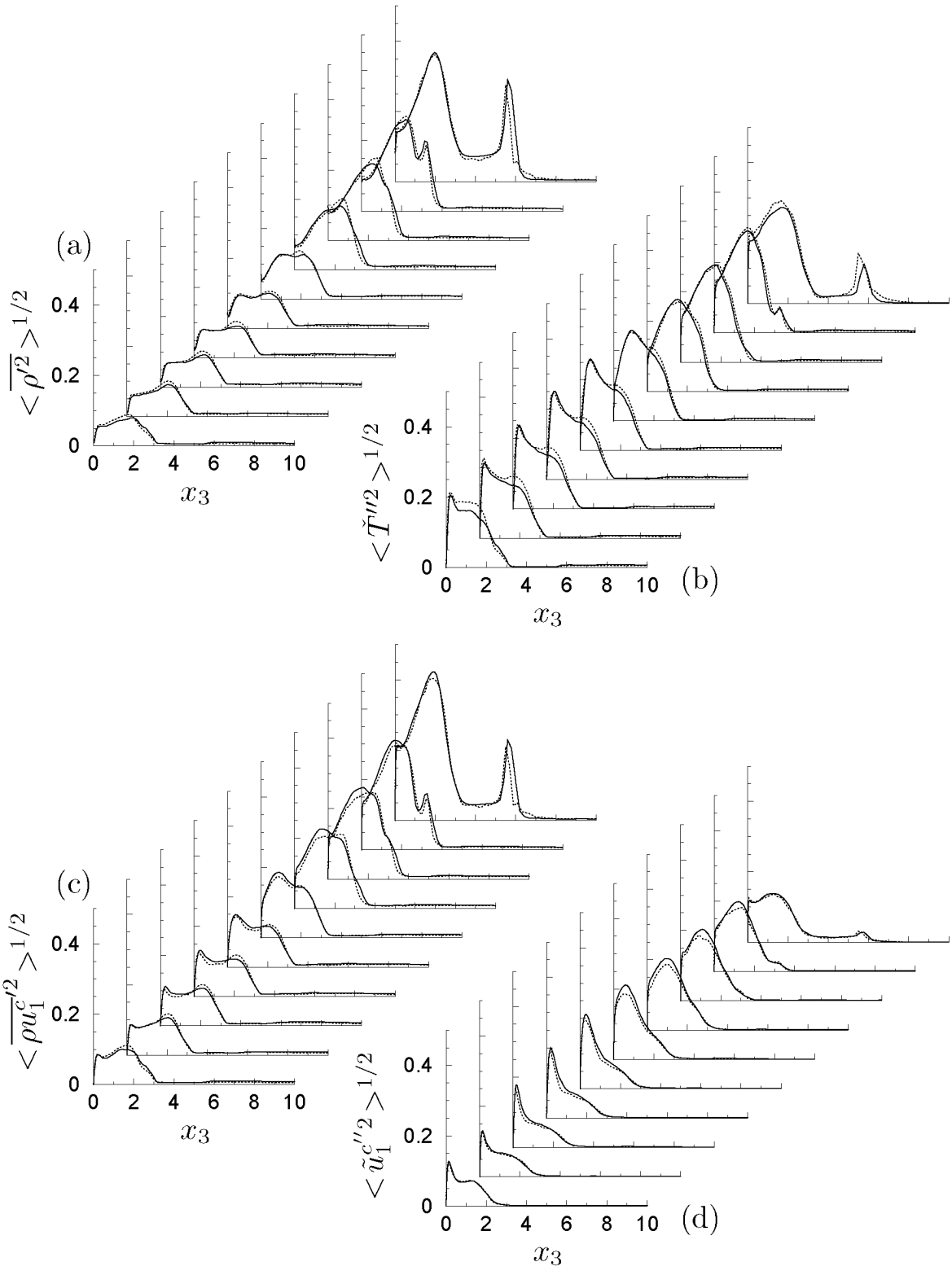

Figure 5.11: (a) Density rms fluctuations $<\overline{\rho'^2}>^{1/2}$, (b) temperature Favre-averaged fluctuations $<\check{T}''^2>^{1/2}$, (c) streamwise contravariant momentum rms fluctuations $<\overline{\rho u_1^c}'^2>^{1/2}$, (d) streamwise contravariant velocity Favre-averaged fluctuations $<\tilde{u}_1^{c''2}>^{1/2}$, at the streamwise stations 1-10 according to fig. 5.6; ——— *filtered DNS,* ····· *LES with ADM.*

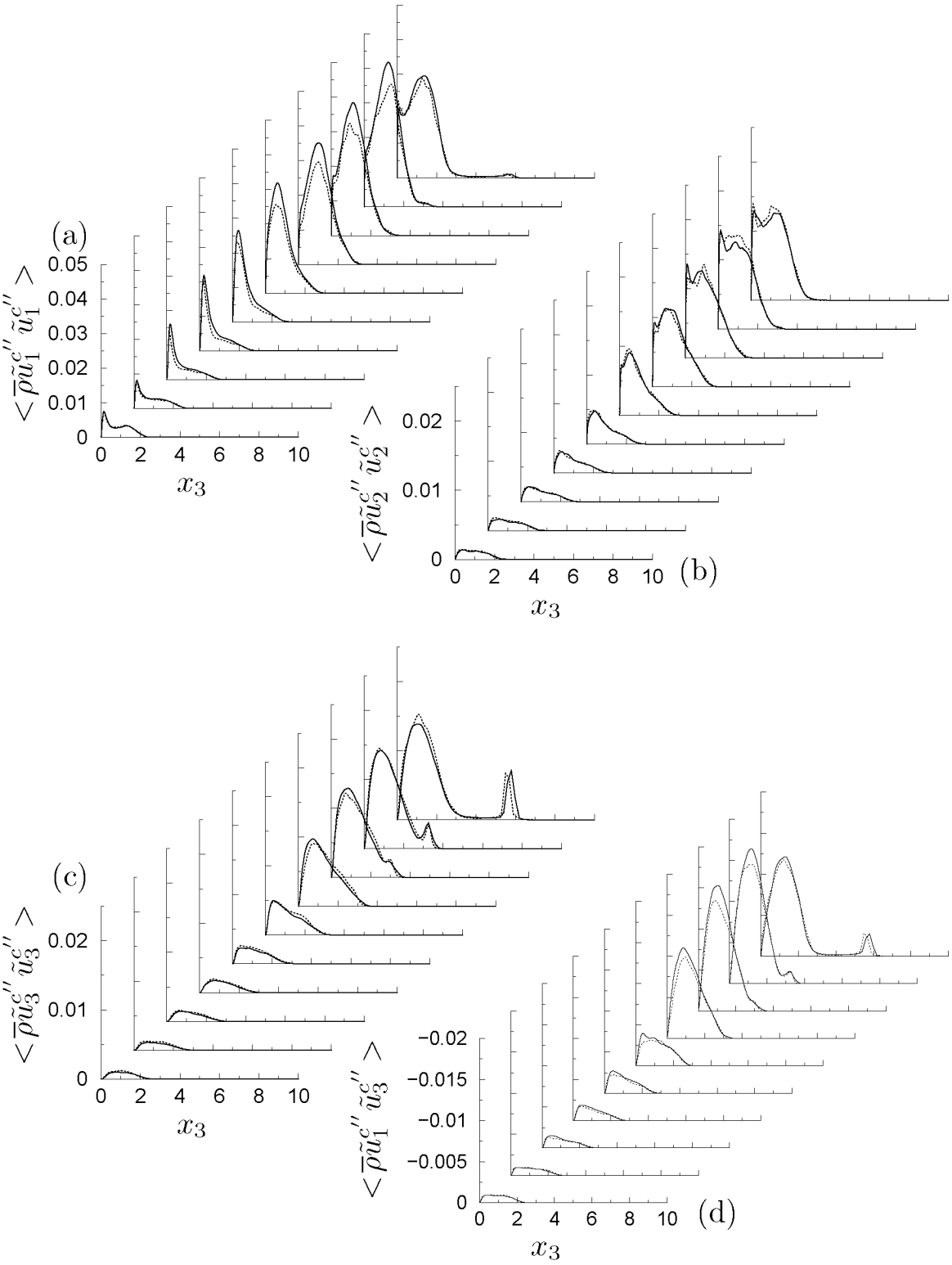

Figure 5.12: Reynolds-stress; (a) $< \overline{\rho}\tilde{u}_1^{c''}\tilde{u}_1^{c''} >$*, (b)* $< \overline{\rho}\tilde{u}_2^{c''}\tilde{u}_2^{c''} >$*, (c)* $< \overline{\rho}\tilde{u}_3^{c''}\tilde{u}_3^{c''} >$*, (d)* $< \overline{\rho}\tilde{u}_1^{c''}\tilde{u}_3^{c''} >$*, at the streamwise stations 1-10 according to fig. 5.6;* ——— *filtered DNS,* ····· *LES with ADM.*

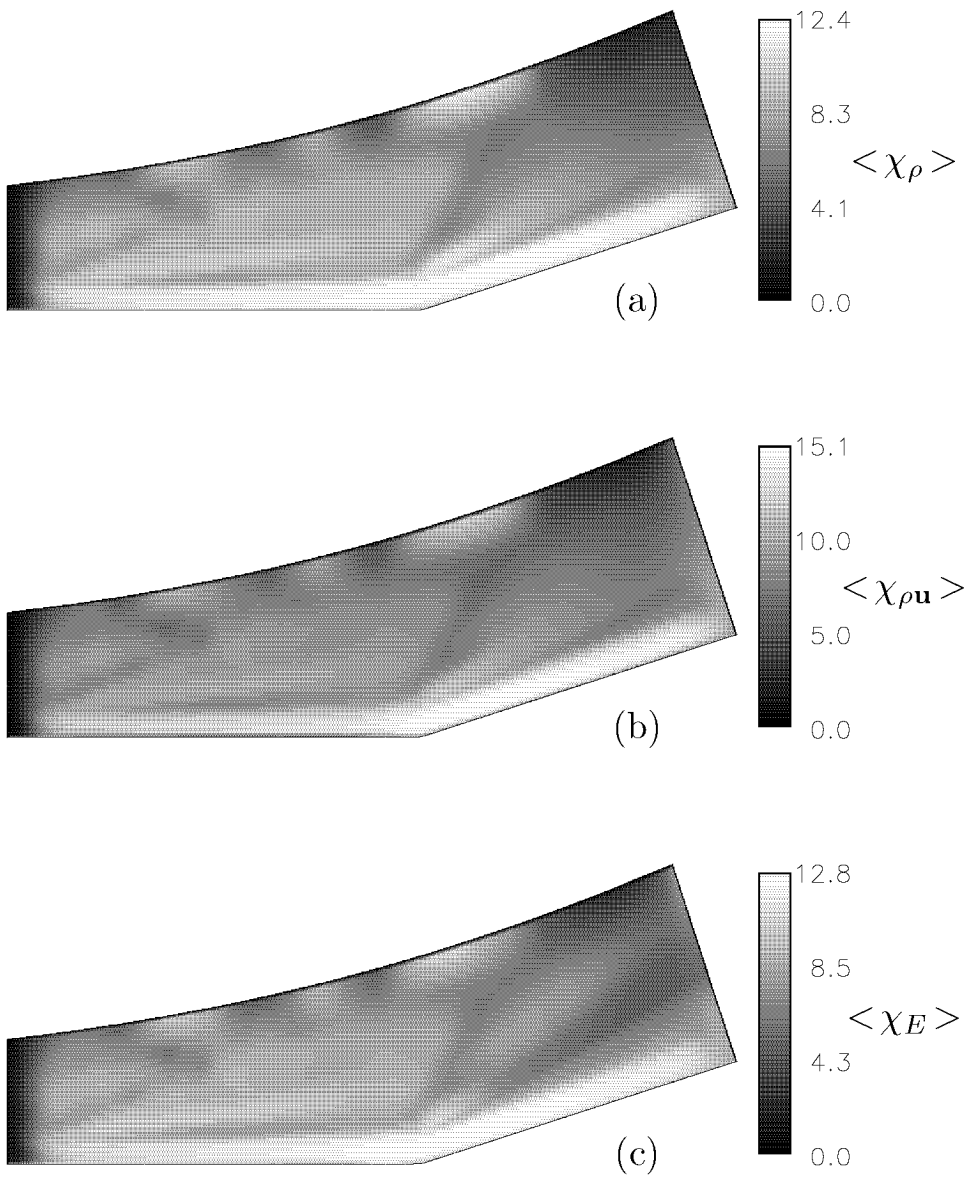

Figure 5.13: Time- and spanwise-averaged relaxation coefficient with decreasing deconvolution order as a function of the wall distance, (a) relaxation coefficient for the continuity, (b) momentum, (c) energy equation.

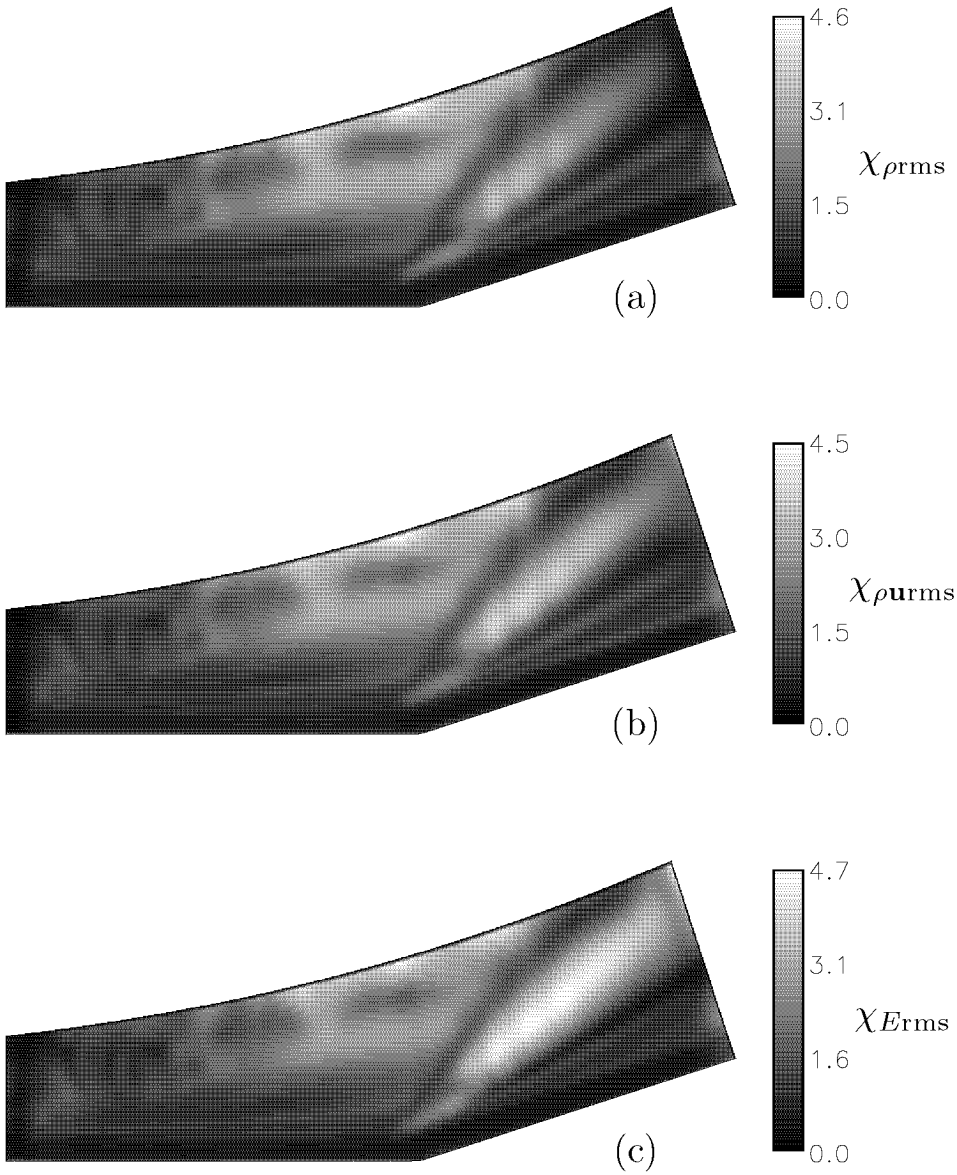

Figure 5.14: rms fluctuations of the relaxation coefficient with decreasing deconvolution order as a function of the wall distance, (a) fluctuations of the relaxation coefficient for the continuity, (b) momentum, (c) energy equation.

5.2.3 Numerical tests

Computations with the convective terms discretized with a second-order skew-symmetric scheme (see section 2.3.1) have also been performed. The deconvolution order distribution is identical than previously.
For the mean profiles of figure 5.15, the agreement between filtered DNS and LES remains good except for larger oscillations in the vicinity of the shock. For the fluctuating quantities of figure 5.16, the deviation from the filtered DNS is larger with the second-order than with the fourth-order discretization.

The mesh dependence has been investigated by refining the computational mesh to N_1=500, N_2=40, and N_3=120 cells (1/2 in each direction of the number of grid points of the DNS of Adams (2000)). The convective terms are again discretized with the fourth-order skew-symmetric and the deconvolution order distribution is similar to previously.
For the mean profiles (figure 5.17), the agreement between filtered DNS and LES is excellent and the effect of the grid refinement is mainly visible in the shock vicinity where the oscillations are minimal. The results for the fluctuating quantities (figure 5.18) are of the same quality than the ones obtained with the coarser mesh and confirm the mesh independence of the previous results. The computational cost of the fine-mesh LES (N_1=500, N_2=40, and N_3=120 cells) is about 1.5% of the DNS and the computational cost of the LES with the mesh of N_1=332, N_2=30, and N_3=90 cells is about 0.5% of the DNS.

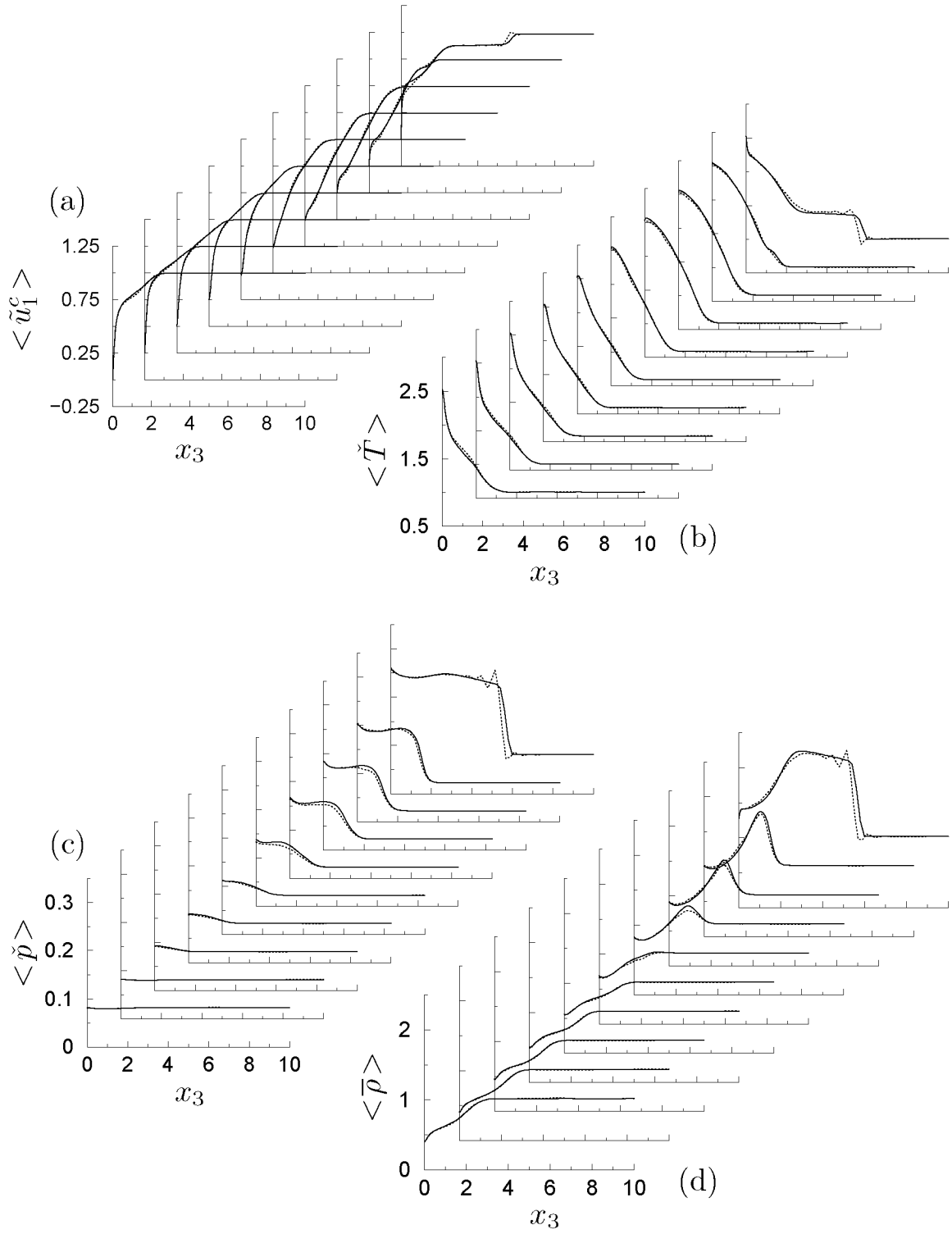

Figure 5.15: Mean profiles obtained with the central second-order scheme. (a) contravariant velocity $<\tilde{u}_1^c>$, (b) temperature $<\check{T}>$, (c) pressure $<\check{p}>$, (d) density $<\overline{\rho}>$, at the streamwise stations 1-10 according to fig. 5.6; ——— *filtered DNS,* ····· *LES with ADM. The notation* $\check{\bullet}$ *indicates that the quantity is computed from the filtered solution, e.g.,* $\check{p} = (\gamma - 1)(\overline{E} - \overline{\rho u_i}\,\overline{\rho u_i}/(2\overline{\rho}))$.

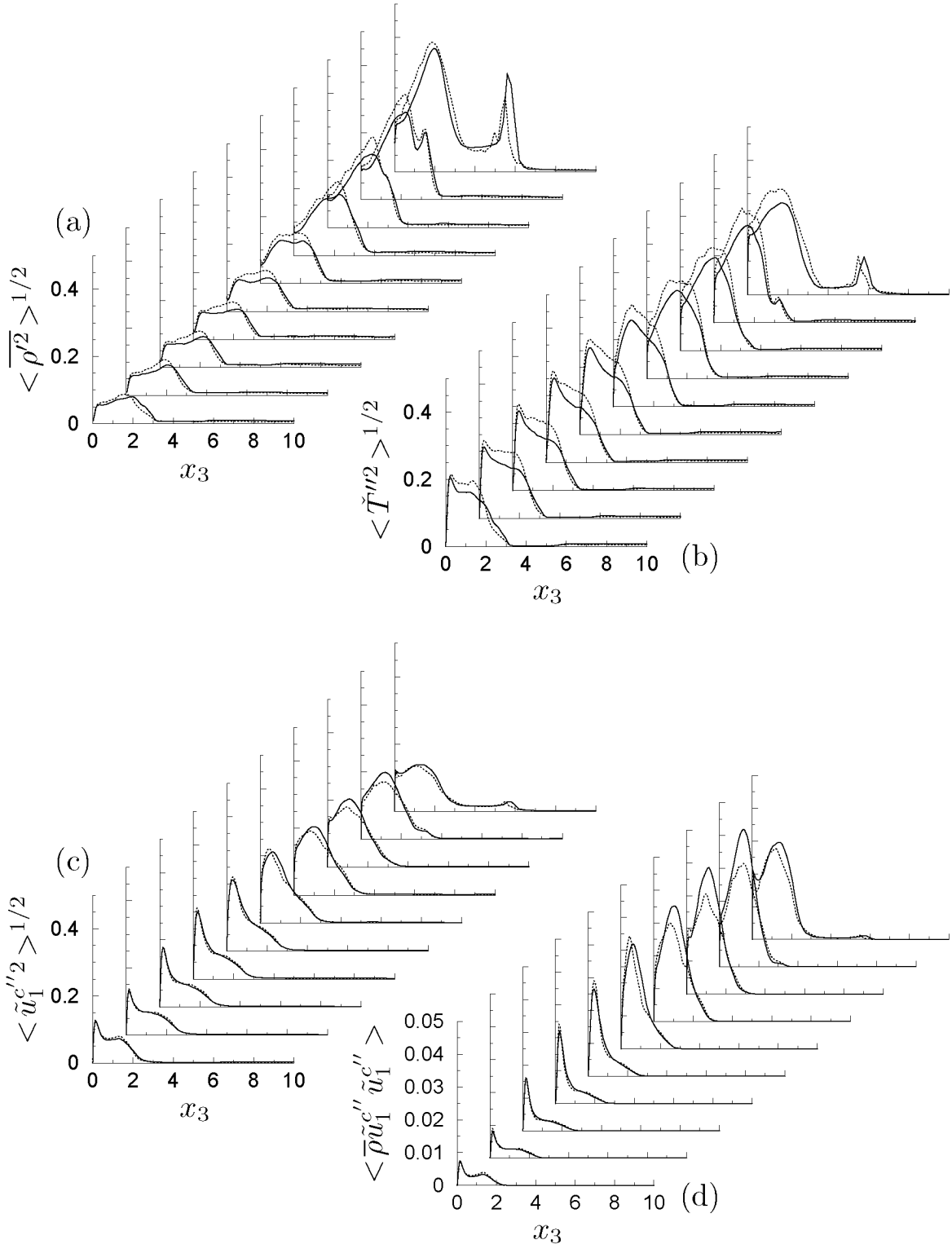

Figure 5.16: Fluctuating quantities obtained with the central second-order scheme. (a) density rms fluctuations $<\overline{\rho'^2}>^{1/2}$, (b) temperature Favre-averaged fluctuations $<\check{T}''^2>^{1/2}$, (d) streamwise contravariant velocity Favre-averaged fluctuations $<\tilde{u}_1^{c''2}>^{1/2}$, (c) Reynolds-stress $<\overline{\rho}\tilde{u}_1^{c''}\tilde{u}_1^{c''}>$, at the streamwise stations 1-10 according to fig. 5.6; ——— *filtered DNS,* ····· *LES with ADM.*

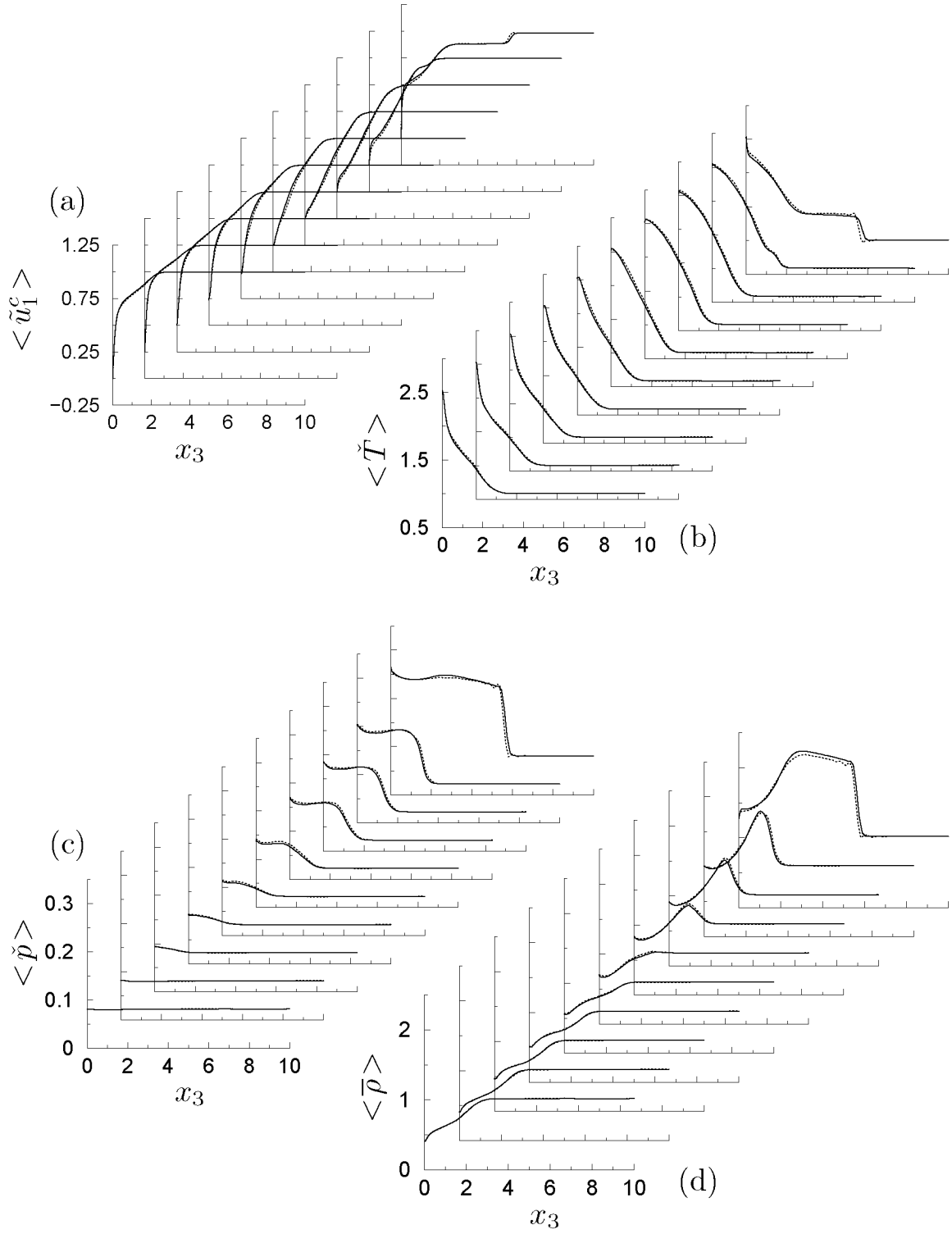

Figure 5.17: Mean profiles obtained with the central fourth-order scheme with a mesh N_1=500, N_2=40, N_3=120. (a) contravariant velocity $<\tilde{u}_1^c>$, (b) temperature $<\check{T}>$, (c) pressure $<\check{p}>$, (d) density $<\overline{\rho}>$, at the streamwise stations 1-10 according to fig. 5.6; ——— filtered DNS, ····· LES with ADM.

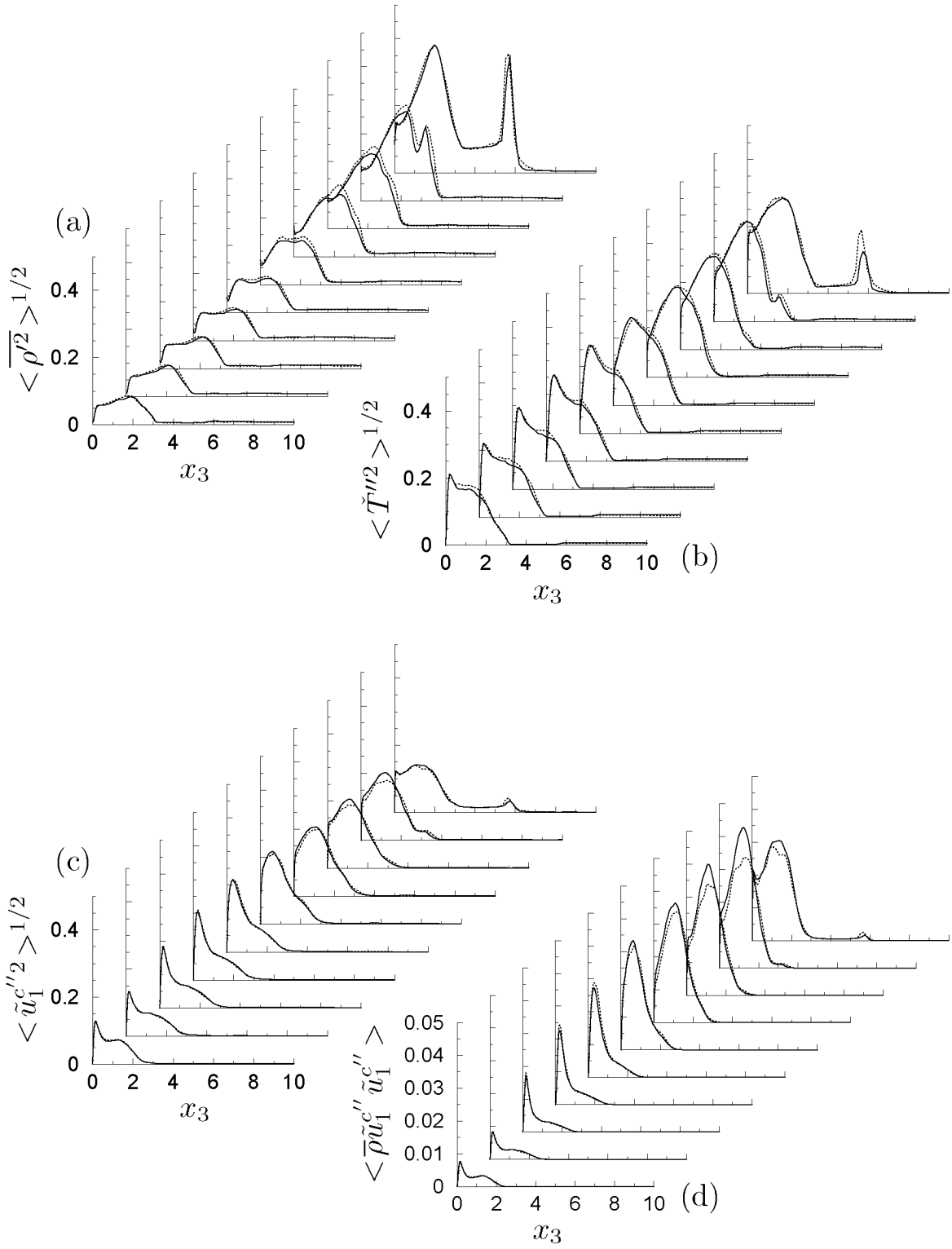

Figure 5.18: Fluctuating quantities obtained with the central fourth-order scheme with a mesh N_1=500, N_2=40, N_3=120. (a) density rms fluctuations $<\overline{\rho'^2}>^{1/2}$, (b) temperature Favre-averaged fluctuations $<\check{T}''^2>^{1/2}$, (d) streamwise contravariant velocity Favre-averaged fluctuations $<\tilde{u}_1^{c''2}>^{1/2}$, (c) Reynolds-stress $<\overline{\rho}\tilde{u}_1^{c''}\tilde{u}_1^{c''}>$, at the streamwise stations 1-10 according to fig. 5.6; ——— *filtered DNS,* ····· *LES with ADM.*

Chapter 6

Summary and conclusions

Despite nearly four decades of work in universities and research institutes, LES still needs to establish itself as an industrial CFD tool. The aim of the present work was to achieve a step in this direction for one particular subgrid-scale model, ADM, from use in an academic framework to applicability in an industrial flow solver. Therefore ADM, so far applied with high-order compact finite-difference or spectral schemes only, was extended to the finite-volume method and implemented in an industrial CFD code (NSMB). Validation of the implementation of ADM and evaluation of the model was then performed with two flow configurations of increasing complexity: the turbulent compressible channel flow and the supersonic flow over a compression ramp.

The isothermal-wall channel flow was selected first to validate the implementation of ADM and to evaluate the model in the challenging near-wall area. The Mach number based on the wall temperature was 1.5 and the Reynolds number based on the bulk (averaged) quantities and the channel half-width was Re_b=3000, reproducing thus the simulation of Coleman *et al.* (1995). The numerical integration was carried out with a Jameson-type scheme, which combines a four-stage Runge-Kutta time integration with a central second-order spatial discretization.
The mean profiles and the turbulent fluctuations of LES with ADM were observed to be in good agreement with filtered DNS data. To evaluate the behavior of the numerical scheme used for the LES, a no-model computation, or underresolved DNS, was performed. In the absence of discontinuities, the dealiasing property of the skew-symmetric formulation (Blaisdell *et al.*, 1996) of the convective terms was observed to be able to keep the computation stable without artificial dissipation terms. Moreover, for the mean profiles and the turbulent fluctuations, the agreement between the no-model computation and the DNS was as good on average as the one observed between ADM and the filtered DNS, which demonstrated a rather small effect of the model in this case. Only the energy spectra revealed the inability of the no-model computation to correctly represent the small-scale dissipation mechanism.
The ability of standard artificial numerical dissipation to replace the relaxation regularization procedure in LES using ADM was investigated

next. The benefit of this modification of the ADM is to simplify its implementation and to make it more attractive for industrial flow solvers using similar numerical methods. It was shown that for suitably chosen values of the dissipation coefficients, the simplified method was able to compete with the relaxation term of ADM, but the results deteriorated quickly for inadequate values of these coefficients. The severe drawback of artificial dissipation thus resides in determining the best values for the dissipation coefficients, which are grid- and flow-dependent and can only be found by trial and experience.

Following the good results obtained for the smooth channel flow, the more complex problem of shock-turbulence interaction on a compression ramp was considered. The presence of a discontinuity in the flow field allowed for testing if ADM, with low-order schemes, can provide a unified modeling of turbulent and nonturbulent (shocks) scales.
The DNS case of Adams (2000) was selected with a ramp deflection angle of 18°, a free-stream Mach number of 3 and a Reynolds number of $Re_\theta = 1685$ with respect to free-stream quantities and mean momentum thickness at inflow. The same numerical scheme as for the channel flow was used, except for a fourth-order spatial discretization which demonstrated a better behavior in the vicinity of the shock than the second-order scheme. Remarkably, no artificial numerical dissipation needed to be used to damp the oscillations developing near the discontinuity, but the order of the secondary filter of ADM had to be lowered so as to maintain an accurate and stable computation. In the turbulent boundary layer, low-order deconvolution showed to be overdissipative so that the deconvolution order in this region was increased. The very good agreement observed between LES with ADM and the filtered DNS showed that the local adaptation of the deconvolution order to the nature of the flow improved the results significantly.

The overall results of ADM with finite-volume schemes look encouraging for a possible future use of the model in an industrial framework. A number of issues, however, require further investigations before this step can be achieved.

A widely unresolved problem regards the treatment of the near-wall area. For the two cases investigated in this study, good results were obtained. However, this success has to be put in relation to the fairly low Reynolds number which allowed to resolve the viscous wall region. No special wall treatment is used with ADM which requires thus a similar near-wall resolution as a DNS. For industrial wall-bounded flows, the

Reynolds number is typically a factor of 10^3 higher and the according near-wall resolution is not computationally feasible. One way to bypass the computational bottleneck of resolving the near-wall region would be to adopt an approximate non-LES treatment to bridge the viscous wall region. ADM would then be applied in the outer flow region only and the viscous layer would be predicted by means of wall functions or RANS models, joining thus formally the so-called DES approach (Spalart *et al.*, 1997; Constantinescu *et al.*, 2002). Nontrivial coupling problems between the near-wall layer and the LES domain remain however to be addressed and solved.

Another topic which would need further investigations concerns the treatment of discontinuities. A satisfactory solution to the unified modeling of turbulence and discontinuities was found here with a local adaptation to the flow phenomena of the deconvolution order. The *a priori* knowledge of the flow allowed for determining "manually" the deconvolution order within certain regions of the computational domain. An improvement would consist in adjusting the deconvolution order automatically, based on the analysis of certain flow outputs, e.g., a pressure sensor to locate the shock position. The actual realization was not carried out here as it appears more to be an implementation task (such pressure sensors exist already for artificial numerical dissipation) than a task of fundamental scientific interest. An alternative to variable deconvolution order to damp oscillations around the shock is to prevent their occurrence by acting on the numerical integration method. In the present case, central schemes which are known to generate oscillations around discontinuities were used. If instead, as done by Rizzetta & Visbal (2001), an upwind method was used locally in regions of shocks, or artificial numerical dissipation terms were switched on, no special care of the discontinuities on the subgrid-scale modeling level would be required. This approach was deliberately not followed in this evaluation phase of ADM in the finite-volume framework, since the effect of ADM on shocks and the intrinsic numerical dissipation of upwind schemes or the artificial dissipation terms would have been inseparable.

A final remark could be expressed in form of a recommendation. The good results obtained without any subgrid-scale model for the turbulent channel flow should incite LES users to evaluate their numerical method without explicit subgrid-scale terms before spending substantial resources in deriving and testing models whose effect could already be simulated by the underlying numerical scheme, or greatly masked by

it. The investigation of the intrinsic dissipation of monotone numerical schemes for use in a turbulence simulation prospect started with the work of Boris *et al.* (1992) and has become known as MILES. Ever since the method has shown growing interest both on a practical level with several academic and industrial applications (Grinstein & Fureby, 2002, 2003) and on a more theoretical level with the recent attempt of Rider & Margolin (2003) to explain the good behavior of monotone schemes by relating their truncation error to the analytical form of well-known subgrid-scale terms. The good results of MILES for a wide range of flow configurations, but mainly its resourceful simplicity, could inspire simplified variants of ADM which would possibly be more attractive for nonacademic users. For example, with low-order schemes and except in viscous regions of the flow, a global reduction of the deconvolution order in the nonlinear terms and in the secondary filter could be considered without loss of quality to save computational time. Furthermore, as already demonstrated by tests, the space- and time-dependent relaxation parameter χ can be replaced by an appropriate constant value without deteriorating significantly the solution.

Appendix A

Shock-tube

The shock-tube problem (Sod, 1978; Leveque, 2002) was considered to test the ability of ADM to represent accurately shock waves. The absence of turbulence allows for a clear evaluation of the energy dissipation mechanism across the discontinuity.

For this configuration, a diaphragm at the location x=0.5 initially separates a left (subscript l) and a right (subscript r) region of the flow which have different densities and pressures. The two regions are in a constant state with pressure p_l=1, p_r=0.1, density ρ_l=1, ρ_r=0.125, and a zero velocity on each side of the diaphragm so that both fluids are initially at rest (figure A.1, t=0). At time t=0 the diaphragm is broken. A shock wave, followed by a contact discontinuity propagate then to the right and an expansion fan propagates to the left (figure A.1 t=0.2). To avoid the reflection of the shock and the expansion fan at the boundaries, we focus on the timespan before any wave has reached the boundary of the computational domain. Furthermore, an inviscid fluid is assumed so that the one-dimensional Euler equations are considered. The temporal integration is carried out until t=0.2 and the spatial mesh size is Δx=0.005. For consistency with the compression ramp flow, the same fourth-order central scheme is used (see chapter 2).

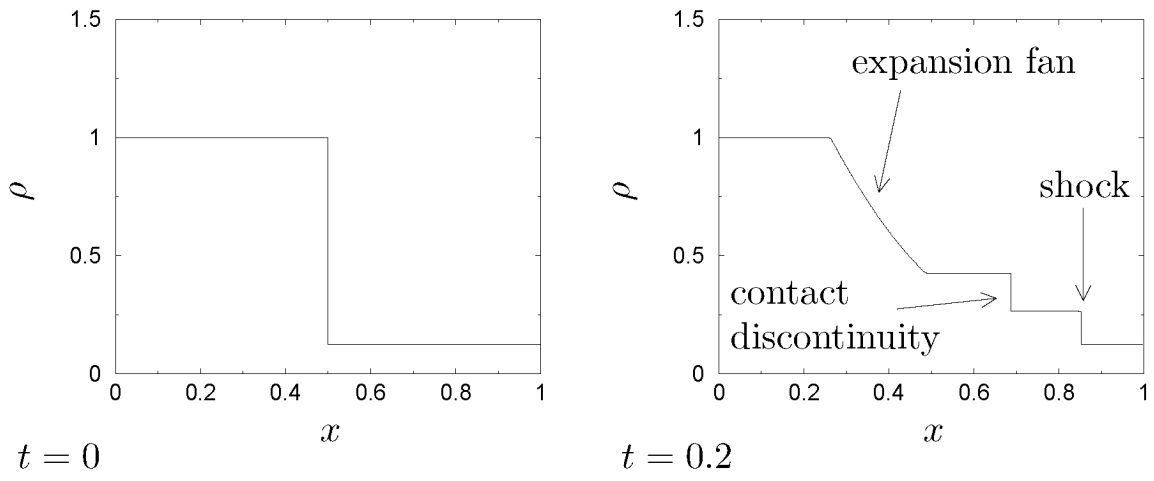

Figure A.1: Exact solution for the shock-tube, ——— density ρ.

It is recalled that the deconvolution order N affects the approximate inverse quantity $\rho^\star = Q_N * \overline{\rho}$ and the relaxation term $-\chi(I - Q_N * G_1) * \overline{\rho}$ (see chapter 3). For further details on the effect of the deconvolution order, we refer to section 5.2.1 and display here only additional results obtained for the nonturbulent shock-tube.

Figures A.2 and A.3 show the temporal evolution of the density for a deconvolution order of N=4 and N=1 respectively. The upper limit for the deconvolution order is dictated by stability reasons since the computation becomes unstable for N=5 and the lower limit corresponds to the lowest deconvolution order used in the compression ramp simulation. The deconvolution order N=4 damps only the high-wavenumber range and large scales oscillations are still present in the flow as can be observed around the contact discontinuity and the shock in figure A.2 (t=0.2). A much smoother solution is obtained when the deconvolution order is reduced to N=1 (figure A.3), indicating that the large scales around the discontinuities have been filtered away. The deconvolution order also affects the relaxation parameter and relaxation term. The average value of the relaxation parameter χ is clearly smaller for the case N=1 than for N=4. This trend finds an explanation with the physical meaning of the relaxation parameter which is the time-scale with which energy is removed from the flow. The smaller energy removal wavenumber range for N=4 is thus compensated by a higher energy removal frequency. An inspection of the values of the relaxation term $-\chi(I - Q_N * G_1) * \overline{\rho}$ confirms this behavior. In average, the values of the relaxation term are lower for N=4 than for N=1 which can be interpreted as a low dissipation for the first case and an increased dissipation for the second case.

Similar investigations on the shock capturing ability of ADM have recently been undertaken by Adams & Stolz (2002). They also varied the deconvolution order of the secondary filter G_2 present in the relaxation term. However, the unfiltered solution $\mathbf{U}^\star$ needed in the nonlinear terms was obtained by singular-value decomposition in their case (direct deconvolution model), and the relaxation parameter χ was kept constant. For test cases such as the "slow-shock problem" (Roberts, 1990) and the Woodward-Colella blast wave (Woodward & Colella, 1984), they came to the same conclusions as found here, i.e. that low-order secondary filters provide a better model of the dissipation mechanism across the shock.

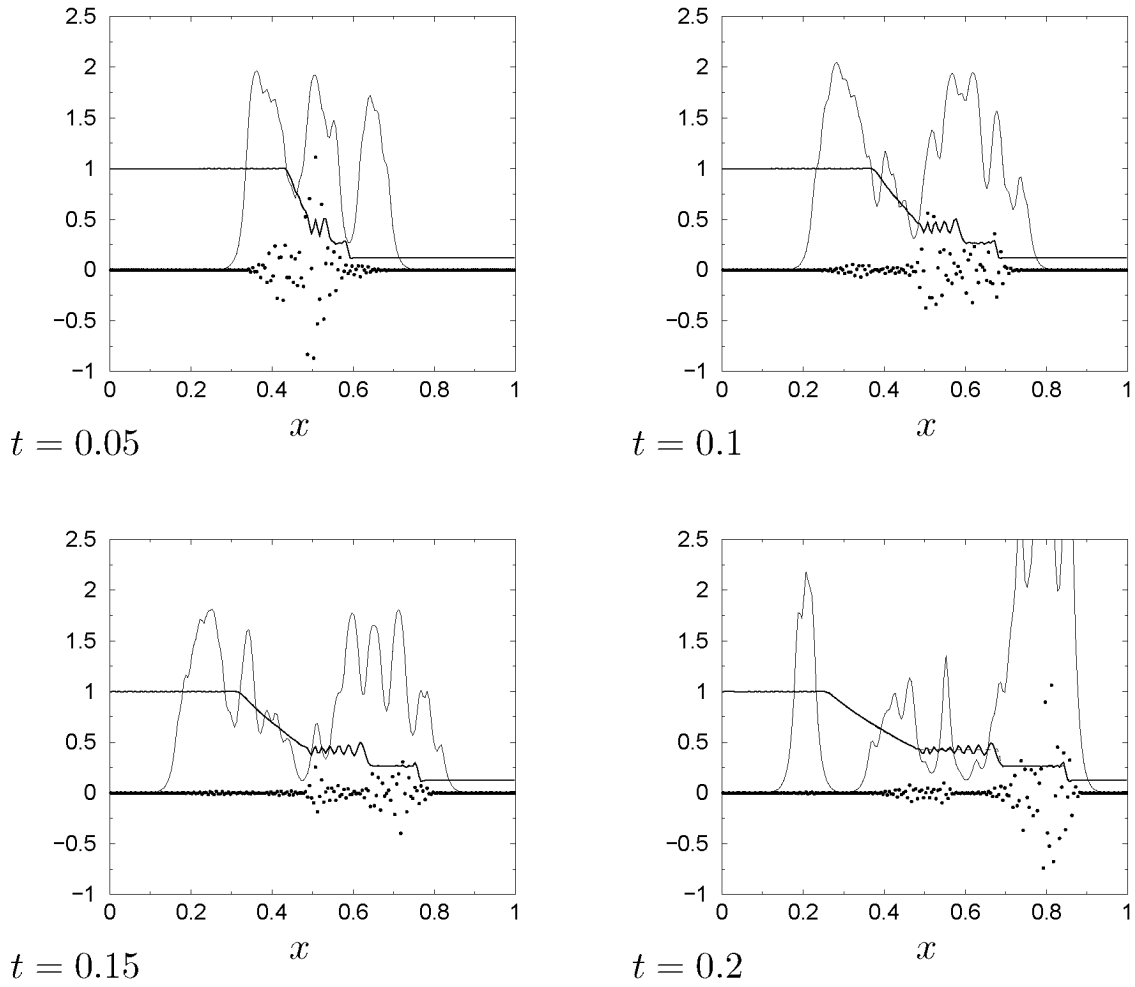

Figure A.2: Deconvolution order N=4. ——— *filtered density* $\overline{\rho}$, ——— *relaxation coefficient* χ *(value is divided by a factor of* 10^2 *for ease of representation on the graph),* • *relaxation term* $\chi(I - Q_4 * G_1) * \overline{\rho}$ *(value is multiplied by a factor* 10^4 *for ease of representation on the graph),* ····· *exact filtered solution* $\overline{\rho}_{exact}$ *(only for t=0.2).*

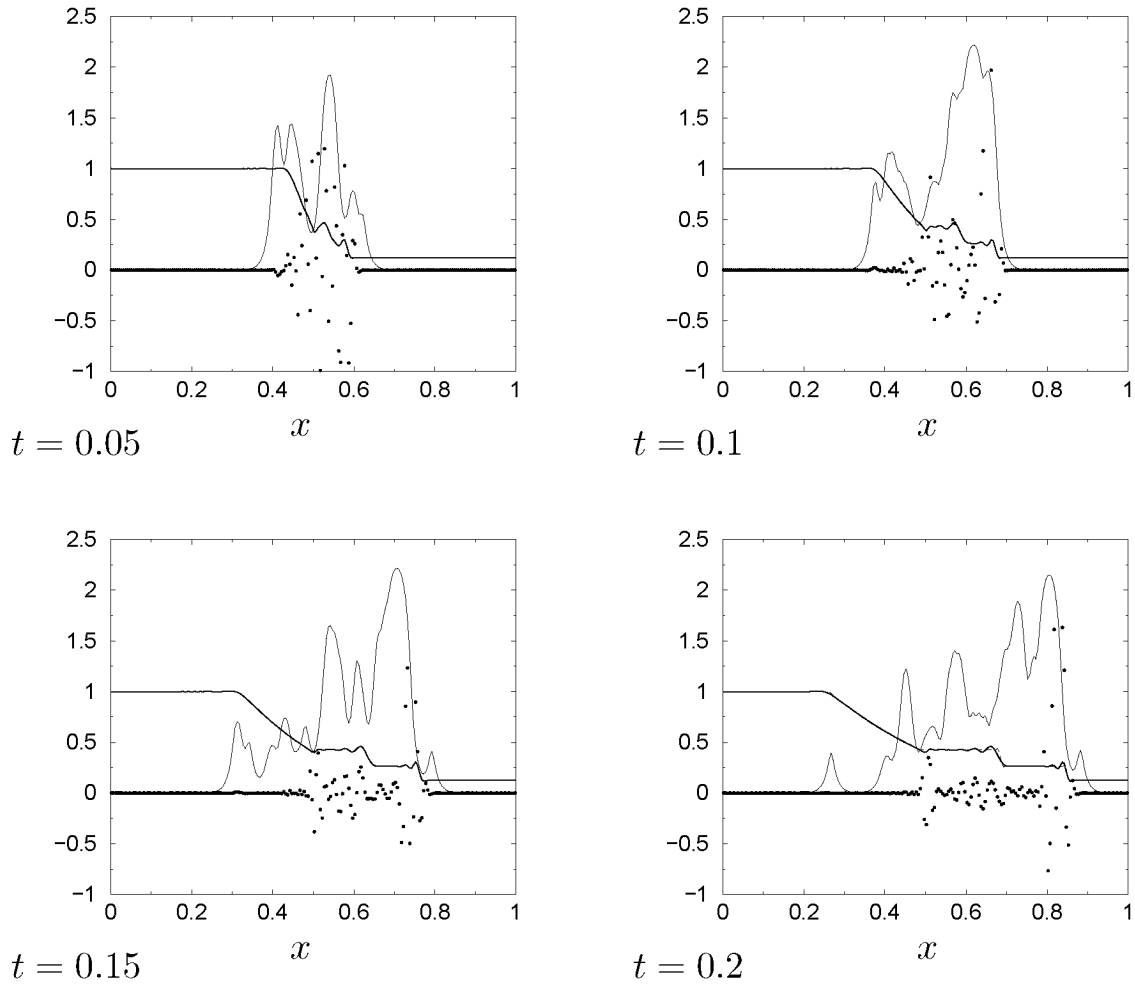

Figure A.3: Deconvolution order N=1. ——— *filtered density* $\overline{\rho}$, ——— *relaxation coefficient* χ *(value is divided by a factor of* 10^2 *for ease of representation on the graph),* • *relaxation term* $\chi(I - Q_1 * G_1) * \overline{\rho}$ *(value is multiplied by a factor* 10^4 *for ease of representation on the graph),* ····· *exact filtered solution* $\overline{\rho}_{exact}$ *(only for t=0.2).*

Bibliography

Ackeret, J., Feldmann, F. & Rott, N. 1946 Untersuchungen an Verdichtungsstößen and Grenzschichten in schnell bewegten Gasen. *Tech. Rep.* Mitt. Inst. Aerodyn. 10. ETH Zürich, Zürich, Switzerland.

Adams, N. A. 2000 Direct simulation of the turbulent boundary layer along a compression ramp at $M = 3$ and $Re_\theta = 1685$. *J. Fluid Mech.* **420**, 47–83.

Adams, N. A. 2001 The role of deconvolution and numerical discretization in subgrid-scale modeling. In *Direct and Large-Eddy Simulation IV* (ed. B. J. Geurts, R. Friedrich & O. Métais).

Adams, N. A. & Stolz, S. 2002 A subgrid-scale deconvolution approach for shock capturing. *J. Comput. Phys.* **178**, 391–426.

Bardina, J., Ferziger, J. H. & Reynolds, W. C. 1980 Improved subgrid-scale models for large-eddy simulation. *AIAA Paper 80-1357* .

Bardina, J., Ferziger, J. H. & Reynolds, W. C. 1983 Improved turbulence models based on large eddy simulation of homogeneous, incompressible, turbulent flows. *Tech. Rep.* TF-19. Dept. of Mechanical Engineering, Stanford University, Stanford, California.

Batchelor, G. K. 1953 *The Theory of Homogenous Turbulence*. Cambridge University Press.

Blaisdell, G. A., Spyropoulos, E. T. & Qin, J. H. 1996 The effect of the formulation of nonlinear terms on aliasing errors in spectral methods. *Applied Numerical Mathematics* **21**, 207–219.

Boris, J. P., Grinstein, F. F., Oran, E. S. & Kolbe, R. L. 1992 New insights into large eddy simulation. In *Fluid Dynamics Research*, , vol. 10, pp. 199–228. North Holland.

Bradshaw, P. 1977 Compressible turbulent shear layers. *Annu. Rev. Fluid Mech.* **9**, 33–54.

Chollet, J. P. 1983 Two-point closure used for sub-grid scale model in large-eddy simulation. In *Turbulent Shear Flows 4* (ed. L. J. S. Bradbury, F. Durst, B. E. Launder, F. W. Schmidt & J. H. Whitelaw), pp. 62–72. Springer–Verlag.

Coleman, G. N., Kim, J. & Moser, R. D. 1995 A numerical study of turbulent supersonic isothermal-wall channel flow. *J. Fluid Mech.* **305**, 159–183.

Constantinescu, G. S., Pacheco, R. & Squires, K. D. 2002 Detached-eddy simulation of flow over a sphere. *AIAA Paper 2002-0425* .

Dahlström, S. & Davidson, L. 2003 LESFOIL: large-eddy simulation of flow around a high lift airfoil. In *Notes on numerical fluid mechanics and multidisciplinary design* (ed. L. Davidson, D. Cokljat, J. Fröhlich, M. A. Leschziner, C. Mellen & W. Rodi), , vol. 83. Springer–Verlag.

Deardorff, J. W. 1970 A numerical study of three-dimensional turbulent channel flow at large Reynolds number. *J. Fluid Mech.* **41**, 453–480.

Deschamps, V. 1988 Simulation numérique de la turbulence inhomogène incompressible dans un écoulement de canal plan. *Tech. Rep.* 5. ONERA, Châtillon, France.

Dolling, D. S. 2001 Fifty years of shock-wave/boundary-layer interaction research: What next? *AIAA J.* **39**, 1517–1531.

Domaradzki, J. A. & Adams, N. A. 2002 Modeling subgrid scales of turbulence in large-eddy simulations. *J. Turb.* **3**.

Domaradzki, J. A. & Radhakrishnan, S. 2002 Subgrid-scale modeling of turbulent convection using truncated navier-stokes dynamics. *Journal of Fluids Engineering* **124**, 823–828.

Ducros, F., Comte, P. & Lesieur, M. 1995 Direct and large–eddy simulations of transition of a supersonic boundary layer. In *Turbulent Shear Flows* (ed. F. Durst, N. Kasagi, B. E. Launder, F. Schmidt, K. Suzuki & J. Whitelaw), pp. 283–300. Springer–Verlag.

Ducros, F., Laporte, F., Soulères, T., Guinot, V., Moinat, P. & Caruelle, B. 2000 High-order fluxes for conservative skew-symmetric-like schemes in structured meshes: application to compressible flows. *J. Comput. Phys.* **161**, 114–139.

Fureby, C. & Grinstein, F. F. 1999 Monotonically integrated large eddy simulation of free shear flows. *AIAA J.* **37**, 544–556.

Fureby, C. & Grinstein, F. F. 2002 Large eddy simulation of high-reynolds-number free and wall-bounded flows. *J. Comput. Phys.* **181**, 68–97.

Gacherieu, C., Collercandy, R., Larrieu, P., Soumillon, P., Tourette, L. & Viala, S. 2000 Navier-Stokes calculations at Aerospatiale Matra Airbus for aircraft design. In *Proc. of ICAS 2000 Congress*.

Garnier, E., Mossi, M., Sagaut, P., Comte, P. & Deville, M. 1999 On the use of shock-capturing schemes for large-eddy simulation. *J. Comput. Phys.* **153**, 273–311.

Garnier, E., Sagaut, P. & Deville, M. 2002 Large-eddy simulation of shock/boundary-layer interaction. *AIAA Journal* **40**, 1935–1944.

Germano, M., Piomelli, U., Moin, P. & Cabot, W. H. 1991 A dynamic subgrid-scale eddy viscosity model. *Phys. Fluids* **A 3**, 1760–1765.

Gilbert, N. & Kleiser, L. 1991 Turbulence model testing with the aid of direct numerical simulation results. In *Eighth Symposium on Turbulent Shear Flows* (ed. R. Friedrich & U. Schumann), pp. 26–1. Munich.

Godunov, S. K. 1959 A difference method for numerical calculation of discontinuous solutions of the equations of hydrodynamics. *Math. Sb.* **47**, 145–156.

Grinstein, F. F. & Fureby, C. 2002 Recent progress on miles for high reynnolds number flows. *J. of Fluids Engineering* **124** (4), 848–861.

Grinstein, F. F. & Fureby, C. 2003 Implicit large eddy simulation of high-Re-flows with flux-limiting schemes. *AIAA Paper 2003-4100* .

Guarini, S. E., Moser, R. D., Shariff, K. & Wray, A. 2000 Direct numerical simulation of a supersonic turbulent boundary layer at Mach 2.5. *J. Fluid Mech.* **414**, 1–33.

Harten, A. 1983 High resolution schemes for hyperbolic conservation laws. *J. Comp. Phys.* **49**, 357–393.

Harten, A. & Chakravarthy, S. R. 1991 Multi-dimensional ENO schemes for general geometries. *Tech. Rep.* 91-76. ICASE, NASA Langley Research Center, Hampton, Virginia, Also CAM report 91-16, UCLA, Los Angeles.

Harten, A., Engquist, B., Osher, S. & Chakravarthy, S. 1987 Uniformly high order essentially non-oscillatory schemes, III. *J. Comp. Phys.* **71**, 231–275.

Harten, A., Lax, P. D. & van Leer, B. 1983 On upstream differencing and Godunov-type schemes for hyperbolic conservation laws. *SIAM Review* **25** (1), 35–61.

Hirsch, C. 1990 *Numerical Computation of Internal and External Flows*. John Wiley & Sons, Chichester.

Jameson, A., Schmidt, W. & Turkel, E. 1981 Numerical solutions of htte Euler equations by finite volume methods using Runge-Kutta time stepping. , vol. 81-1259.

von Kaenel, R., Adams, N. A., Kleiser, L. & Vos, J. B. 2003 The approximate deconvolution method for large-eddy simulation of compressible flows with finite-volume schemes. *J. of Fluids Engineering* **125**, 375–381.

Kato, C., Kaiho, M. & Manabe, A. 2001 Industrial application of les in mechanical engineering. In *Proceedings of the third AFOSR international conference on DNS/LES, DNS/LES-progress and challenges* (ed. C. Liu, L. Sakell & T. Beutner), pp. 47–58. Greyden Press.

Kim, J., Moin, P. & Moser, R. D. 1987 Turbulence statistics in fully developed channel flow at low Reynolds number. *J. Fluid Mech.* **177**, 133–166.

Knight, D. & Degrez, G. 1997 Shock wave boundary layer interactions in high Mach numder flows - a critical survey of current CFD

prediction capabilities. In *AGARD AR-319*, , vol. 2. Neuilly-sur-Seine, France: AGARD.

Krajnović, S. 2002 Development of large-eddy simulation for vehicle aerodynamics. In *Proc. of IMECE 2002*.

Lax, P. D. & Wendroff, B. 1960 Systems of conservation laws. *Comm. Pure Appl. Math.* **13**, 217–237.

Lele, S. K. 1992 Compact finite difference schemes with spectral-like resolution. *J. Comp. Phys.* **103**, 16–42.

Lenormand, E., Sagaut, P., Phuoc, L. T. & Comte, P. 2000 Subgrid-scale models for large-eddy simulations of compressible wall bounded flows. *AIAA Journal* **38**, 1340–1350.

Leschziner, M. A. & Drikakis, D. 2002 Turbulence modelling and turbulent-flow computation in aeronautics. *The Aeronautical Journal* pp. 349–384.

Lesieur, M. & Métais, O. 1996 New trends in large-eddy simulations of turbulence. *Annu. Rev. Fluid. Mech.* **28**, 45–82.

Leveque, R. J. 2002 *Finite Volume Methods for Hyperbolic Problems*. Cambridge, U.K.: Cambridge University Press.

Lilly, D. K. 1967 The representation of small-scale turbulence in numerical simulation experiments. In *Proc. IBM Scientific Computing Symp. on Environmental Sciences* (ed. H. H. Goldstine), pp. 195–210.

Liu, S. W., Meneveau, C. & Katz, J. 1994 On the properties of similarity subgrid-scale models as deduced from measurements in a turbulent jet. *J. Fluid Mech.* **275**, 83–119.

Maeder, T., Adams, N. A. & Kleiser, L. 2001 Direct simulation of turbulent supersonic boundary layers by an extended temporal approach. *J. Fluid Mech.* **429**, 187–216.

Meneveau, C. & Katz, J. 2000 Scale-invariance and turbulence models for large-eddy simulation. *Annu. Rev. Fluid. Mech.* **32**, 1–32.

Métais, O. & Lesieur, M. 1992 Spectral large-eddy simulations of isotropic and stably-stratified turbulence. *J. Fluid Mech.* **239**, 157–194.

Moin, P. & Kim, J. 1982 Numerical investigation of turbulent channel flow. *J. Fluid Mech.* **118**, 341–377.

Morkovin, M. V. 1962 Effects of compressibility on turbulent flows. In *Mécanique de la Turbulence* (ed. A. Favre), pp. 367–380. CNRS, Paris.

Mossi, M. 1999 Simulation of benchmark and industrial unsteady compressible turbulent fluid flows. Thèse epfl no. 1958, Ecole Polytechnique Fédérale de Lausanne, Lausanne, Switzerland.

Müller, B. & Rizzi, A. 1990 Modelling of turbulent transonic flow around aerfoils and wings. *Comm. in Applied Numerical Methods* **6**, 603–616.

Müller, S., Adams, N. A., Stolz, S. & Kleiser, L. 2002 Analysis of LES with the approximate deconvolution model for forced and decaying isotropic turbulence. In *Advances in Turbulence IX* (ed. I. P. Castro, P. E. Hancock & T. G. Thomas), pp. 591–594. CIMNE.

von Neumann, J. & Richtmyer, R. D. 1950 A method for the numerical calculations of hydrodynamics shocks. *J. Appl. Phys.* **21**, 232–237.

Normand, X. & Lesieur, M. 1992 Direct and large-eddy simulations of transition in the compressible boundary layer. *Theor. Comp. Fluid Dyn.* **3**, 231–252.

O'Neil, J. & Meneveau, C. 1997 Subgrid-scale stresses and their modelling in a turbulent plane wake. *J. Fluid Mech.* **349**, 253–293.

Peyret, R. & Taylor, T. D. 1983 *Computational Methods for Fluid Flow*. Springer-Verlag, New York.

Piomelli, U. & Balaras, E. 2002 Wall-layer models for large-eddy-simulations. *Annu. Rev. Fluid Mech.* **34**, 349–374.

Pope, S. B. 2000 *Turbulent Flows*. Cambridge University Press.

Rembold, B., Adams, N. A. & Kleiser, L. 2001 Direct and large-eddy simulation of a transitional rectangular jet. In *Direct and Large-Eddy Simulation IV* (ed. B. J. Geurts, R. Friedrich & O. Métais), pp. 197–204. Kluwer.

Reynolds, O. 1883 An experimental investigation of the circumstances which determine whether the motion of water shall be direct and sinuous, and the law of resistance in parallel channels. *Phil. Trans. Roy.* pp. 51–105.

Rider, W. J. & Margolin, L. 2003 From numerical analysis to implicit subgrid turbulence modeling. *AIAA Paper 2003-4101* .

Rizzetta, D. P. & Visbal, M. R. 2001 Large-eddy simulation of supersonic compression ramp flow. *AIAA Paper 2001-2858* .

Roberts, T. W. 1990 The behavior of flux difference splitting schemes near slowly moving shock waves. *J. Comp. Phys.* **90**, 141–160.

Sagaut, P. 2000 *Large-Eddy Simulation for Incompressible Flows*. Springer.

Sagaut, P. 2001 DNS/LES for complex flows and industrial interest. In *Proceedings of the third AFOSR international conference on DNS/LES, DNS/LES-progress and challenges* (ed. C. Liu, L. Sakell & T. Beutner), pp. 35–46. Greyden Press.

Settles, G. S., Fitzpatrick, T. J. & Bogdonoff, S. M. 1979 Detailed study of attached and separated compression corner flowfields in high Reynolds number supersonic flow. *AIAA J.* **17**, 579–585.

Smagorinsky, J. 1963 General circulation experiments with the primitive equations. *Mon. Weath. Rev.* **93**, 99–164.

Smagorinsky, J. 1993 Some historical remarks on the use of nonlinear viscosities. In *Large eddy simulation of complex engineering and geophysical flows* (ed. B. Galperin & S. A. Orszag), pp. 3–36. Cambridge University Press.

Sod, G. A. 1978 A survey of several finite difference methods for systems of nonlinear hyperbolic conservation laws. *J. Comput. Phys.* **27**, 1–31.

Spalart, P. R., Jou, W.-H., Strelets, M. & Allmaras, S. R. 1997 Comments of the feasibility of les for wings, and on a hybrid rans/les approach. In *Proceedings of the first AFOSR international conference on DNS/LES, Advances in DNS/LES* (ed. C. Liu & Z. Liu). Greyden Press.

Stolz, S. 2000 Large-eddy simulation of complex shear flows using an approximate deconvolution model. Diss. ETH No. 13861, Eidgenössische Technische Hochschule Zürich, Zürich, Switzerland, Published also as Fortschritt-Bericht VDI Reihe 7, Nr. 403, ISBN 3-18-340307-2.

Stolz, S. & Adams, N. A. 1999 An approximate deconvolution procedure for large-eddy simulation. *Phys. Fluids* **11**, 1699–1701.

Stolz, S. & Adams, N. A. 2003 LES of high-Reynolds-number supersonic boundary layers using the approximate deconvolution model. *Phys. Fluids* To appear.

Stolz, S., Adams, N. A. & Kleiser, L. 2000 LES of shock-boundary layer interaction with the approximate deconvolution model. In *Advances in Turbulence IIX* (ed. C. Dopazo), pp. 715–718. CIMNE.

Stolz, S., Adams, N. A. & Kleiser, L. 2001*a* An approximate deconvolution model for large-eddy simulation with application to incompressible wall-bounded flows. *Phys. Fluids* **13**, 997–1015.

Stolz, S., Adams, N. A. & Kleiser, L. 2001*b* The approximate deconvolution model for LES of compressible flows and its application to shock-turbulent-boundary-layer interaction. *Phys. Fluids* **13**, 2985–3001.

Swanson, R. C. & Turkel, E. 1987 Artificial dissipation and central difference schemes for the euler and navier-stokes equations. *AIAA Paper 87-1107* .

Swanson, R. C. & Turkel, E. 1992 On central-difference and upwind schemes. *J. Comput. Phys.* **101**, 292–306.

Sweby, P. K. 1984 High resolution schemes using flux limiters for hyperbolic conservation laws. *SIAM J. Num. Anal.* **21**, 995–1011.

Viala, S., Amant, S. & Tourette, L. 2002 Recent achievements on Navier-Stokes methods for engine integration. In *Proc. of CEAS, Cambridge*.

Visbal, M. R., Morgan, P. E. & Rizzetta, D. P. 2003 An implicit LES approach based on high-order compact differencing and filtering schemes. *AIAA Paper 2003-4098* .

Vos, J. B., Leyland, P., Lindberg, P. A., van Kemenade, V., Gacherieu, C., Duquesne, N., Lotstedt, P., Weber, C., Ytterström, A. & Requier, C. S. 2000 NSMB handbook. *Tech. Rep.*. EPF Lausanne, KTH, CERFACS, Aérospatiale, SAAB.

Vos, J. B., Rizzi, A. W. & Bergman, C. M. 1993 Hypersonic multi block flow simulations around space vehicles including non-equilibrium chemistry. *Tech. Rep.*. AGARD CP-514.

Vreman, B. 1995 Direct and large-eddy simulation of the compressible turbulent mixing layer. PhD thesis, University of Twente.

Wilcox, D. C. 1994 *Turbulence Modeling for CFD*. La Cañada, California: DCW Industries, Inc.

Woodward, P. & Colella, P. 1984 The numerical simulation of two-dimensional flow with strong shocks. *J. Comp. Phys.* **54**, 115–173.

Yoshizawa, A. 1986 Statistical theory for compressible turbulent shear flows, with the application to subgrid modeling. *Phys. Fluids* **29**, 2152–2164.

Zang, Y., Street, R. L. & Koseff, J. H. 1993 A dynamic mixed subgrid-scale model and its application to turbulent recirculating flows. *Phys. Fluids* **A 5**, 3186–3196.

Curriculum vitae

Name	Roland von Kaenel
Date of Birth	October 29, 1976
Place of Birth	Saint-Germain-en-Laye, France
Nationality	Swiss
October 2000 to September 2003	Ph.D. student and research and teaching assistant under the supervision of Prof. L. Kleiser at the Institute of Fluid Dynamics, ETH Zürich, Switzerland
April to September 2000	Research assistant at the Fluid Mechanics Laboratory, EPF Lausanne, Switzerland
April 2000	Diploma (equivalent to Masters degree) in mechanical engineering, EPF Lausanne
October 1999 to February 2000	Visiting graduate student at the Fluid Mechanics Laboratory of the MIT, Cambridge, MA, USA
October 1995 to April 2000	Studies in mechanical engineering, EPF Lausanne; majors: fluid mechanics, thermal sciences and turbomachinery
July 1995	"Federal matura" (high-school graduation), Gymnase de La Tour-de-Peilz, Switzerland